

AN ABSTRACT OF THE THESIS OF

Kent C. Abel for the degree of Master of Science in Nuclear Engineering presented on April 30, 2002.

Title: Axial Development of Two-Phase Flow Parameters in a Vertical Column.

Abstract approved: Redacted for Privacy

The next generation of nuclear safety analysis computer codes will include detailed modeling of the interfacial area concentration. The interfacial area concentration is the essence of the two-fluid model. It is the most accurate of the two-phase models since it considers each phase independently and links the two phases together with six conservation equations. The interfacial area concentration, along with a driving potential, determines the energy, momentum and mass transfer between the two phases.

The importance of this research lies in obtaining a greater understanding of the developing nature of two-phase flows and the application of the two-fluid model. With proper characterization of two-phase flow, the next generation of nuclear safety analysis computer codes will be able to incorporate this information to predict parameters during an accident scenario with greater precision. This research will provide a first order look into the developing nature of two-phase flow.

As part of this research, the development of two-phase flow in a vertical column was analyzed using double sensor impedance probes. The resident vapor and liquid times were recorded along with the velocity of the vapor phase. By creating distributions of the bubble residence times, liquid residence times, velocities, and sizes, one can characterize the developing nature of the two-phase flow. Data was taken at four different axial locations for six different flow rates. The resulting data show clear trends in how the standard deviation and mean values for the measured parameters change as a function of flow rate and axial position. The void fraction contribution from the spherical/distorted bubble group as well as

the cap/slug bubble group was also recorded to determine the net transfer rate of vapor between the two bubble groups. Interfacial area concentration was not included in the measurement since the probes that were used can only determine interfacial area concentration for spherical bubbles. Further research will be conducted with the inclusion of interfacial area concentration at a later time.

©Copyright by Kent C. Abel
April 30, 2002
All Rights Reserved

Axial Development of Two-Phase Flow Parameters in a Vertical Column

By
Kent C. Abel

A THESIS

Submitted to
Oregon State University

in partial fulfillment of
the requirements for the
degree of

Master of Science

Completed April 30, 2002
Commencement June 2002

Master of Science thesis of Kent C. Abel presented on April 30, 2002.

APPROVED:

Redacted for Privacy

Major Professor, representing Nuclear Engineering

Redacted for Privacy

Chair of Department of Nuclear Engineering

Redacted for Privacy

Dean of Graduate School

I understand that my thesis will become part of the permanent collection of Oregon State University libraries. My signature below authorizes release of my thesis to any reader upon request.

Redacted for Privacy

Kent C. Abel, Author

ACKNOWLEDGMENTS

I would like to take this opportunity to thank Dr. José N. Reyes, Jr. for all of his support, ideas, and positive input throughout the research and writing phases of this thesis. He has been instrumental in my education.

I also owe Dr. Qiao Wu a debt of gratitude for all of his help in designing the bubble column as well as for providing theoretical and applied information based upon his vast experience within this field.

I would also like to thank the other members of my committee, Dr. Thomas K. Plant and Dr. William F. Reiter, for their valuable comments and their time. I also thank Stephanie Antoine for her assistance in setting up the probes.

I finally would like to thank my wife for putting up with the late hours of work and providing support throughout this thesis. Lastly, I want to thank my family back home, especially my mother, for their support throughout my college education.

TABLE OF CONTENTS

	<u>Page</u>
1. INTRODUCTION.....	1
2. LITERATURE REVIEW	3
2.1 TYPES OF FLOW REGIMES	3
2.2 TWO-PHASE FLOW MODELS	5
2.2.1 Homogenous model.....	6
2.2.2 Drift-flux model.....	7
2.2.3 Two-fluid model.....	10
2.3 TWO-PHASE FLOW MEASUREMENT TECHNIQUES	13
2.3.1 Non-intrusive techniques.....	14
2.3.1.1 Magnetic resonance imaging (MRI).....	15
2.3.1.2 Gamma densitometer	16
2.3.1.3 Ultrasonic techniques	18
2.3.1.4 Flush mount impedance probe.....	19
2.3.1.5 Photographic method.....	20
2.3.1.6 Light transmission	22
2.3.1.7 Particle image velocimetry (PIV).....	22
2.3.1.8 Laser Doppler velocimetry (LDV)	23
2.3.2 Intrusive techniques.....	24
2.3.2.1 Needle type optical probe.....	25
2.3.2.2 Wire mesh conductivity/impedance probe	27
2.3.2.3 Double or multi-sensor conductivity probe.....	29
2.3.2.4 Acoustic bubble spectrometry	39
2.4 INTERFACIAL AREA TRANSPORT EQUATION	41
2.5 LOCAL INTERFACIAL AREA MEASUREMENT	45
3. EXPERIMENTAL SETUP	48
3.1 EXPERIMENTAL APPARATUS	48
3.2 INSTRUMENTATION.....	53

TABLE OF CONTENTS (Continued)

	<u>Page</u>
3.2.1 Impedance probe principles of measurement	54
3.2.2 Impedance probe design	57
3.2.3 Signal processing	59
3.2.4 Data acquisition	61
3.2.5 Post processing	62
4. DATA AND RESULTS	63
4.1 RESIDENT VAPOR TIME	67
4.2 RESIDENT LIQUID TIME	82
4.3 VAPOR VELOCITY MEASUREMENT	96
4.4 TWO-GROUP VOID FRACTION	102
5. CONCLUSIONS AND PLANS FOR FUTURE WORK	108
BIBLIOGRAPHY	110
APPENDIX	114
C++ DATA PROCESSING PROGRAM.....	115

LIST OF FIGURES

<u>Figure</u>	<u>Page</u>
2.1 Flow patterns in vertical flow.....	4
2.2 Flow patterns in horizontal flow.....	5
2.3 Gamma densitometer measurement	17
2.4 Flush mount conductivity probe.....	20
2.5 Optical needle probe operation.....	26
2.6 Needle type optical probe diagram.....	27
2.7 Wire mesh sensor diagram	29
2.8 The jth interface of a bubble.....	32
2.9 General double sensor conductivity probe design.....	38
3.1 Schematic of the test facility	48
3.2 Air-water injector top view	50
3.3 Air-water injector side view	51
3.4 Air-water separator baffle plate.....	52
3.5 Instrumentation mount design.....	53
3.6 Some of the possible double-sensor probes signals	56
3.7 Needle probe design	58
3.8 Impedance probe signal processing circuit for one probe tip.....	59
3.9 Impedance probe timing diagram.....	60
4.1 Resident vapor time distribution, L/D=90, 20 gpm, 40 scfh.....	70

LIST OF FIGURES (Continued)

<u>Figure</u>	<u>Page</u>
4.2 Resident vapor time distribution, L/D=60, 20 gpm, 40 scfh	70
4.3 Resident vapor time distribution, L/D=30, 20 gpm, 40 scfh	71
4.4 Resident vapor time distribution, L/D=6, 20 gpm, 40 scfh	71
4.5 Resident vapor time distribution, L/D=90, 20 gpm, 60 scfh	72
4.6 Resident vapor time distribution, L/D=60, 20 gpm, 60 scfh	72
4.7 Resident vapor time distribution, L/D=30, 20 gpm, 60 scfh	73
4.8 Resident vapor time distribution, L/D=6, 20 gpm, 60 scfh	73
4.9 Resident vapor time distribution, L/D=90, 20 gpm, 80 scfh	74
4.10 Resident vapor time distribution, L/D=60, 20 gpm, 80 scfh	74
4.11 Resident vapor time distribution, L/D=30, 20 gpm, 80 scfh	75
4.12 Resident vapor time distribution, L/D=6, 20 gpm, 80 scfh	75
4.13 Resident vapor time distribution, L/D=90, 30 gpm, 40 scfh	76
4.14 Resident vapor time distribution, L/D=60, 30 gpm, 40 scfh	76
4.15 Resident vapor time distribution, L/D=30, 30 gpm, 40 scfh	77
4.16 Resident vapor time distribution, L/D=6, 30 gpm, 40 scfh	77
4.17 Resident vapor time distribution, L/D=90, 30 gpm, 60 scfh	78
4.18 Resident vapor time distribution, L/D=60, 30 gpm, 60 scfh	78
4.19 Resident vapor time distribution, L/D=30, 30 gpm, 60 scfh	79
4.20 Resident vapor time distribution, L/D=6, 30 gpm, 60 scfh	79

LIST OF FIGURES (Continued)

<u>Figure</u>		<u>Page</u>
4.21	Resident vapor time distribution, L/D=90, 30 gpm, 80 scfh	80
4.22	Resident vapor time distribution, L/D=60, 30 gpm, 80 scfh	80
4.23	Resident vapor time distribution, L/D=30, 30 gpm, 80 scfh	81
4.24	Resident vapor time distribution, L/D=6, 30 gpm, 80 scfh	81
4.25	Resident liquid time distribution, L/D=90, 20 gpm, 40 scfh	84
4.26	Resident liquid time distribution, L/D=60, 20 gpm, 40 scfh	84
4.27	Resident liquid time distribution, L/D=30, 20 gpm, 40 scfh	85
4.28	Resident liquid time distribution, L/D=6, 20 gpm, 40 scfh	85
4.29	Resident liquid time distribution, L/D=90, 20 gpm, 60 scfh	86
4.30	Resident liquid time distribution, L/D=60, 20 gpm, 60 scfh	86
4.31	Resident liquid time distribution, L/D=30, 20 gpm, 60 scfh	87
4.32	Resident liquid time distribution, L/D=6, 20 gpm, 60 scfh	87
4.33	Resident liquid time distribution, L/D=90, 20 gpm, 80 scfh	88
4.34	Resident liquid time distribution, L/D=60, 20 gpm, 80 scfh	88
4.35	Resident liquid time distribution, L/D=30, 20 gpm, 80 scfh	89
4.36	Resident liquid time distribution, L/D=6, 20 gpm, 80 scfh	89
4.37	Resident liquid time distribution, L/D=90, 30 gpm, 40 scfh	90
4.38	Resident liquid time distribution, L/D=60, 30 gpm, 40 scfh	90
4.39	Resident liquid time distribution, L/D=30, 30 gpm, 40 scfh	91

LIST OF FIGURES (Continued)

<u>Figure</u>	<u>Page</u>
4.40 Resident liquid time distribution, $L/D=6$, 30 gpm, 40 scfh.....	91
4.41 Resident liquid time distribution, $L/D=90$, 30 gpm, 60 scfh.....	92
4.42 Resident liquid time distribution, $L/D=60$, 30 gpm, 60 scfh.....	92
4.43 Resident liquid time distribution, $L/D=30$, 30 gpm, 60 scfh.....	93
4.44 Resident liquid time distribution, $L/D=6$, 30 gpm, 60 scfh.....	93
4.45 Resident liquid time distribution, $L/D=90$, 30 gpm, 80 scfh.....	94
4.46 Resident liquid time distribution, $L/D=60$, 30 gpm, 80 scfh.....	94
4.47 Resident liquid time distribution, $L/D=30$, 30 gpm, 80 scfh.....	95
4.48 Resident liquid time distribution, $L/D=6$, 30 gpm, 80 scfh.....	95
4.49 Velocity distribution, $L/D=60$, 20 gpm, 40 scfh	97
4.50 Velocity distribution, $L/D=60$, 20 gpm, 60 scfh	97
4.51 Velocity distribution, $L/D=60$, 20 gpm, 80 scfh	98
4.52 Velocity distribution, $L/D=60$, 30 gpm, 40 scfh	98
4.53 Velocity distribution, $L/D=60$, 30 gpm, 60 scfh	99
4.54 Velocity distribution, $L/D=60$, 30 gpm, 80 scfh	99
4.55 Improper velocity measurement at $L/D=6$	102
4.56 Two-group vapor time distribution for $L/D=90$, 20gpm, 80scfh	103
4.57 Two-group void fraction, $L/D=90$	106
4.58 Two-group void fraction, $L/D=60$	106

LIST OF FIGURES (Continued)

<u>Figure</u>		<u>Page</u>
4.59	Two-group void fraction, $L/D=30$	107
4.60	Two-group void fraction, $L/D=6$	107

LIST OF TABLES

<u>Table</u>		<u>Page</u>
2.1	Typical non-intrusive bubbly/slug flow measurement techniques	15
2.2	Typical intrusive bubbly/slug flow measurement techniques	25
4.1	Test matrix	63
4.2	Void fraction data	64
4.3	Mean resident vapor time (ms)	68
4.4	Resident vapor time standard deviation (ms)	68
4.5	Mean resident liquid time (ms)	82
4.6	Resident liquid time standard deviation (ms)	83
4.7	Velocity Results for L/D=60 Location	101
4.8	Two group void fraction table L/D=90	104
4.9	Two group void fraction table L/D=60	104
4.10	Two group void fraction table L/D=30	105
4.11	Two group void fraction table L/D=6	105

NOMENCLATURE

a_i	interfacial area concentration
C_o	distribution parameter
D_{Sm}	Sauter mean diameter
f	calibration factor
$g(\omega_0)$	probability density function of angle ω
$I(\omega_0)$	correction factor
j_l, j_g	superficial velocity of liquid and gas
ℓ_{bubble}	bubble chord length
L_s	length scale at interface
n	surface normal vector
N	total number
t	time
T	total sampling time
V_{gj}	drift velocity of the j th interface
v	velocity
x	vapor quality
z	axial position

Greek Symbols

α	void fraction of gas phase
Δs	spacing between front and rear sensor of double probe
Δt_{kj}	transit time for j^{th} interface to pass between front and rear sensor k
ρ	density
σ	surface tension
τ	resident time for a single bubble

ω	angle between the velocity vector of the j^{th} interface and the velocity vector of the mean flow direction
ω_0	the maximum angle of ω
φ_j	angle between n and v_{ij}
$\dot{\varphi}$	rates of change of the bubble number density
$\dot{\Phi}$	rates of change of the interfacial area concentration
ψ	bubble shape factor

Subscripts

B, C	bubble breakup, bubble coalescence
P, V	phase change, void transport
b, miss	bubble, missing
f, g, i	liquid phase, gas phase, value at interface
j	interface number
k	rear sensor number ($k=1, 2, 3$)
t	per unit time
z	z component
0	reference
∞	terminal

Mathematical operators

$\langle \rangle$	area averaged quantity
$\langle\langle \rangle\rangle$	void fraction weighted area averaged quantity
$^{-t}$	time averaged quantity
$^{-l}$	line averaged quantity

Axial Development of Two-Phase Flow Parameters in a Vertical Column

1. INTRODUCTION

Within the area of two-phase fluid flow, there is still little understanding of the complex nature in which bubbles interact in the evolution of their size and shape. The knowledge of the behavior of bubbles in two-phase flow is important in many research and industrial applications such as chemical reactors and nuclear power plants. The main two-phase flow parameter of interest is the interfacial area concentration. The interfacial area concentration is defined as the total surface area between the two phases of interest per volume of mixture. The interfacial area concentration is of great importance because the surface area between the two phases governs the transfer rate of energy, mass, and momentum between the two phases.

Since the interfacial area concentration is a difficult quantity to measure, especially on a local basis, one must instead measure the diameters of the bubbles and then either use a photographic method to determine the shape of the bubble or assume a bubble shape to relate a one-dimensional length quantity to a surface area. Hence the importance of measuring bubble sizes and how the distribution of bubble sizes change along the length of a pipe. With adequate information of how the distribution of bubble sizes changes as flow develops, one may be able to achieve a greater understanding on how two-phase flow develops. This could then lead to better predictions of how the interfacial area concentration develops along the axial direction.

Unfortunately, the distribution data is not presented by most researchers and is instead replaced with time averaged local values for interfacial area concentration, void fraction, and Sauter mean diameter. The Sauter mean diameter is a mean effective bubble diameter that provides a relationship between interfacial area concentration and void fraction. By just looking at averaged quantities, much

information is lost on the size of individual bubbles. In the few cases where researchers do display bubble size distributions, the histograms typically have very few bins, the distributions are typically not fitted with a distribution function, and the distributions are typically only given at one axial position for a few different flow conditions.

With this research, however, the intent is to sample a large number of bubbles at several axial locations for a given flow rate at the pipe centerline location. This will then lead to distributions of bubble sizes, resident times, and velocities with a large number of bins which then will later have distributions fitted to them by a commercial computer program. With this information, one can observe how parameters such as mean bubble size and standard deviation change. In addition, one can then examine how the distributions change along the length of the pipe as well as for different flow rates. The other important information that will be gathered is to see how the bubble size distribution changes from a single distribution into two distinct distributions as in the case of developing slug flow. This is important in relation to the interfacial area transport equation which separates bubbles into two groups: the spherical/distorted bubble group, otherwise known as group one, and the cap/slug bubble group, otherwise known as group two. By analyzing this change from a single distribution to two distinct distributions, one can determine the net transfer rate between group one bubbles and group two bubbles.

By achieving a greater understanding of two-phase flows, it is hoped that the subjectively based flow regime maps used in today's multiphase computer codes may be eliminated and replaced with a more precise method.

2. LITERATURE REVIEW

2.1 TYPES OF FLOW REGIMES

The use of flow regimes is a way to visually categorize the void distribution patterns of gas-liquid flows. These patterns depend upon gas and liquid flow rates, channel geometry, pressure and orientation to gravity. In the nuclear engineering industry, the two most important flow orientations are vertical and horizontal. In other fields such as petroleum engineering, inclined flows are also important. In the nuclear engineering field, upward, vertical, co-current flow is important in simulating a Boiling Water Reactor (BWR) fuel assembly. The horizontal co-current flow is important for simulation of a Light Water Reactor (LWR) piping during transients.

The distinct flow regimes in the vertical flow orientation are bubbly, slug, churn, and annular. A representation of these flows is given in Figure 2.1. The bubbly flow regime is characterized by the existence of dispersed bubbles in a continuous liquid phase. Smaller bubbles are typically spherical, but larger bubbles tend to be between spherical and ellipsoid in shape. Slug flow is constructed of large gas bubbles separated by liquid slugs. Within the liquid slug, small bubbles like those in bubbly flow exist. In addition, in the case of slug flow, a thin liquid film surrounding the slug bubble falls downward as the slug rises. Churn flow is similar to slug flow but is more chaotic. The annular flow regime exists at high gas flow rates and is characterized by a gas core surrounded by a liquid film. The annular flow regime may also contain liquid droplets within the gas core depending on the flow rates used.

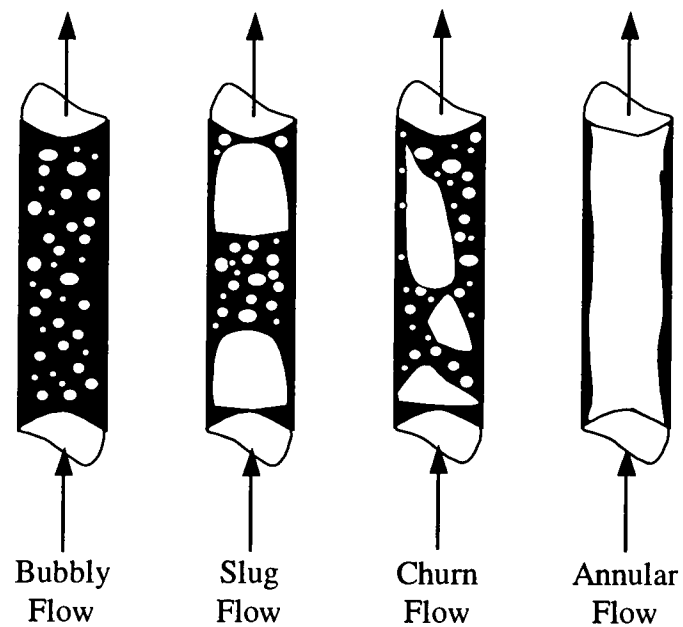


Figure 2.1: Flow patterns in vertical flow

Flow in a horizontal section has the ability to become stratified and thus contains more flow regimes than in the vertical case. Another difference between the vertical and horizontal flow case is the radial location of the maximum void fraction. The void fraction distribution is normally peaked in the center of the pipe for the vertical case, but due to the bubble buoyancy, the void fraction distribution peak in the horizontal case is near the top wall. The flow regimes for the horizontal case are given in Figure 2.2.

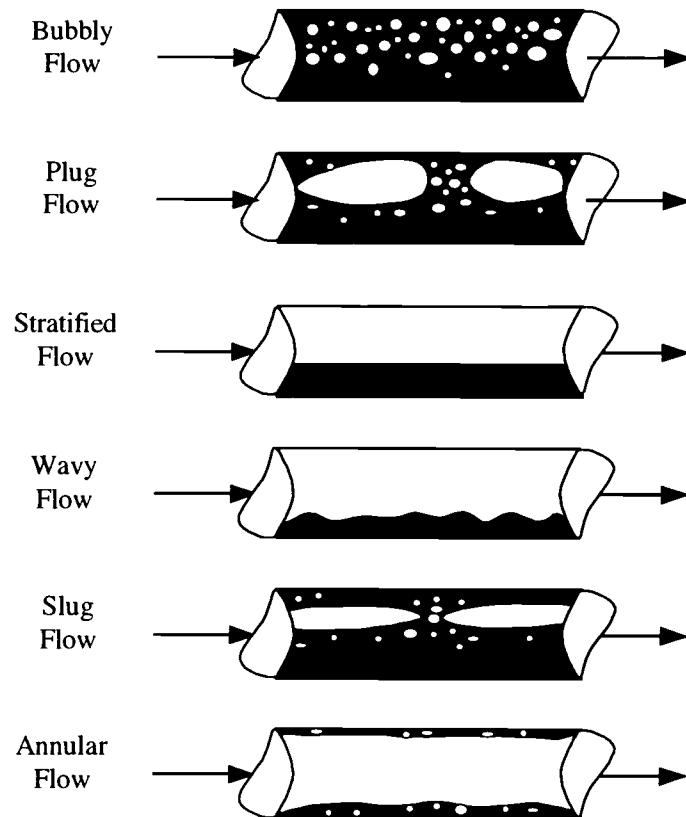


Figure 2.2: Flow patterns in horizontal flow

2.2 TWO-PHASE FLOW MODELS

In the field of two-phase flow, three important models have been proposed. These models include the homogeneous flow model, the drift flux model and the two-fluid model. A description of each of these models is given:

1. **Homogeneous model** – In this model, the two phases are assumed to move with the same velocity and have the same temperature. This allows the two-phase mixture to be treated as a single fluid. This model is useful at high

pressure and high flow rate conditions. The temperature is the saturation temperature for that pressure. Since at high flow rates, the gas and liquid move with the approximately same velocity, the equal velocity of the two phases is a good assumption.

2. **Drift flux model** – This model is similar to the homogeneous model except it allows the two phases to move with different velocities or a slip ratio. This model requires that the relative velocity between the two phases be given by a predetermined relationship. This model is useful for low pressure or low flow rate flows in which the system is at steady-state condition.

3. **Two-fluid model** – This is the most advanced of these three models. The two-fluid model allows the two phases to have unequal temperatures as well as unequal velocities. The model uses conservation of mass, momentum, and energy transfer equations. This model is most useful where transient and non-equilibrium conditions exist. However, since this is the most descriptive of the three models, the two-fluid model may also be applied to the simpler flow conditions.

2.2.1 Homogenous model

The homogeneous model is the most simplistic of these three models since it assumes that both phases are at the same temperature and move with the same velocity. Although simple, the homogenous model does have applications for which it is applicable. These include applications in which everything is at saturation temperature, moving at high flow rates, and at steady state condition. An example in which the homogenous model may work well is in modeling a BWR fuel channel

during normal steady state operation. The area averaged void fraction given by the homogenous model is given in equation (2.1).

$$\langle \alpha \rangle = \frac{1}{1 + \frac{1-x}{x} \frac{\rho_g}{\rho_f}} \quad (2.1)$$

Where x is the vapor quality, ρ_g is the density of the gas and ρ_f is the liquid density. The vapor quality, x , is defined as the mass flow rate of the vapor divided by the mass flow rate of the two-phase mixture.

2.2.2 Drift-flux model

The drift flux model is currently the most widely used model in two-phase flow. This is because the drift flux model offers more flexibility than the homogeneous model but is much less complex than the two-fluid model. The drift flux model is most commonly used for co-current upward, vertical flows. However, Franca and Lahey (Franca and Lahey, 1992) successfully applied the drift flux model to horizontal flows. The drift flux model stems from a paper that Zuber and Findley (Zuber and Findley, 1965) published. This basic drift flux model has been revised by other researchers over the years. The one dimensional drift flux model for a relative velocity v_r is given by:

$$(1-\alpha)v_r = (C_o - 1)j + \langle \langle V_{gj} \rangle \rangle \quad (2.2)$$

where C_o , j , and $\langle \langle V_{gj} \rangle \rangle$ are the distribution parameter, total volumetric flux, and the void fraction weighted area average of the local drift velocity respectively. The total volumetric flux is defined as:

$$j = j_g + j_f \quad (2.3)$$

where j_g and j_f are the superficial gas and liquid velocities respectively. The relative velocities between the phases is given by:

$$v_r = u_g - u_f \quad (2.4)$$

where $u_g = j_g/\alpha$ and $u_f = j_f/(1-\alpha)$. By combining these relations, one can find the void fraction as follows:

$$\alpha = \frac{j_g}{C_o j + \langle\langle V_{gj} \rangle\rangle} \quad (2.5)$$

The distribution parameter, C_o , is defined by equation (2.6). Often the distribution parameter is found by using one of the many correlations that exist. For bubbly and slug flows, the value of C_o is approximately 1.2. Kataoka and Ishii (Kataoka and Ishii, 1987) used the drift flux model to apply towards a large diameter pipe to develop a correlation for pool void fraction. Kataoka and Ishii found that the drift velocity of a pool system depends upon vessel diameter, pressure, gas flux, and the physical properties of the fluid being studied. They found that the drift velocity and the void fraction measured experimentally could be quite different from those predicted by the conventional correlations at the time. The correlation that Kataoka and Ishii developed based on the drift flux model fit the existing experimental data much better than the conventional correlations.

$$C_o = \frac{\langle\alpha j\rangle}{\langle\alpha\rangle\langle j\rangle} \quad (2.6)$$

Kataoka et al. (Kataoka et al., 1987) applied the drift flux model to a vertical column in which the liquid phase was stagnant. They found that the distribution parameters, C_o , for the stagnant flow case were higher than those found at higher liquid flow rates. Kataoka et al. found that the drift velocity however was nearly the same for the different liquid flow rates. Kaminaga (Kaminaga, 1992) compared experiments that were in vertical columns with small diameters and having a low

liquid velocity to three different correlations. The correlations that are compared include Ishii's correlation, Kataoka's (Kataoka and Ishii, 1987) correlation based on stagnant liquid, and a correlation for stagnant or low liquid velocities in an air-water system determined by Ellis. Kaminaga determined that the void fraction correlations of Ishii and Ellis were valid with experimental data within a 30% error for gas velocities over 0.2 m/s in a round tube with a diameter less than 50 mm. However, if the gas velocity is less than 0.2 m/s, Kaminaga found that none of the correlations selected for this study could be applied and suggested that a correlation that is applicable in this velocity range for small diameter tubes needed to be determined. In 1989, Chen and Fan (Chen and Fan, 1989) applied the drift flux model to a vertical column consisting of air, water, and 3.04 mm diameter glass beads. It was found that the drift flux model can be applied to a three phase system such as this one and return a value for the bubble velocity with an error of less than 10% and 2% error in liquid holdup for the liquid-solid sedimentation region. This paper demonstrates that the drift flux model can be applied to more than a gas-liquid system.

Franca and Lahey (Franca and Lahey, 1992) applied the drift flux model to the horizontal flow orientation. They found that horizontal two-phase flows could be well correlated using the drift flux model. They also discovered that the standard variables $\langle j_g \rangle / \langle \alpha \rangle$ and $\langle j \rangle$ work well for plug and slug flows while $\langle \alpha \rangle / (1 - \langle \alpha \rangle)$ and $\langle j_g \rangle / \langle j \rangle$ are more appropriate for stratified and annular flows. For plug, wavy-stratified, and annular flow, the distribution parameter, C_o , is equal to about 1.0 while for plug flow the distribution parameter is equal to 1.2. The drift velocity, V_{gj} , found in horizontal flow ranged from -0.20 m/s, for slug flow, up to 0.27 m/s for annular flow. A negative value for the drift velocity indicates that the liquid phase is moving faster than the vapor phase.

2.2.3 Two-fluid model

The two-fluid model is considered the most accurate of these models because this model considers each phase separately in terms of two sets of conservation equations (Hibiki et al., 1998; Hibiki and Ishii, 1999; Revankar and Ishii, 1992; Rinne and Loth, 1996; Wu et al., 1998). These conservation equations include a balance of mass, energy and momentum of each phase. Since mass, energy, and momentum can transfer between the two phases; one needs to accurately predict these transfer terms. The weakest link of this model is the difficulty in accurately predicting or measuring the interfacial transfer terms. Since the interfacial transfer terms are related to the area between the two phases, one needs to be able to find the interfacial area or interfacial area concentration. Thus, interfacial area and interfacial area concentration are two important parameters in the field of two-phase flow. The interfacial area concentration has units of area per volume and is defined as:

$$\frac{1}{L_s} = a_i = \frac{\text{Interfacial area}}{\text{Mixture volume}} \quad (2.7)$$

where L_s is the length scale at the interface and a_i is the interfacial area concentration. The three conservation equations are given as follows (Revankar and Ishii, 1992):

continuity equation:

$$\frac{\partial \alpha_k \rho_k}{\partial t} + \nabla \cdot (\alpha_k \rho_k \mathbf{v}_k) = \Gamma_k; \quad (2.8)$$

momentum equation:

$$\frac{\partial \alpha_k \mathbf{v}_k}{\partial t} + \nabla \cdot (\alpha_k \rho_k \mathbf{v}_k \mathbf{v}_k) = -\alpha_k \nabla p_k + \nabla \cdot \alpha_k (\bar{\tau}_k + \tau_k^t) + \alpha_k \rho_k \mathbf{g} + \mathbf{v}_{ki} \Gamma_k + \mathbf{M}_{ik} - \nabla \alpha_k \cdot \boldsymbol{\tau}_i ; \quad (2.9)$$

enthalpy energy equation:

$$\frac{\partial \alpha_k \rho_k H_k}{\partial t} + \nabla \cdot (\alpha_k \rho_k H_k \mathbf{v}_k) = \nabla \cdot \alpha_k (\bar{q}_k + q_k^t) + \alpha_k \frac{D_k}{D_t} p_k + H_{ki} \Gamma_k + \frac{q_{ki}''}{L_s} + \Phi_k \quad (2.10)$$

The symbols Γ_k , \mathbf{M}_{ik} , $\boldsymbol{\tau}_i$, and Φ_k are the mass generation per unit volume, interfacial drag, the interfacial shear stress, the interfacial heat flux and the dissipation respectively. The subscripts k and i indicate the value of the term for phase k at the interface i. The terms α_k , ρ_k , \mathbf{v}_k , p_k , q_{ki}'' , and H_k represent the void fraction, density, velocity, pressure, interfacial heat flux and enthalpy of phase k respectively. The terms $\bar{\tau}_k$, τ_k^t , \bar{q}_k , q_k^t , and \mathbf{g} are the average viscous stress, turbulent stress, mean conduction heat flux, the turbulent heat flux, and the acceleration due to gravity respectively. H_{ki} symbolizes the enthalpy of phase k at the interface. The right hand sides of equations (2.7) - (2.9) are the interfacial transfer terms and are related to each other by using averaged local jump conditions. If one rewrites equations (2.7) - (2.9) in terms of the average mass transfer per unit area, m_k , which is defined as $\Gamma_k = m_k/L_s$, one can write the right hand side of these equations as an interfacial area multiplied by a driving force. The results are as follows:

continuity equation:

$$\frac{\partial \alpha_k \rho_k}{\partial t} + \nabla \cdot (\alpha_k \rho_k \mathbf{v}_k) = \frac{m_k}{L_s}; \quad (2.11)$$

momentum equation:

$$\begin{aligned} \frac{\partial \alpha_k \mathbf{v}_k}{\partial t} + \nabla \cdot (\alpha_k \rho_k \mathbf{v}_k \mathbf{v}_k) = & -\alpha_k \nabla p_k + \nabla \\ & \cdot \alpha_k (\overline{\boldsymbol{\tau}}_k + \boldsymbol{\tau}_k^t) + \alpha_k \rho_k \mathbf{g} + \frac{1}{L_s} (\mathbf{v}_{ki} m_k + \zeta_{ik}) - \nabla \alpha_k \cdot \boldsymbol{\tau}_i; \end{aligned} \quad (2.12)$$

enthalpy energy equation:

$$\begin{aligned} \frac{\partial \alpha_k \rho_k H_k}{\partial t} + \nabla \cdot (\alpha_k \rho_k H_k \mathbf{v}_k) = & \nabla \cdot \alpha_k (\overline{q}_k + q_k^t) \\ & + \alpha_k \frac{D_k}{D_t} p_k + \frac{1}{L_s} (m_k H_{ki} + q_{ki}^r) + \Phi_k \end{aligned} \quad (2.13)$$

With ζ_{ik} in equation (2.12) being the interfacial drag force per cross-sectional bubble area. Equations (2.11) – (2.13) shows that the interfacial transfer terms are proportional to the interfacial area concentration multiplied by a driving force. The importance of interfacial area concentration is shown by the appearance of interfacial area concentration in each one of the conservation equations. Although, the interfacial area concentration is an important value, measurement of interfacial area concentration in the real world is very difficult and so there is very few data sets with good local interfacial area concentration data. Most of the interfacial area data sets are limited to averaged values over a section of pipe due to many of the interfacial area concentration data sets being determined by a first order chemical reaction. The driving force for the energy equation is the heat flux between the two phases based on:

$$q_{ki}'' = h_{ki}(T_i - T_k) \quad (2.14)$$

where T_i and T_k are the interfacial and bulk temperatures based on the mean enthalpy and h_{ki} is the interfacial heat transfer coefficient. The driving force for the continuity equation is the mass generation per volume and for the momentum equation; the driving force is based on the interfacial drag and velocity. By separating out the length scale, L_s , from each of the conservation equations, one is able to determine each of the driving forces independently of the interfacial area concentration. This allows one to perform separate experiments for interfacial area concentration and the driving forces independently and then recombining the information to construct the set of conservation equations.

2.3 TWO-PHASE FLOW MEASUREMENT TECHNIQUES

As part of this literature review, a survey of two-phase flow measurement techniques was conducted to determine the most applicable measurement techniques for this research. This survey will point out some of the major two-phase flow measurement techniques with their advantages, limitations, what two-phase parameters the technique can measure as well as how each technique works. This will allow one to quickly discern the types of technology that is available in two-phase flow and where each technique may be applicable.

Two-phase flow measurement techniques can be broken up into two broad categories. These categories include intrusive techniques and non-intrusive techniques. Non-intrusive techniques are generally preferable to intrusive techniques since the measurement device does not disturb the flow. However, only a few non-intrusive techniques are available and many only work for certain types of flow, not all give parameters of interest or may have other restrictions. Because of these limitations, researchers many times have to resort to intrusive techniques. A description of popular two-phase flow measurement techniques with their advantages and limitations are listed in the following sections.

2.3.1 Non-intrusive techniques

Non-intrusive techniques are theoretically ideal for measurement of two-phase flow parameters since there is no contact with the flow and thus no flow disturbance. However, in practice the non-intrusive techniques tend to be expensive and have quite a few limitations. Some of these limitations include the use of transparent piping and/or fluid, non-magnetic piping for MRI and low void fraction limitation for the optical and ultrasonic techniques. The most widely used non-intrusive two-phase flow measurement techniques are listed in Table 2.1.

Table 2.1: Typical non-intrusive bubbly/slug flow measurement techniques

Measurement Technique	Measurement	Types of Measurement	Advantages	Limitations
MRI	All points within the measurement volume	Void fraction, interfacial area, velocity	Full 3-D view of flow within the MRI	Needs non-magnetic piping, non-conductive fluid, cost, typically only horizontal flow, limited speed
Gamma Densitometer	Line averaged	Void fraction	Does not need clear pipes or fluid. Works full range of void fractions.	Need radioactive source and shielding
Ultrasonic Techniques	Local	Void fraction, interfacial area, velocity	Fairly inexpensive, does not need clear pipe or fluid	Low void fraction, limited imaging depth
Flush mount impedance probe	Area averaged	Void fraction	Inexpensive, simple	Needs conductive liquid. Probe mount must be an insulator
Photographic Method	Local and average	Void fraction, interfacial area	Inexpensive, simple	Transparent fluid and walls. Low void fraction.
Light Transmission	Local and average	Interfacial area, void fraction	Fairly inexpensive	Low void fraction, Transparent system
PIV	Local and average	Velocity, vorticity	Allows 2-D and 3-D measurement of velocity and vorticity fields	Low void fraction, need to add tracer, clear fluid and pipe
LDV	Local, line or area with traversing	Velocity, vorticity	Measures up to 3 components of velocity, accurate, wide range of velocities	Low void fraction, clear fluid and pipe

2.3.1.1 Magnetic resonance imaging (MRI)

According to Reyes (Reyes et al. 1998), two MRI imaging methods are available for the study of two-phase flow. These methods include the phase shift methodology and the time-of-flight methodology.

The phase shift methodology measures the phase shift of the transverse magnetization of moving spins in the direction of a magnetic gradient. This phase shift is then correlated to a fluid velocity. The phase shift is caused by first applying a 90 degree radio frequency to the fluid of interest. This causes the protons to spin in phase until a magnetic gradient is applied. The linear magnetic gradient causes the precession frequency of the spins to be different from one location to another.

After the magnetic gradient is removed, the precession frequency of the spins equalize but having different phases. The shift in phase can then be correlated to a fluid velocity in the direction of the magnetic gradient.

The time of flight method is a useful way of producing a graphical representation of molecular motion. This technique uses the dispersion of the transverse magnetization in a plane by a large amplitude pulse followed by the imaging of the spins in that plane a short time later. The cross sectional plane of interest is first marked by an excitation frequency and then imaged after a small change in time. One may find velocities at each location by the change in displacement between excitation and subsequent imaging divided by the time between the excitation and the following imaging. One may adjust the thickness of the measurement plane in this technique by varying the radio frequency bandwidth and the gradient of the magnetic field that is applied during the period of the radio frequency excitation.

2.3.1.2 Gamma densitometer

The gamma densitometer works on the principle that water or other liquids attenuate a gamma beam more than a gas such as air or steam. The gamma densitometer requires a gamma source such as ^{137}Cs and a gamma scintillator with appropriate photodetector, preamplifier, counter, high voltage source and discriminator. One of the main advantages of this system is that it does not require transparent piping or special fluid limitations. A gamma densitometer can give very accurate measurements for line averaged void fraction and therefore is a useful tool for the calibration of other void fraction measurement instruments. Since a radioactive source is necessary, special requirements such as shielding and limiting exposure to people must be enforced. Because of the radiation and the amount of equipment required, gamma densitometers are typically only used short term as a calibration device for other instruments. A diagram of a gamma densitometer setup

is shown in Figure 2.3 with the darker color being the void fraction measurement area.

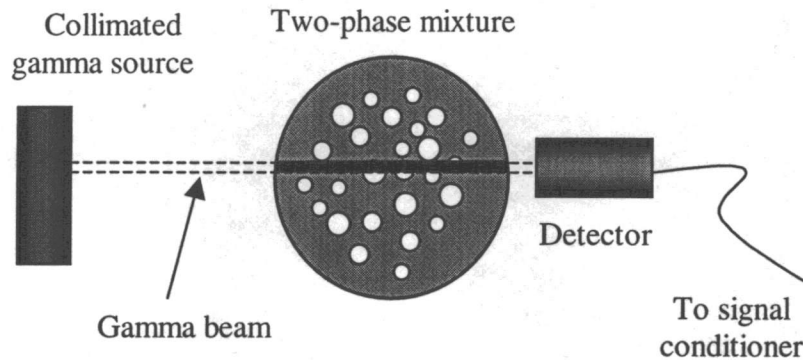


Figure 2.3: Gamma densitometer measurement

The line averaged void fraction is measured by first counting the number of counts in a specified time with only liquid in the pipe. Then one obtains the number of counts in over the same period with only gas present in the pipe. Once these two values are known one can measure the void fraction of a two-phase mixture. The line averaged void fraction at a particular location is related to the count rate by equation (2.15).

$$\bar{\alpha}^l = \frac{\ln\left(\frac{I_{2\phi}}{I_f}\right)}{\ln\left(\frac{I_g}{I_f}\right)} \quad (2.15)$$

Where $I_{2\phi}$ is the two-phase mixture count rate, I_f is the count rate for just the fluid and I_g is the count rate for just the gas. Since, with gamma densitometry, one counts particles, counting statistics apply. The count rate error goes as \sqrt{N}^{-1} where

N is the total number of counts for fluid, gas, or mixture. This means to have a count rate error of 1%, one must obtain a minimum of 10,000 counts. The time that it takes to reach this many counts is dependant on the strength of the source, geometry, and the detector efficiency.

2.3.1.3 Ultrasonic techniques

There are two main types of two-phase flow ultrasonic measurement techniques. These include ultrasonic pulse imaging and ultrasonic Doppler velocimetry (Morriss and Hill, 1993).

Ultrasonic pulse imaging is available in either one or two dimensions and works like those used in the medical industry. The ultrasonic pulse technique may use a separate transmitter and receiver or use the same unit to transmit a pulse and then wait a short time while receiving the reflected pulse before transmitting again. The received pulse intensity is plotted against time in order to create an image in one dimension. The receive pulse intensity is many times displayed onscreen with a raster line with the brightness proportional to the received pulse intensity. This image is typically plotted onscreen as intensity versus distance instead of time. This is an easy conversion since the speed of sound in the medium is known. The two-dimensional pulse echo is similar to the one-dimensional technique except for the fact that the transducer is swept continuously through an 80° arc. This produces a two dimensional pie shaped image of the flow at a given time and is the technology often seen in the medical industry. One of the main problems with ultrasound is proper processing to the received signal. One must eliminate signals that are reflected off the pipe as well as background noise. There is also a trade off between maximum imaging depth and the imaging resolution, thus this technique will not work well on large diameter pipes with the spatial resolution that is required.

The other ultrasonic measurement technique that may be applied to two-phase flow measurement is Ultrasonic Doppler Velocimetry. This technique is very

similar to Laser Doppler Velocimetry (LDV) except this technique uses the Doppler shift of ultrasonic sound instead of light to determine velocity. Since this technique uses sound instead of light, neither the piping nor the fluid needs to be optically transparent. However, the ultrasonic beam is much wider than that of a laser so there is a decreased spatial resolution over using LDV.

Both of these techniques have been successfully applied to slurry flows with a relatively high amount of solid particles. These techniques are both relatively new to gas-liquid two-phase flows and have been used with good success. The problem with ultrasound is that it only works for a limited range of void fractions. If the void fraction is too small, the reflected signal will either not be able to image the bubbles or measure their velocities. If the void fraction is too large, most of the ultrasonic energy will be absorbed or scattered by the bubbles and the received signal will not be distinguishable from background noise. Ultrasonic measurement techniques currently have an upper limit void fraction of about 12 percent in order to function correctly. One will typically not run into the lower void fraction limit unless one is dealing with void fraction that are much less than 1 percent.

2.3.1.4 Flush mount impedance probe

The flush mount impedance probe is used to measure and area averaged void fraction or equivalently liquid level in a horizontal section. The flush mount impedance probe works in the same manner as other impedance probe but the electrodes are set flush in machined grooves of electrically insulated material. This allows for measurement of the void fraction without penetrating the pipe wall with light, gamma rays, or ultrasonic sound waves but still has the benefit of being non-intrusive and thereby not disrupting the flow. The main disadvantage to the flush mount impedance probe is that only void fraction can be measured. The probe will not tell one anything about velocity, bubble size or interfacial area. The electrodes are usually applied with an alternating current voltage source since direct current

tends to be slow and inaccurate. Since the impedance of the probe varies with the amount of liquid within the plane of measurement versus the amount of air within that plane, the current flowing through the probe is directly related to the area averaged void fraction within that plane. The probe uses a current sensing amplifier to measure the current that flow through the probe and produces an output voltage. This signal is then rectified and put through a low pass filter to remove the carrier wave. This results in an output voltage that is inversely proportional to the void fraction. A diagram of one type of flush mounted conductivity/impedance probe is shown in Figure 2.4. The black lines in the figure represent the electrodes that are mounted flush around the perimeter of the pipe.

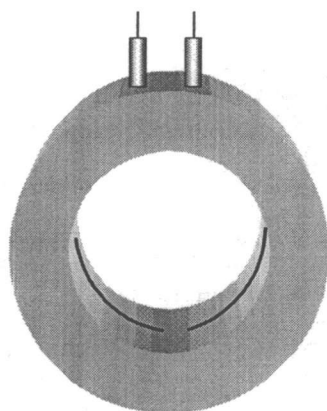


Figure 2.4: Flush mount conductivity probe

2.3.1.5 Photographic method

The photographic method can use a film or digital camera. However, the digital camera is much less labor intensive since the collected images can directly be passed into an image processing program such as MATLAB with the image

processing toolbox where void fraction can directly be measured. It is also possible to measure bubble velocity with this method if multiple frames are collected and the frame rate is known. This method requires that the void fraction is low and the piping and fluid are optically transparent. Lighting is also an issue since stray reflections or shadows created by the bubbles can result in errors in the image processing measurement. The photographic method also has the ability of measuring bubble size and velocity as long as there is some known reference length within the view. However, if the pipe is curved, one will run into problems in determining bubble size due to the magnification created in the direction of curvature. Typically, a water filled jacket with flat sides is placed around the section of interest. This cancels out the curvature effects of the pipe and allows one to record an undistorted view of the flow. The photographic method is an inexpensive method using anything from a still film camera to a high-speed digital camera. The photographic method is useful for calibrating other types of probes at a low void fraction as well as being able to determine the shapes of the bubbles and for observing bubble coalescence and breakup. The photographic method is useful in conjunction with other types of probes since the processing of the images can be difficult and the photographic method only works over a small range of void fraction but the photographic method does over additional information that many other types of measurement cannot provide. Wilmarth and Ishii (Wilmarth and Ishii, 1997) applied the photographic technique along with image processing to determine the void fraction and interfacial area concentration in narrow rectangular vertical channels and compared the measurements to the drift flux model. Since the sides of the channels were flat, Wilmarth and Ishii did not experience image distortion of the bubbles due to curvature effects. Many other authors have used the photographic method to analyze bubble shapes or to check their probe measurements with another source in other papers. However, researchers usually do not use the photographic method as their primary measurement technique because of the limitations that the photographic method possesses. Before image processing, the photographic technique was very tedious and slow going since all of the image

measurements were done by hand. Today, with the image processing software, the photographic method is more accurate and faster than at previous times. However, one must be careful with lighting since the human eye can distinguish a reflection or a shadow from an actual bubble but the image processing software can be fooled by reflections or shadows and give incorrect results.

2.3.1.6 Light transmission

The light transmission method relies upon the attenuation of light as it passes through a pipe in the radial direction. Because of this requirement, the piping and fluid must be optically clear. In addition, this method is limited to areas in which the void fraction is low. The light transmission technique works by passing a laser beam through a pipe and by measuring the intensity of the light on the other side with a photodetector (Mudde et al. 1992). The system must be first calibrated by having the pipe all liquid and then all gas. This method has limited accuracy for void fraction measurement due to the fact that the intensity of the light is a function of the amount of liquid or gas the light passes through and also the number of bubble-liquid interfaces that the light must pass through. In addition, scattering of the light from other bubbles and surfaces into the photodetector is also a source of error. Due to these limitations, this technique is rarely used in research applications.

2.3.1.7 Particle image velocimetry (PIV)

Particle Image Velocimetry (PIV) is a non-intrusive, two or three-dimensional, instantaneous velocity measurement technique. The measurements are performed by seeding the flow of a fluid with small spherical tracer particles and illuminating a region of interest with a thin sheet of laser light. PIV systems measure velocity by determining particle displacement over time using a double-pulsed laser technique.

A laser light sheet illuminates a plane in the flow, and the positions of particles in that plane are recorded using a digital or film camera. A fraction of a second later, another laser pulse illuminates the same plane, creating a second particle image. From these two particle images, PIV analysis algorithms obtain the particle displacements for the entire flow region imaged, and gives velocity information. Because PIV is an optical imaging technique, it suffers from the same limitations as other imaging techniques such as the photographic method and light transmission method. One also has to add tracer particles to the flow, which may disrupt the flow. PIV is limited to very low void fractions and requires the use of clear piping. Flow properties such as vorticity and velocity are obtained for the entire region. This technique is useful for measurements of velocity but lacks the ability to provide other important two-phase flow parameters such as interfacial area concentration and void fraction.

2.3.1.8 Laser Doppler velocimetry (LDV)

Laser Doppler Velocimetry is a proven technique that provides an accurate measurement of fluid velocity. Laser light illuminates the flow, and light scattered from particles in the flow is collected and processed. In practice, a single laser beam is split into two equal-intensity beams, which are focused at a common point in the flow field. An interference pattern is formed at the point where the beams meet.

Particles moving through the measuring volume scatter light of varying intensity, some of which is collected by a photodetector. The resulting frequency of the photodetector output is related directly to particle velocity. If additional laser beam pairs with different wavelengths are directed at the same point, two or three velocity components can be determined simultaneously. Typically, the blue and green or blue, green, and violet lines of an argon-ion laser are used for multiple velocity component measurements.

LDV provides velocity data at a single point. Using a traverse system to move the laser light source point-by-point makes it possible to perform an area analysis. LDV is very accurate and can provide excellent spatial resolution that can provide a technique to validate velocity and turbulence results from Computation Fluid Dynamics (CFD) codes. LDV is capable of measuring velocities from the natural convection range all the way to supersonic flow. LDV is similar to PIV in that it can only provide information on velocity and vorticity of the flow and lacks the ability to provide measurement of interfacial area and void fraction. One of the main advantages to LDV however is the ability to measure multiple velocity components simultaneously. This can provide valuable information on the direction of bubble motion as well as having the potential to accurately measure bubble oscillations. The downfall of this system is the equipment needed to process the received signal can be expensive and complex. Argon-ion lasers are relatively expensive and require a large power supply due to their low efficiencies. Both of these requirements can make the LDV system too expensive to use for some applications. In addition, the LDV system will only work well for relatively low void fractions as well as having the requirement of needing transparent piping and fluids.

2.3.2 Intrusive techniques

Intrusive techniques offer almost the only possibility of measuring two-phase flow parameters locally. These techniques allow for measurement of void fraction distributions, bubble size and velocity distributions as well as interfacial area. Although intrusive techniques can disturb the flow, these techniques offer inexpensive and accurate measurement of two-phase flow parameters. When designing an intrusive probe, it is important to miniaturize the design of the probe as much as possible to reduce the amount of influence the probe has on the flow.

Table 2.3: Typical intrusive bubbly/slug flow measurement techniques

Measurement Techniques	Measurement	Types of Measurement	Advantages	Limitations
Needle type optical probe	Local	Void fraction, interfacial area, velocity	Good response, works over wide range of void fractions	Mechanically sensitive, fluids must have different index of refractions
Wire mesh conductivity probe	Several points	Void fraction distribution	Many simultaneous measurement points	Highly intrusive
Double or multi-sensor conductivity probe	Local	Void fraction, interfacial area, individual bubble size	Inexpensive, offers many two-phase flow parameters	Usually homemade, needs conducting fluid
Acoustic Bubble Spectrometer	Volume	Void fraction, bubble size distribution	Inexpensive, works for many fluids, give bubble size distribution directly	Can disrupt flow since hydrophones must be installed in the liquid, temperature and pressure limitations because of hydrophones in the fluid

2.3.2.1 Needle type optical probe

The needle type optical probe is similar to the needle type conductivity probe in that both probe pierce the bubble in order to measure it. However, the optical probe relies on the difference between the index of refraction of each fluid instead of relying upon difference in conductance. The needle type optical probe works by sending a modulated laser or Light Emitting Diode (LED) light down an optical fiber and into the glass needle tip. The needle has been polished at an angle that is between the critical angle of water and that of air. Figure 2.5 contains a schematic of the operation principle of the optical needle probe.

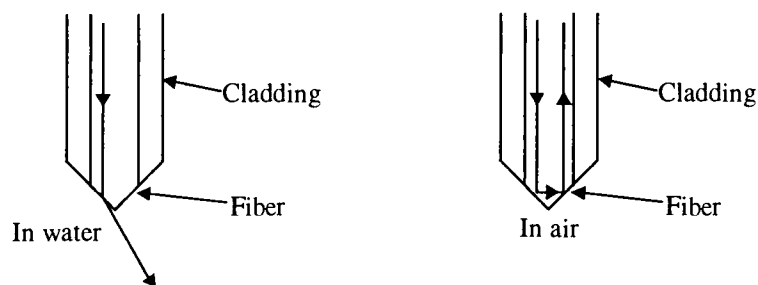


Figure 2.5: Optical needle probe operation

If water is present, the angle of the needle tip is greater than the critical angle for a glass/water interface so the light exits the probe tip. However, if air is present, the angle of the tip is less than the critical angle of a glass/air interface so the light is reflected back up the probe into another optical fiber. This light falls upon a photodetector, which converts the light into an electrical signal. This signal is put through a rectifier and low pass filter to remove the modulating frequency which results in two distinct output voltages; one for air and other for water. If two needles are present, one can determine all of the two-phase parameters that can be obtained with a double sensor conductivity probe. The needle type optical probe typically has much smaller needle diameters than the conductivity probe and therefore is less intrusive. The main disadvantage to the needle type optical probe is that it is very fragile and cannot withstand high flow rates. In addition, one can get false signals from this style of optical probe from particles in the water as well as the possibility of improper operation due to dust or scratches on the needle tip. A diagram of how a needle type optical probe works is shown in Figure 2.6. If there were no bubble present, the laser beam would exit through the tip of the needle tip. This would result in the beam not being returned to the photodetector. This results in a high signal from the photodetector when gas is present and a low signal when liquid is present.

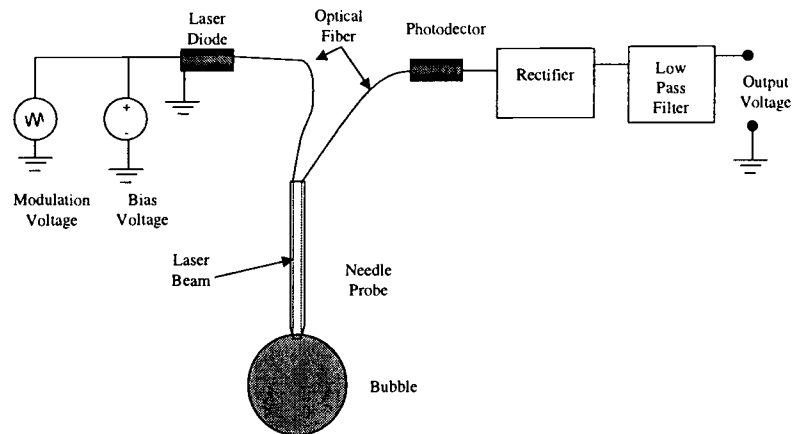


Figure 2.6: Needle type optical probe diagram

Rinne and Loth (Rinne and Loth, 1996) used this technique to determine local bubble frequency, local void fraction, and local residence time on the sensor for bubbly flow in a vertical pipe with a sudden expansion. They also incorporated a pair of similar sensors in this study that were mounted horizontally in order to determine local bubble velocity. Rinne and Loth also included the photographic technique to cross calibrate the void fraction measurements of the probe as well as to verify bubble shapes.

2.3.2.2 Wire mesh conductivity/impedance probe

Wire mesh type impedance probes are constructed using two wire grids separated by a small distance. One of these planes is the transmitter plane and the other plane is the receiver plane. The transmitting and receiving plane are rotated 90 degrees from each other. One of the transmitting wires is selected with a multiplexing circuit and applied with an excitation voltage. The currents through

each of the receiving wires, which cross the excited transmitter wire, are measured using a current to voltage converter along with a sample and hold circuit and an analog to digital converter. The receiving line in which current is detected, liquid is present. If little or no current is detected, one knows that gas is present at that point. This process is then repeated by exciting the next transmitter wire and so on. One of the main difficulties with this probe is cross talk between parallel wires. This occurs when one of the wires is at a higher potential than the surrounding wires, this results in current flowing to lines in which no current should be present. The only way to eliminate this effect is to make the impedance of the driving and receiving circuit much less than the impedance of the fluid. Typically, these probes are applied with alternating current instead of direct current because direct current will cause measurement errors due to electrolysis. The alternating current can be sine, square or triangle wave as long as no direct current components of the wave exist. The wire mesh sensor has the advantage of measuring many points in the flow simultaneously and getting a void fraction distribution directly. However, due to the large number of transmitting and receiving lines, this probe type is highly intrusive so one cannot be certain that the measurements obtained by this probe would be applicable to the flow with the probe not in place. A simplified version containing 16 measurement points of the wire mesh sensor is given in Figure 2.7. If one were to use alternating current for this circuit one would have to add a rectifier and a low pass filter between the current to voltage converters and the sample and hold circuit to allow for demodulation of the signal. These additional modifications are not shown in Figure 2.7. This circuit can be expanded to result in hundreds of measurement points within the cross section. An example of the types of measurement and imaging that can be performed with this type of probe is given in Reinecke et al. (Reinecke et al., 1998). Reinecke et al. were able to take a cross-sectional image in horizontal slug flow every nine milliseconds with this technique.

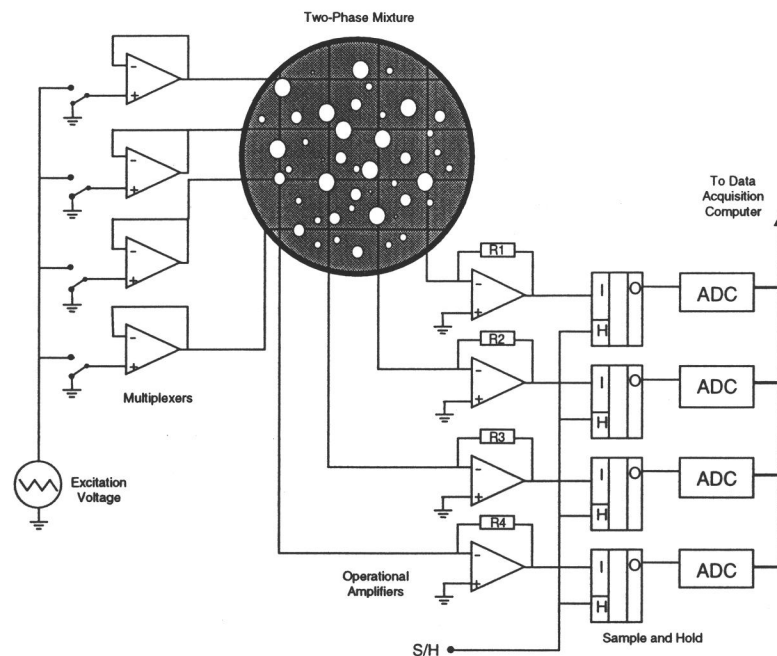


Figure 2.7: Wire mesh sensor diagram

2.3.2.3 Double or multi-sensor conductivity probe

The double or multi-sensor conductivity probe is currently the most popular method for obtaining local two-phase flow parameters. Needle type conductivity/impedance probes are popular due to that fact that they do not require optically clear piping or fluid, are inexpensive to construct, will work over a large void fraction range, as well as providing many two-phase flow parameters from a single probe. These probes only require that the liquid phase is much more conductive than the gas phase and are limited to temperature and pressure limits based on construction methods and materials. Since, there are no commercially

available multi-sensor conductivity probes, researchers must rely on their own hand-constructed design. This can make it difficult to place the probe tips accurately. Thus, each probe is unique even with a given construction technique. Some of the properties that the impedance probe must exhibit include; the sensors must be highly conducting and electrochemically stable to the surrounding fluid and the probe must be strong enough to withstand the forces of the flow. In addition, the sensor diameter must be small relative to the bubble diameter and the body of the probe must be as small as possible in order to avoid distortion of the bubble's interface during measurement.

With a double sensor conductivity probe, one can measure interfacial area concentration, but one needs to make several assumptions. These assumptions include: (1) the number of measured interfaces is large; (2) $|v_{ij}|$ is statistically independent of the angle between the flow direction and the normal direction of the j^{th} interface; (3) the interfaces are composed of spherical bubbles; (4) the probe passes through every part of a bubble with equal probability; and (5) transverse direction components of v_{ij} are random. This is why conductivity probe with four or sometimes more sensors are constructed. A four-sensor probe is like having three double sensor probes grouped together with one common leading sensor. This allows for velocity measurements at several points on each bubble, resulting in the ability to determine interfacial area without making so many assumptions. Like the double sensor probe, other multi-sensor probes have the possibility of a bubble either missing one of the probe tips or contacting a leading and trailing sensor simultaneously. This problem is discussed further in section 3.2. However, this problem is magnified in probe with more than two probe tips. One must have additional criteria for specifying when a bubble is missing due to the increased number of probe tips that the bubble must encounter. This problem can be eliminated by reducing the size of the probe and the lateral spacing between the leading and trailing sensors. However, the size of these conductivity probes cannot be reduced further in size with the current hand-construction techniques. One

requires the use of machinery to reduce the size of these multi-sensor probes to a size that will return reliable results in which very few bubbles are missing. This reduction in size also has the advantage of reducing the intrusiveness of the probe on the flow. The reduction in size of these probes also has the disadvantage of requiring a higher data acquisition rate especially for determining velocity since there is less distance between the probe tips. If the size of the probe is reduced enough, the probe will be essentially non-intrusive and offer researchers and industry an inexpensive way of measuring local two-phase flow parameters.

The theoretical relation to determine interfacial area concentration for a double sensor probe is given by several researchers (Wu and Ishii, 1999; Revankar and Ishii, 1992; Leung et al., 1995; Hibiki et al., 1998; Hibiki and Ishii, 1999; Hogsett and Ishii, 1997; Hibiki et al., 2001a). The needle type impedance probe works by each sensor acting as an independent phase identifier. This accomplished by passing a current through each one of the sensors to a common ground. Since, in an air-water system, the water is a much better conductor than air, the current through a sensor is much greater for water than for air. In fact, if the system uses a direct current, the resultant current that passes through the sensor when air is present is zero since the circuit is open. Having the ability to detect each phase and the time at which each phase is present, one can determine many important two-phase flow parameters at the location of the probe. These parameters include: void fraction, bubble chord length, interfacial velocity, and interfacial area. The time averaged local interfacial area concentration is given by

$$\bar{a}_i = \frac{1}{T} \sum_j \frac{1}{|v_{ij}| \cos \varphi_j} \quad (2.16)$$

where φ_j is the angle between the velocity of the j^{th} interface, v_{ij} , and the direction of the surface normal vector and T is the total sampling time. Equation 2.16 is summed over the total number of interfaces, j , during the sampling period.

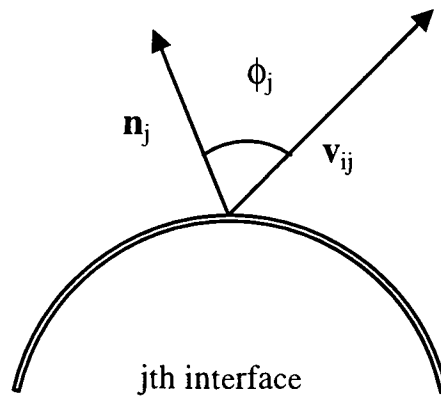


Figure 2.8: The j th interface of a bubble

If one then assumes that $1/|v_{ij}|$ and $1/\cos\phi_j$ has no correlation, one can simplify equation (2.16) to:

$$\bar{a}_i{}' = 2 N_t \frac{\overline{1}}{|v_i|} \cdot \frac{\overline{1}}{\cos\phi} \quad (2.17)$$

where N_t is the total number of bubbles which pass the probe per unit time. The factor of two is to account for the fact that each of the bubbles has two interfaces associated with it. If one then applies the required assumptions on the shape of the bubbles, lateral motion, and probabilities of the probe piercing different portions of the bubble, equation (2.17) can then be written as:

$$\bar{a}_i{}' = 2 N_t \left\{ \frac{\sum_j \frac{1}{|v_{szj}|}}{\left(\sum_j \right)} \right\} I(\omega_0) = 2 N_t \frac{\overline{1}}{|v_{sz}|} I(\omega_0) \quad (2.18)$$

where the correction factor, $I(\omega_0)$, according to Hibiki et al. (Hibiki et al., 1998), is:

$$I(\omega_0) = \frac{\int_0^{\omega_0} \left[\int_0^{\pi/2} \left\{ \int_0^{2\pi} g(\omega_0) \frac{\sin\phi}{\pi} d(\psi-\theta) \right\} d\phi \right] d\omega}{\int_0^{\omega_0} \left[\int_0^{\pi/2} \left\{ \int_0^{2\pi} g(\omega_0) \frac{\sin\phi \{ \cos\omega \cos\phi + \sin\omega \sin\phi \cos(\psi-\theta) \}}{\pi} d(\psi-\theta) \right\} d\phi \right] d\omega} \quad (2.19)$$

In the above equations, the terms v_{szj} , ω , ω_0 , and $g(\omega_0)$ are the velocity of the j^{th} interfaces passing through the probe in the direction of flow, the angle between the velocity vector of the j^{th} interface and the velocity vector of the mean flow direction, the maximum angle of ω , and the probability density function of angle ω respectively. In addition, the terms ϕ , θ , and ψ are the angles between the probe and a set of transformed coordinates based on z' being in the direction of the bubble velocity vector. Once the integrals are performed on equation (2.19), one is left with a much simpler equation for $I(\omega_0)$.

$$I(\omega_0) = \frac{2}{\int_0^{\omega_0} g(\omega) \cos\omega d\omega} \quad (2.20)$$

By assuming a functional form for $g(\omega_0)$, one may then arrive at the following equation for $I(\omega_0)$:

$$I(\omega_0) = \frac{\omega_0^3}{3(\omega_0 - \sin\omega_0)} \quad (2.21)$$

In order for these equations to be useful for the measurement of time averaged interfacial area concentration, one must try to relate ω_0 to a measurable quantity. This is accomplished by including the assumption that the root mean square of the z

component fluctuations in the interfacial velocity is equal to that of the x and y component root mean square velocity fluctuations. One may find ω_0 and thus the time averaged interfacial area concentration by the following equation.

$$\frac{3}{2\omega_0^2} \left(1 - \frac{\sin 2\omega_0}{2\omega_0} \right) = \frac{1 - \left(\sigma_z^2 / |v_{iz}|^2 \right)}{1 + 3 \left(\sigma_z^2 / |v_{iz}|^2 \right)} \quad (2.22)$$

In the above equation, σ_z is the root mean square of the velocity fluctuations in the flow direction and v_{iz} is the z component of the interfacial velocity. However, the above analysis performed by Hibiki et al. (Hibiki et al., 1998) does not consider the missing bubble case. The missing bubble case should however be included since these missed bubbles contain additional interfacial area.

Wu and Ishii (Wu and Ishii, 1999) did include the missing bubble case in their analysis. They numerically obtained a set of three calibration factors that would be able to be used to bridge the mean measurable parameter to the interfacial area concentrations carried by the missed bubbles, measured bubbles, and their combination. Equation 2.23 shows the time average interfacial area concentration that includes missing bubbles.

$$\bar{a}_i^t = \frac{2N_b}{T} \left[\frac{N_b - N_{miss}}{N_b} \left(\frac{1}{|v_i| \cos \phi} \right)_{normal}^t + \frac{N_{miss}}{N_b} \left(\frac{1}{|v_i| \cos \phi} \right)_{miss}^t \right] \quad (2.23)$$

Where N_b is the total number of bubbles detected, N_{miss} is the number of missing bubbles, and T is the total sampling time. The inverse of the average measured velocity is given in equation (2.24).

$$\overline{\left(\frac{1}{v_{sz}}\right)}_{\text{normal}}^t = \frac{1}{N_b - N_{\text{miss}}} \sum_j \left(\frac{\Delta t}{\Delta s}\right)_j \quad (2.24)$$

The theoretical calibration factors used by Wu and Ishii are given in equations (2.25)- (2.27).

$$f_{\text{total}} = \frac{\overline{\left(\frac{1}{|v_i| \cos \phi}\right)}_{\text{total}}^t}{\overline{\left(\frac{1}{v_{sz}}\right)}_{\text{normal}}^t} \quad (2.25)$$

$$f_{\text{normal}} = \frac{\overline{\left(\frac{1}{|v_i| \cos \phi}\right)}_{\text{normal}}^t}{\overline{\left(\frac{1}{v_{sz}}\right)}_{\text{normal}}^t} \quad (2.26)$$

$$f_{\text{miss}} = \frac{\overline{\left(\frac{1}{|v_i| \cos \phi}\right)}_{\text{miss}}^t}{\overline{\left(\frac{1}{v_{sz}}\right)}_{\text{normal}}^t} \quad (2.27)$$

Finally, Wu and Ishii (Wu and Ishii, 1999) found that if the bubble sizes ranged between 1.2 and 3 times the probe spacing, the time averaged interfacial area concentration could be found by equation (2.28).

$$\bar{a}_i^{-t} = \left(\frac{2N_b}{\Delta s T} \right) \left[2 + \left(\frac{v'_{sz}}{\bar{v}_{sz}^{-t}} \right)^{2.25} \right] \left[\frac{\sum_j (\Delta t_j)}{N_b - N_{miss}} \right] \quad (2.28)$$

In equation (2.28), v'_{sz} is the bubble velocity fluctuation and \bar{v}_{sz}^{-t} is the average bubble velocity.

Once the interfacial area concentration and void fraction are known, one can determine the time average Sauter mean diameter by using:

$$\bar{D}_{Sm}^{-t} = \frac{6\alpha^{-t}}{\bar{a}_i^{-t}} \quad (2.29)$$

The determination of the time averaged void fraction as well as the time averaged interfacial velocity for a double sensor conductivity probe is given in section 3.2.

A similar treatment as stated above may be applied to the four-sensor conductivity probe. According to Revankar and Ishii (Revankar and Ishii, 1993), the interfacial area concentration for a four-sensor probe measurement is given by:

$$\bar{a}_i^{-t} = \frac{1}{T} \sum_j \left\{ \left(\frac{1}{v_{s1j}} \right)^2 + \left(\frac{1}{v_{s2j}} \right)^2 + \left(\frac{1}{v_{s3j}} \right)^2 \right\}^{1/2} \quad (2.30)$$

if the front and three rear sensors are arranged to make an orthogonal system. The z component of the interfacial velocity, v_{skj} , is given in a similar manner as the double sensor probe and is given by the following equation:

$$v_{ski} = \frac{\Delta s_k}{\Delta t_{kj}}, \quad k = 1, 2, 3. \quad (2.31)$$

In the case of multiple sensor probes, Δs_k is the distance between the leading probe tip and each individual rear probe tip.

No matter the geometry, conductivity/impedance probes can operate in two major modes. These modes include a purely conductive mode or an impedance mode. For a purely conductive mode, a direct current source such as a battery is used to power the probe and the resulting current that passes through the probe is then converted to a voltage via a load resistor. This is the most simplistic mode of operation requiring only the use of the probe, a battery, and a load resistor. However, the purely conductive mode has low response and the resulting conductivity is a function of temperature and ion concentration in the liquid. This requires the use of properly selected signal thresholds to separate a signal resulting from a bubble from that of noise. For a purely impedance mode, a high frequency alternating current source is used so that the impedance of the capacitive portion of the probe dominates over the resistive portion of the probe. Since, the impedance is frequency dependent, one requires a high frequency in order for the impedance of the capacitive term to dominate over the resistive term. The current that then passes through the probe is then converted to a voltage with an active current to voltage converter circuit. This signal is then rectified and passed through a low pass filter to remove the carrier wave. Because one needs to selectively remove the carrier signal from the signal fluctuations for the incoming bubbles, one needs to have the carrier frequency to be at least ten times that of the data acquisition rate. The purely impedance mode has the advantage that the impedance is only determined by frequency and capacitance. The capacitance is only a function of the electrode area, electrode spacing, and the dielectric constant of the liquid or gas. This results in a measurement that is independent of temperature, ion concentration, etc. However, this mode of operation has the disadvantage of being more complicated and one may have difficulty with the capacitance in the wire that connect the probe to the signal processing circuit. This requires the use of cable designed for high frequency use and short lengths of cables are often required.

One may use a single sensor conductivity probe to measure local void fraction or the number of bubbles that pass the probe tip. However, probes with two or more sensors have these abilities plus the ability to measure individual bubble lengths,

velocities, and interfacial area. Multi-sensor conductivity probes typically have one leading sensor and one or more trailing sensors. The bubble velocity is determined by the transient time of the bubble from the leading sensor to the trailing sensor since the distance between the sensors is known.

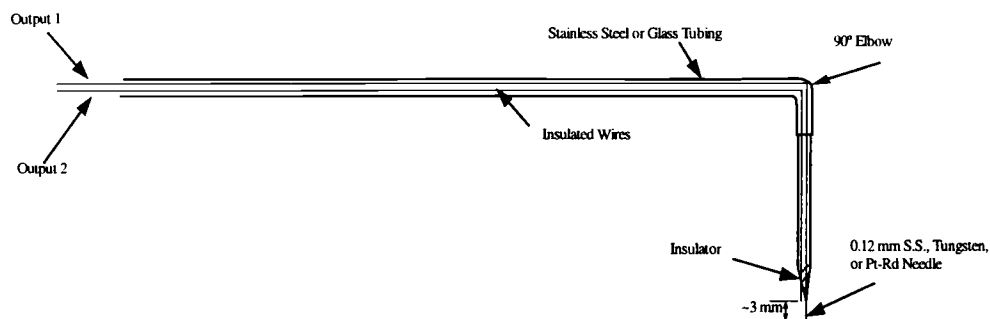


Figure 2.9: General double sensor conductivity probe design

Kocamustafaogullari et al. (Kocamustafaogullari et al., 1994a) used three double-sensor conductivity probes at different locations along a 50.8 mm diameter horizontal pipe to study the profiles of void fraction, interfacial area, and velocity for horizontal two-phase flow. Each of the probes was placed in a custom instrumentation mount that allowed for traversing the probe across the diameter of the pipe as well as allowing for rotation of the probe. These two abilities allow for the creation of cross sectional mapping of important two-phase flow parameter. The ability for the probe mount to be able to rotate is especially important in horizontal flow since the parameters such as void fraction are highly asymmetric in horizontal flows due to buoyancy allowing the migration of the bubble towards the top of the pipe. Kocamustafaogullari et al. measured 23 points along the pipe diameter for each rotation of 22.5° of the probe with respect to the pipe. This resulted in 108 measurement points for each probe location for each flow rate tested. Although, it

would seem that this many measurement points would be time consuming, each experiment did not require much time since Kocamustafaogullari et al. only sampled data for 1 second at 20 kHz for each probe location. They found that in horizontal flow, one does not obtain fully developed flow as in vertical or inclined flows due to the constant acceleration due to pressure changes caused by wall friction. Kocamustafaogullari et al. presented their data as three-dimensional plots for each flow condition and each axial measurement location. One can see from these plots the development of void fraction, interfacial area concentration, and interfacial velocity along the length of the pipe. A second paper by Kocamustafaogullari et al. (Kocamustafaogullari et al., 1994b) is similar to the work in Kocamustafaogullari et al., 1994a except for the fact that in this paper Kocamustafaogullari et al. concentrated on just traversing the probe across the pipe with no rotation of the probe with respect to the pipe. They then compared the axial and radial profiles of void fraction, interfacial area concentration, and Sauter mean diameter to the predicted values for these flow parameters.

2.3.2.4 Acoustic bubble spectrometry

The Acoustic Bubble Spectrometer® (ABS) is an acoustic based device produced by Dynaflo Incorporated that measures bubble size distributions and void fractions in liquids. The ABS is less expensive than optics-based measurements and is insensitive to solid particles in the flow as being bubbles. The ABS can be used in a wide range of two-phase flow applications where one requires the measurement of the bubble size distribution, and the volume averaged void fraction. Base of the bubble size distribution measurement and the void fraction measurement, one can estimate interfacial area concentration by assuming a bubble shape. The instrument can provide the data in near real time, thus making it suitable for process or time varying applications. The device extracts the bubble population from acoustic measurements made at several frequencies. It consists of a set of two

hydrophones or transducers connected to a set of boards resident on a computer. A data board controls signal generation by the first hydrophone and signal reception by the second hydrophone. Short monochromatic bursts of sound at different frequencies are generated by the transmitting hydrophone and received by the second hydrophone after passage through the bubbly liquid. These signals are then processed and analyzed utilizing specialized software algorithms. This allows one to obtain the attenuation and phase velocities of the acoustic waves as well as the bubble size distribution. The onboard PC cards' signal generation and data acquisition hardware is synchronized to control the measurements and perform the data analysis.

Bubble size distribution measurements using the ABS are based on a dispersion relation for sound wave propagation through a bubbly liquid. A multiphase fluid model for sound propagation through bubbly liquids is combined with a model for the bubble oscillations, including various damping modes. The combined model relates the attenuation and phase velocity of a sound wave to the bubble population or size distribution. Because the hydrophones must be facing each other within the flow, this is an intrusive system and thus would perform best in a case in which the liquid flow is stagnant. In addition, with the hydrophones needing to be in the flow, temperature and pressure limits are placed on this measurement technique based on the properties of the hydrophones. One of the main drawbacks to this system is since it is acoustically based; this system will only work for relatively low void fractions, namely the bubbly flow regime. This system does not require that the fluid or piping be transparent or that the fluid be electrically conductive as with other types of two-phase flow measurement techniques. The ABS system also has the advantage of being able to directly measure the bubble size distributions within a volume of mixture directly instead of needing to traverse a probe to get several local measurements to try to reconstruct the bubble size distribution over an area or a volume.

2.4 INTERFACIAL AREA TRANSPORT EQUATION

As discussed in previous sections, interfacial area or the interfacial area concentration is vital to the development of two-phase flow modeling. Several researchers have published papers on one and two group interfacial area transport equations (Hibiki and Ishii, 1999; Hibiki and Ishii, 2000; Hibiki et al., 2001b; Morel et al., 1999; Wu et al., 1998). Typically, the interfacial area transport equations are based on a particle number densities model. The bubbles are broken up into two groups, the spherical/distorted bubble group and the cap/slug bubble group. Lafi and Reyes (Lafi and Reyes, 1991) incorporated a population balance approach as well as a Monte Carlo approach in determining bubble and droplet breakage and coalescence criteria. This would be a good basis on which one could develop conceptually how a bubble size distribution may change from containing only group one bubbles to a distribution which contains both group one and group two bubbles. The idea behind having an interfacial area transport equation is that with proper modeling one could determine the interfacial area concentration at the inlet of the section of interest and predict what the interfacial area concentration would be at different times and at different axial and radial positions. The transport equation consists of source and sink terms for interfacial area for each of the two groups. Examples of a source term would be bubble break up or a phase change from the liquid phase to the vapor phase. Examples of a sink term would be bubble coalescence or bubble collapse. In order to properly characterize the interfacial area transport equation, all of the source and sink terms must be fully understood and modeled correctly. The interfacial area sink terms that need to be properly described are coalescence due to random collision and the wake-entrainment process. For the interfacial area source terms, one can have bubble breakup due to turbulence impact, shearing off small bubbles from a larger bubble, or bubble breakup due to a surface instability. In addition to these source and sink terms, one could also have phase change as an additional source or sink term. Separate experiments as well as additional theoretical investigation is needed to identify and model the entire set of

possible source and sink terms in the interfacial area transport equation. Once these tasks are performed, this information can be combined with experimental results for interfacial area concentration to provide additional insight into the behavior of multiphase flow as well as allowing computer codes which model multiphase flow to become more accurate. Hibiki et al. (Hibiki et al., 2001b) created an interfacial area transport equation for bubbly flow in a small diameter pipe. They modeled the sink terms by just using wake entrainment. Hibiki et al. believed that since the bubble diameter is close to the pipe diameter, the lateral motion of the bubble would be restricted by the pipe wall and therefore coalescence due to random collision may be neglected. The interfacial area concentration source terms were neglected since at low liquid velocities, the amount of bubble breakup would be negligible. There was no phase change to deal with since this was an adiabatic air/water system. In addition, since only bubble flow was being studied, the two-group interfacial area concentration transport equation could be reduced to a one-group equation since cap or slug bubbles did not exist. The one group interfacial area transport equation may be given as (Hibiki et al., 2001b):

$$\begin{aligned} \frac{\partial a_i}{\partial t} + \frac{d}{dz}(a_i v_g) &= \frac{1}{3\psi} \left(\frac{\alpha}{a_i} \right)^2 (\varphi_B - \varphi_C + \varphi_P) + \left(\frac{2a_i}{3\alpha} \right) \left\{ \frac{\partial \alpha}{\partial t} + \frac{d}{dz}(\alpha v_g) \right\} \\ &= \Phi_B + \Phi_C + \Phi_P + \Phi_V \end{aligned} \quad (2.32)$$

where

$$\begin{aligned} \Phi_B &\equiv \frac{1}{3\psi} \left(\frac{\alpha}{a_i} \right)^2 \varphi_B \\ \Phi_C &\equiv \frac{1}{3\psi} \left(\frac{\alpha}{a_i} \right)^2 \varphi_C \\ \Phi_P &\equiv \frac{1}{3\psi} \left(\frac{\alpha}{a_i} \right)^2 \varphi_P \\ \Phi_V &\equiv \left(\frac{2a_i}{3\alpha} \right) \left\{ \frac{\partial \alpha}{\partial t} + \frac{d}{dz}(\alpha v_g) \right\} \end{aligned}$$

The terms a_i , t , v_g , z , ψ , and α denote the interfacial area concentration, time, gas velocity, axial position, bubble shape factor ($\psi = 1/(36\pi)$ for spherical bubbles), and the void fraction respectively. The terms ϕ_B , ϕ_C , and ϕ_P are the rates of change of the bubble number density due to bubble breakup, bubble coalescence, and phase change. The terms Φ_B , Φ_C , Φ_P , and Φ_V are the rates of change of the interfacial area concentration due to bubble breakup, bubble coalescence, phase change, and void transport respectively.

With all of the simplifications that Hibiki et al. used, the transport equation can be greatly simplified since many of the terms reduce to zero. Hibiki et al. found that the modeled interfacial area concentration transport equation could reproduce the axial interfacial area transport within an error of 11.1% for a 9.0 mm diameter tube with a superficial gas velocity of 0.013-0.052 m/s and a superficial liquid velocity ranging from 0.58 to 1.0 m/s.

Wu et al. (Wu et al, 1998) did some development with the interfacial area transport equation and then compared the one group theoretical equations to the experimental results for vertical bubbly flow. Wu et al. analyzed various methods of bubble breakup and bubble coalescence. They analyzed the important mechanisms for one group interfacial area transport. These mechanisms include: wake-entrainment induced bubble coalescence, bubble breakup due to turbulent impact, and random collision induced bubble coalescence. For two-group interfacial area transport, one must also include the shearing of small bubbles from large bubbles as well as the breakup of large bubbles due to surface instabilities. They found that the proposed models for bubble breakup and bubble coalescences compared well to the experimental data and that the adjustable parameters used in the theoretical modeling were within the range of expected physical values. However, since the data set that was compared only had measurements at three axial locations, more data will need to be gathered in order to finely tune the theoretical models adjustable parameters.

Several researchers have used the information gained using the theoretical development of the interfacial area transport equation and have compared the theoretical results with experimental results (Hibiki et al., 2001a; Hibiki and Ishii, 1999; Hibiki and Ishii, 2000). This sort of comparison could reveal missing areas within the theoretical result and could help to determine the rate of change of the bubble number density within the pipe as well as to characterize the transfer rates between the two bubble groups.

Leung et al. (Leung et al., 1995) performed several experiments to determine the axial development of interfacial area and void concentration profiles in a vertical bubble column. This produces a data set for one to compare the experimental results with the one group interfacial area transport equation. By employing a double-sensor conductivity probe, Leung et al. were able to measure the radial profiles of the void fraction, interfacial area concentration, Sauter mean diameter, bubble velocity, and bubble frequency at each axial location. Leung et al., unfortunately only took measurements at two different axial locations: one at the entrance to the test section ($L/D=8$) the other at a position far away from the entrance ($L/D=60$). This makes it difficult to determine how the interfacial area concentration is actually changing along the flow direction. Leung et al. found that the void fraction peak is near the wall in the entrance region for all of the test cases ran. They also found that in most of the flow rates that were used, the void profile remained saddle shaped even at $L/D=60$ but in one case the void fraction profile developed from saddle shaped at the entrance to a parabolic shape in the fully developed region. Leung et al. also compared their results to the drift flux model and found the distribution parameter, C_o , to be 0.7. This value is consistent with a near wall void peak profile.

Hibiki et al. (Hibiki et al., 2001a) also performed experiments to examine axial interfacial area transport in vertical bubbly flows. Hibiki et al. used three double-sensor conductivity probes located at $L/D=6.00$, 30.3, and 53.5 to determine the axial interfacial area transport. The probes were also set up to traverse the pipe in the radial direction and data was taken at fifteen different radial locations for each

flow condition specified. This allows for the creation of radial profiles for void fraction, interfacial velocity, and local interfacial area concentration. Hibiki et al. also employed the use of a hotfilm anemometer to measure local liquid velocity and turbulence. They also observed some of the same phenomena as Leung et al. (Leung et al., 1995) such as the saddle shaped void profiles in the developed region. However, Hibiki et al. also observed situations in the transitional regime in where the void profile exhibited a near wall peak as well as a centerline peak. These transitional regions occur as the flow is transferring from a saddle shaped void profile to a void profile that is parabolic in shape.

Hibiki and Ishii (Hibiki and Ishii, 2000) provided involved theoretical development of the two-group interfacial area transport equation. They then applied this theoretical formulation and performed a comparison with experimental results. The experimental setup is essentially identical to that used in Hibiki et al, 2001a. The difference between this particular set of experiments for the axial development of interfacial area concentration is that flow rates which contained cap/slug bubbles were used in order for comparison against their theoretical development of the two-group interfacial area concentration transport equation. Hibiki and Ishii observed that for low void fractions, the one-group interfacial area concentration transport equation could be applied within an average deviation of $\pm 9.51\%$. On the other hand, for higher void fractions, one may apply the two-group interfacial area concentration transport equation within an average deviation of $\pm 3.61\%$ for the flow cases studied.

2.5 LOCAL INTERFACIAL AREA MEASUREMENT

Typically, one is interested in the measurement of local interfacial area concentration. However, most of the interfacial area data is an average over a section of pipe and is typically measured via a chemical technique. Thus, researchers are trying to develop a database of local interfacial area measurements so one will be able to improve the modeling of the terms in the interfacial area

transport equation as well as to be able to compare the current one or two group interfacial area transport equations with experimental data. Currently, the most popular method in acquisition of local interfacial area is the multi-sensor conductivity/impedance probe. The multi-sensor probes that are used are usually either double sensor or four sensor probes. The four-sensor probes give better interfacial area measurement results since one does not have to make assumptions on the actual shape of the bubble. However, the four sensor probes are more difficult to construct and since the probe area is relatively large, one experiences many cases in which bubbles miss one or more of the probe tips. This can make data processing very difficult and can lead to inaccuracies in interfacial area measurement. However, this problem is currently being combated with researchers like Kim et al. (Kim et al., 2001) by working on the miniaturization of the four-sensor conductivity probe. By reducing the size of these probes, one will have fewer problems with missing bubbles and be able to get a more accurate measurement of local interfacial area concentration. This reduction in size, however, is not without its drawbacks. By reducing the size of the probe tips, one needs to determine the spacing between the probe tips with greater precision as well as accounting for the fact that some of the probe tips have more area exposed to the surrounding fluid. This increased precision of the probe tip spacing must also be matched with an increased data-sampling rate for good temporal resolution. Revankar and Ishii (Revankar and Ishii, 1993) produced a theoretical foundation for the measurement of the time averaged local interfacial area concentration using a four-sensor conductivity probe. They then used this theoretical formulation to determine interfacial velocity, local interfacial area concentration, and void fraction in a vertical air-water cap bubbly flow. Revankar and Ishii then compared the four-sensor probe results to differential pressure measurements and to theoretical predictions of the interfacial area concentration profiles and found good agreement between theory and measurement.

In addition to the theoretical development of the local volumetric interfacial area transport equation, Morel et al. (Morel et al., 1999) also performed numerical

simulations of simple upward bubble flows and compared the results to their theoretical calculations. They also analyzed numerically the effect that the spacing of the probe tips has on the measurement of interfacial area concentration as well as the vertical velocity component measurement. They found that if the probe spacing were less than 50 times smaller than the bubble diameter, one would achieve excellent measurement of the interfacial area concentration. However, if the spacing of the probe tips is greater than one fifth of the bubble radius, the measurement error for interfacial area concentration will be at least 20%. Morel et al. also found that the error in the vertical velocity component measurement was not sensitively affected by the probe spacing. These numerical results were obtained with the assumption that the bubbles are spherical, monodispersed, with the same radius and velocity. Morel et al. also ran simulations with varying bubble sizes to see the effect of the bubble interfaces missing one or more of the sensors. They found good agreement with the actual value of the interfacial area and the vertical velocity component. However, these results are somewhat artificial since in their simulation, they assumed a uniform distribution in bubble sizes with no lateral velocity components and for real flow cases, bubbles tend to exhibit distributions which are not uniform and do indeed have lateral velocity components.

At the present stage of research in the field of two-phase flow, there is some debate on which type of probe, double sensor or four-sensor, is better for local interfacial area measurement. This will continue until the four sensor probes can be built easily with a small measurement area and with good precision. Until that time many researcher will still rely on the more simplistic and smaller double sensor probe.

3. EXPERIMENTAL SETUP

3.1 EXPERIMENTAL APPARATUS

This set of experiments was carried out in a 50.8 mm diameter vertical air-water test section with a height of 6100 mm ($L/D=120$). A schematic of the test loop is depicted in Figure 3.1.

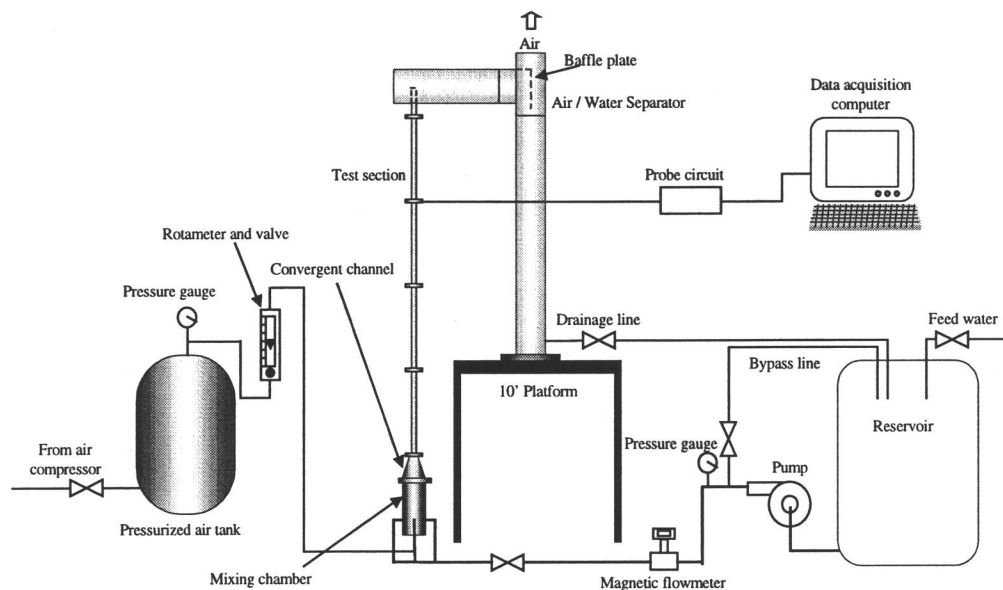


Figure 3.1: Schematic of the test facility

The test section is constructed from clear schedule 40 PVC pipe and is divided into four separate 1525 mm lengths joined together with flanges. Custom made instrumentation mounts have the ability be installed between any of the test section flanges. This allows for flow measurement at L/D equal to 0, 30, 60, 90 and 120 for the investigation into developing conditions for two phase flow. Air is supplied to the facility via an air compressor, which passes through a 4.01 m^3 high-pressure

storage tank that act as a buffer for constant air pressure. The airflow is regulated and measured with the use of a rotameter. Water is supplied to the test facility from a 9.46 m³ storage tank with the use of a pump that is capable of pumping 1.89 m³ per minute at atmospheric pressure. The water flow rate is regulated with a gate valve and is measured with a magnetic flow meter. Air is combined with the water through a section of porous stainless steel with 40 μm pores in the mixing section to produce a nearly uniform distribution of bubble sizes. The two-phase mixture passes through a short conical section in which the diameter reduces from the 15.24 cm mixing chamber diameter to the 50.8 mm test section diameter. The two-phase mixture exits the test section into a horizontal section of 20.32 cm diameter PVC pipe. The air-water mixture then enters a vertical 20.32 cm tee, which is equipped with a stainless steel baffle plate. This separates the air from the water allowing the air to exit out of the top of the tee into the atmosphere and letting the water fall down a 20.32 cm diameter section of PVC pipe which is returned to the storage tank. This 20.32 cm diameter vertical section serves two functions; the first is to act as a drain line and the other is to provide structural support for the air-water separator. This test facility has the ability to easily change the test section diameter in a range of 25.4 mm to 15.24 cm just by replacing the removable conical section and installing the desired diameter of test section pipe.

The design of the air-water injector is shown in Figure 3.2 and Figure 3.3. The injector uses four water inlets and one air inlet. The air enters up the 50.8 mm diameter vertical pipe in the center of the injector. The air is then forced out of the pipe and into the liquid through the porous stainless steel. This creates a uniform distribution of initial bubble size. Out of the four water inlets, three of them are used to control the overall liquid flow rate, while the fourth inlet controls the initial bubble size. The bubble size control works by controlling the flow of water that enters the lower chamber. The water from the lower chamber exits into the upper chamber and passes over the porous stainless steel. By varying this flow rate, one controls the shear force between the bubble and the liquid, thereby altering the size of which the bubble detaches from the porous element. The three other water inlets,

denoted by $Q_{\text{liquid1}} - Q_{\text{liquid3}}$ in Figure 3.2 do not pass over the porous element and thereby do not affect the initial bubble size. These inlets only contribute to the overall liquid flow rate. Using three water inlets to vary the overall liquid flow rate was chosen in order to give a more even circumferential liquid velocity profile in the injector over using one or two water inlets. Water is supplied to the injector through a 76.2 mm diameter pipe that is then split into three 38.1 mm diameter sections that are fed into the overall liquid flow rate control inlets. A separate 38.1 mm diameter pipe with a valve and flow meter is used to control the initial bubble size.

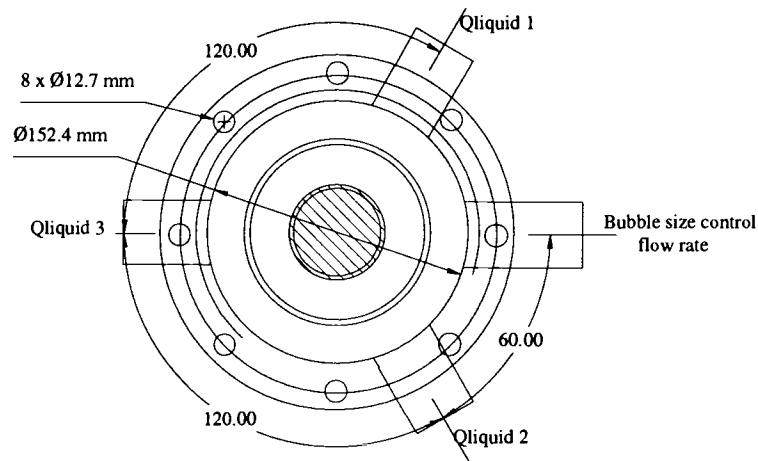


Figure 3.2: Air-water injector top view

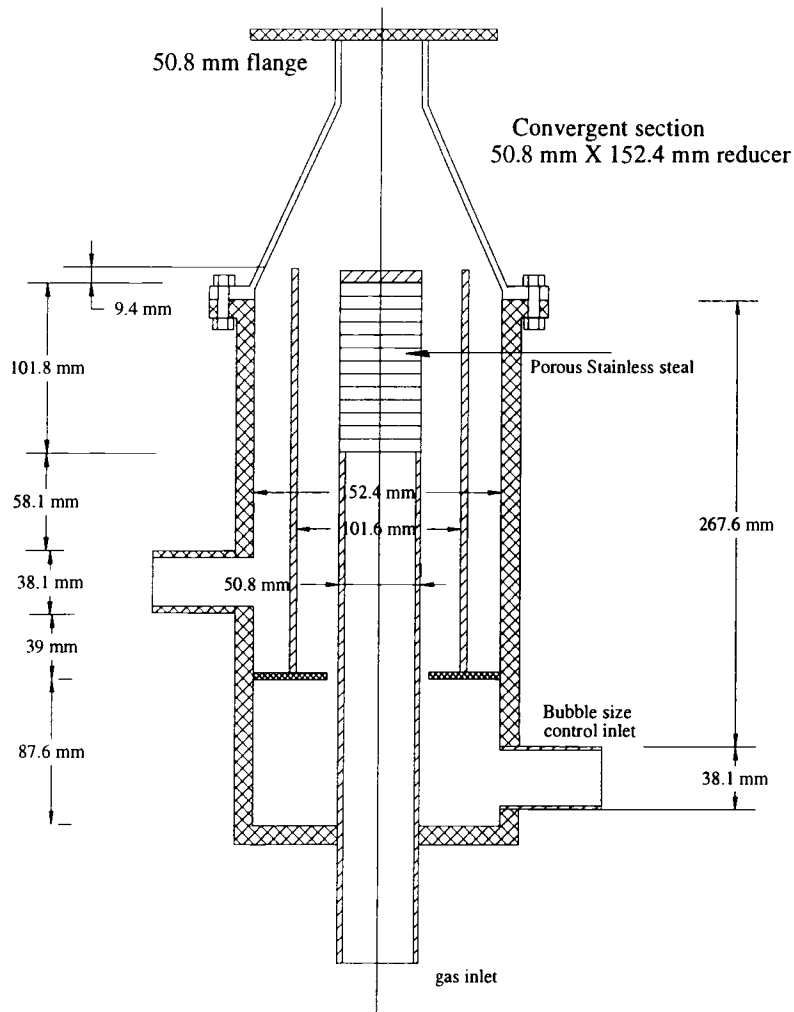


Figure 3.3: Air-water injector side view

The air-water separator baffle plate is shown in Figure 3.4. This baffle plate is constructed from stainless steel and is inserted in the top vertical section of the tee in the air-water separator. The baffle is equipped with three tabs to allow for mounting within the tee. This plate sits in front of the incoming flow from the horizontal portion of the air-water separator thereby forcing the air down the front face of the baffle plate and then forcing the air to turn 180 degrees and flow upward on the back face of the baffle plate. The water droplet in the air cannot make this

turn and therefore fall out of the air and into the liquid drain section of the separator.

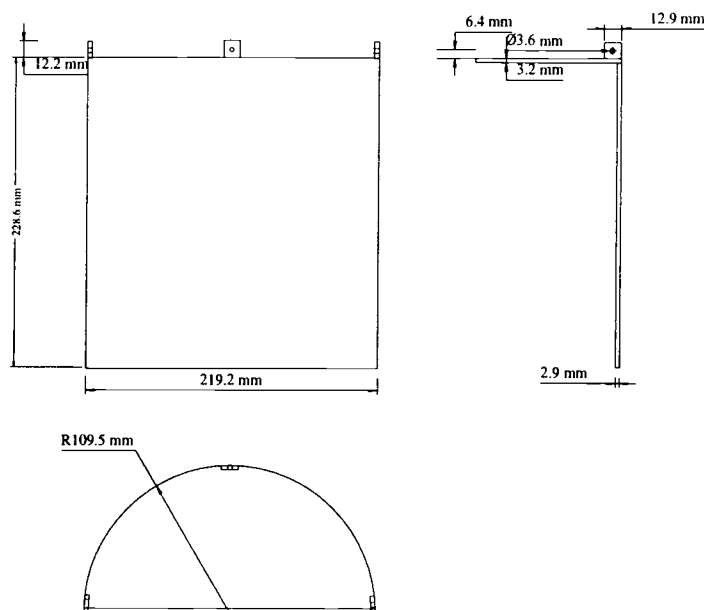


Figure 3.4: Air-water separator baffle plate

The instrumentation mount design is shown in Figure 3.5. The mount is machined out of gray PVC and can be mounted between a set of 50.8 mm flanges. On the side of the instrumentation mount, there are two 1/8" NPT threads where Swagelok fittings are installed. The impedance probe is inserted through one of these fitting and the other is either capped off or could be used to install a pressure tap. This mount design could be easily modified in the future by installing a groove along the inner circumference of the mount to transform the mount into a flush mounted ring type impedance probe. Initially five of these instrumentation mounts were constructed and were installed between each section in the test loop. The mounts are easily removable and can be installed at any location between a set of flanges. Thus, one could have different probes setups in each one of these mounts and easily swap them depending on the experiment of interest and the data required.

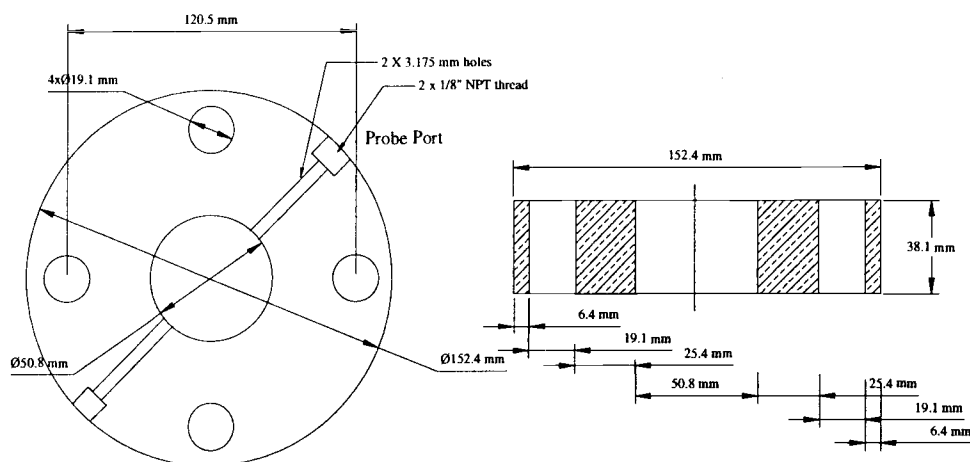


Figure 3.5: Instrumentation mount design

3.2 INSTRUMENTATION

The primary piece of instrumentation for this test facility is the double needle impedance probe. This probe allows for measurement of void fraction, bubble and liquid lengths, number of bubbles that pass through the probe tips, and individual bubble velocities at a single point. The double-sensor probe was chosen over the four sensor probe because the double-sensor probe is easier to construct, the signal processing is less difficult, and since four sensor probes have a large measurement area, four sensor probes are more likely to miss small bubbles as well as creating a greater deformation of the interface of the bubbles. The impedance probe has the ability to transverse the pipe diameter in the radial direction to allow for measurement of the void fraction distribution at any of the probe locations. Four of these probes were constructed along with the required circuitry to measure the two-phase flow parameters of interest at four different axial locations. The probes were inserted at $L/D=6, 30, 60,$ and 90 locations. No probe was inserted at the $L/D=120$

location due to the difficulty in achieving access to the probe as well as that fact that a probe is not needed typically in that location because the flow is already developed at the $L/D=90$ probe location. In addition, the $L/D=120$ location is near the exit of the column; one may find the flow to be affected by the exit condition. Although each probe has the ability to traverse the pipe in the radial direction, only the centerline location was used for this research. In the future, various radial locations as well as additional flow rates will be analyzed as the theoretical part of the research becomes more developed. More about the construction and operation of the probe is described in sections 3.2.1 and 3.2.2.

3.2.1 Impedance probe principles of measurement

The lengths and the velocities of the gas and liquid phases of this experiment are found using a double sensor impedance probe. The probe allows for finding the number of bubbles which passed through the sensor, the amount of time either gas or liquid phases are present, and the velocity of the each phase. The velocity of each phase can be determined by using the difference between the time in which the first sensor detected the phase and when the second sensor detected the phase and using the knowledge of the spacing between the probe tips. This also allows for calculation of each liquid or gas length by multiplying the time of which the particular phase is present on the sensor with the corresponding velocity. If one denotes the spacing between the probe tips as Δs and by knowing that the time it takes the bubble to traverse the distance between the tips, Δt , one can determine bubble velocity.

$$v_{sz} = \frac{\Delta s}{\Delta t} \quad (3.1)$$

By also knowing the time, τ , that the bubble is present at one of the probe tips, the length of the bubble can also be determined by equation (3.2). The same methodology may also be applied to the liquid phase in order to get liquid time and liquid length.

$$\ell_{\text{bubble}} = v_{sz} \tau \quad (3.2)$$

However, not all of the bubbles pass through the probe tips in the manner that will allow for proper measurement as shown in Figure 3.6. The bubble can contact one probe tip but not the other or the bubble can also contact both probe tips at the same time. Either of these cases do not allow for measurement of the bubble velocity and therefore the bubble length. These cases must be eliminated and the number of missed bubbles recorded. This can be done in post-processing with a computer code or while recording data. If the leading sensor detects a bubble, many programs use some maximum waiting time for the trailing sensor to go high based on the lowest bubble velocity one would expect with the current flow conditions. If the trailing sensor does not detect a bubble within this period, it is determined that the bubble is missing. A similar technique may be applied to a minimum waiting time based on the maximum velocity one would expect with their current flow rates. This can be used to eliminate the cases in which the bubble contacts both probe tips at close to the same time. However, in the case in which the bubble's velocity cannot be determined, the time that the bubble is in contact with one of the probe tips is still known and therefore should be included in the calculation of void fraction.

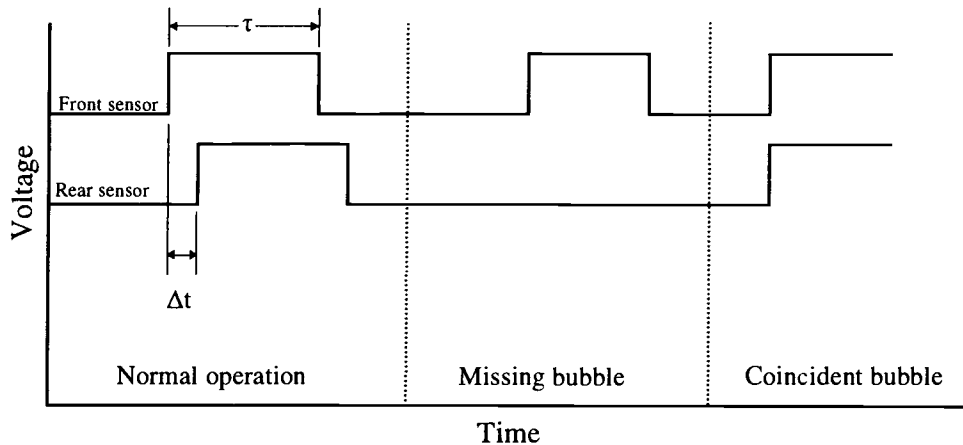


Figure 3.6: Some of the possible double-sensor probes signals

The time-averaged void fraction, $\bar{\alpha}$, was calculated by taking the accumulated time that the sensor was exposed to the gas phase divided by the total sampling time of the sensor. This results in a value that is between 0 and 1. The void fraction is determined by:

$$\bar{\alpha}' = \sum_{i=1}^n \frac{\tau_i}{T} \quad (3.3)$$

where T is the total sampling time and n is the total number of bubbles that pass through one of the probe tips. Although, one could theoretically use either one of the probe tips to determine void fraction, it is more accurate to use the first probe tip to determine void fraction since the first probe tip can influence the bubbles that contact the second probe tip. The probe can detect gas and liquid phases in the vertical column by detecting the change in impedance between the two phases. The probe behaves as a capacitor in parallel with a resistor with the corresponding impedance:

$$Z_{\text{phase}} = (R_{\text{phase}}^{-1} + j\omega C_{\text{phase}})^{-1} \quad (3.4)$$

Where Z is the impedance of the corresponding phase, R is the resistance of that phase, C is the capacitance of the corresponding gas or liquid phase, and ω is the angular driving frequency or $2\pi f$. At higher frequencies, the capacitance term dominates making the probe essentially capacitive. Operating the probe at higher frequencies offers several advantages. Since the resistance term can vary substantially with temperature variations and ion concentrations in the water, the impedance of a given phase can fluctuate greatly for a probe that operates at low frequencies or DC. In addition, probes that operate at or close to dc tend to be slow due to the ion migration time. At higher frequencies where the capacitive term is dominant; the impedance of a given phase is only a function of the electrode area, electrode spacing and the dielectric constant of the liquid or gas. This results in a more stable and faster probe design.

3.2.2 Impedance probe design

The body of the probe is constructed from 11-gauge thin-walled stainless steel tubing and acts as a common electrode for each of the two needles. The probe consists of two stainless steel acupuncture needles that are 120 μm in diameter with an axial spacing of approximately 3 mm. Each needle is placed into a piece of 1 cm long 27-gauge stainless steel tubing and is crimped for good electrical contact. In the other end of the 27-gauge tubing, a 30 cm length of 0.127 mm diameter, Teflon insulated, thermocouple wire is connected. The probe needles are insulated from each other and the probe body with the use of epoxy resin and placed in a 5 cm length of 14-gauge stainless steel tubing. The 11-gauge probe body is cut almost completely through approximately 1 cm from one end. The 11-gauge body is inserted into the probe mount and the notched portion is bent to a 90-degree angle.

The needle assembly is then inserted into the 11-gauge body, the probe wires are ran through the 11-gauge body, and the needle assembly is attached to the 11-gauge probe body with epoxy resin. In addition, the 90-degree bend where the notch was made is also filled with waterproof epoxy. A diagram of the resulting double sensor impedance probe is shown in Figure 3.7.

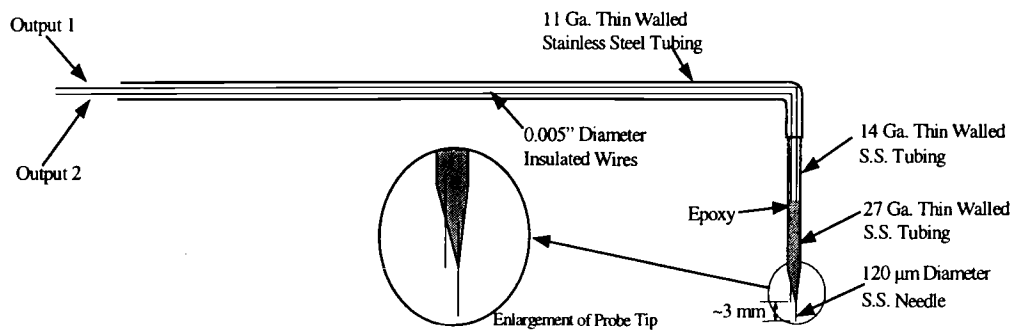


Figure 3.7: Needle probe design

The probe body is connected to the driver circuit and the current through each needle is measured, converted to a voltage, then processed to give an output voltage of 5 volts when gas is present and 0 volts when liquid is present. The designed circuit to complete this task is given in Figure 3.8.

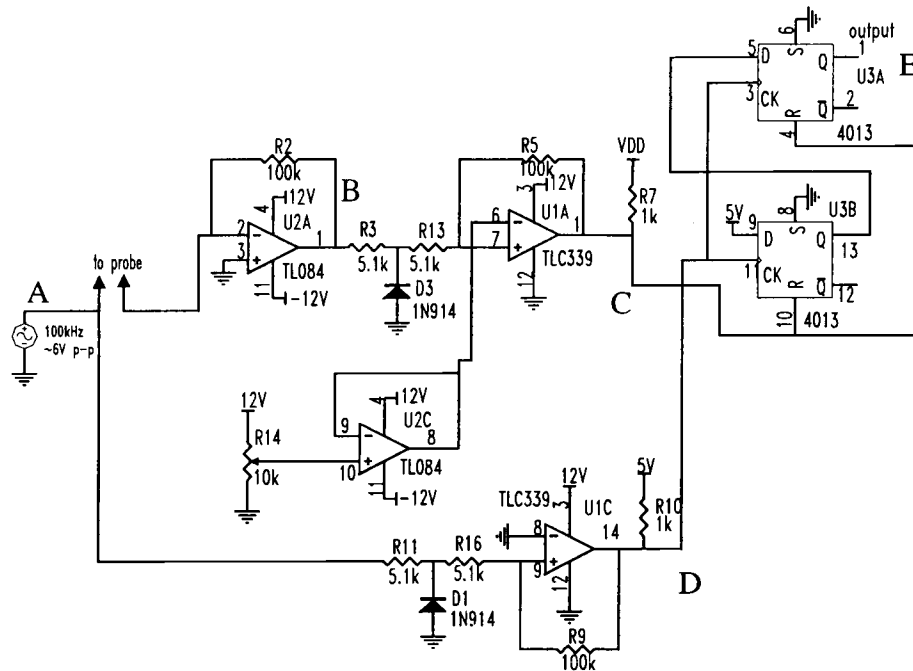


Figure 3.8: Impedance probe signal processing circuit for one probe tip

3.2.3 Signal processing

The driving signal or carrier frequency of 100 kHz with a 6-volt peak-to-peak amplitude sine wave was created using a function generator. This driving signal passes through each of the two probe tips producing a current into U2A. U2A is configured as a current to voltage converter with an output voltage of $0.1 \text{ volts}/\mu\text{A}$. This signal is in turn feed into U1A, which determines if the input signal is greater than the output from U2C. U1A will produce an output voltage of 5 volts if the input is greater than the output from U2C or will produce an output of zero volts if the input is less than the output from U2C. The comparator (U1A) is used to

remove the alternating signal when air is present as well as to convert the 100 kHz sine wave to a 100 kHz square wave. U2C is configured as a voltage follower with the output voltage determined by the variable resistor, R14. By adjusting R14, one can set the threshold voltage that determines whether vapor or liquid is present at the probe tip. U3A and U3B is a pair of D-type flip-flops. The flip-flops are configured so that the output will go high only when the input to the flip-flops is low for a period greater than two cycles of the 100 kHz clock. This means that the output will go high when gas is present and will be low when liquid is present. An example of the voltages at each of the labeled nodes, A through E, is given in Figure 3.9.

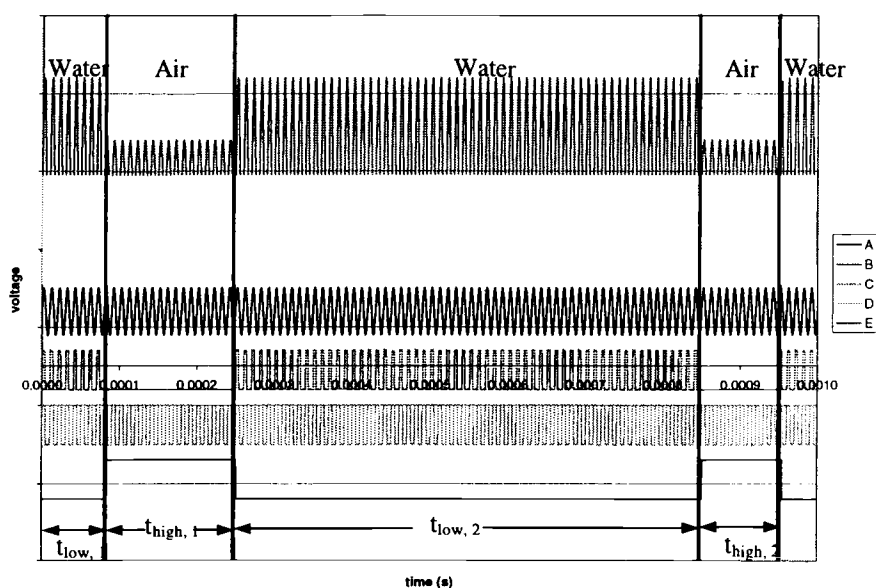


Figure 3.9: Impedance probe timing diagram

3.2.4 Data acquisition

Data is collected using National Instruments' PCI-6023E data acquisition card. This data acquisition card offers 200,000 samples per second sampling rate, 12-bit resolution, and two general-purpose 24-bit counter/timers. The card has the capability of using 16 single ended analog inputs or 8 differential analog inputs. The data acquisition is controlled using National Instruments LabVIEW software. The instrumentation is interfaced with the data acquisition card using National Instruments SCB-68 shielded 68-pin, shielded screw terminal block. A LabVIEW program was written to collect the analog input voltages in a buffered manner then write the voltages to a tab delimited text file. The software also allows for plotting the data on screen at near real-time rates. For each of the double sensor impedance probes, two analog inputs were required, one for each tip. The signal from the rear sensor of one of the impedance probe was also connected to one of the data acquisition card's onboard counters to allow for counting of the number of bubbles that pass through the probe tips. One may input the desired number of bubble that pass through the probe tips to be acquired or the total time to sample data for and the data acquisition will cease once that number of bubbles or time is reached. The voltages from the output of the impedance probe circuit were scanned at a rate of 10,000 samples per second to ensure an accurate measurement of the bubble velocities and lengths. At this scan rate however, the output files can become quite large and cannot be opened by most spreadsheet programs. This requires the development of a code that will read in the scanned voltages and convert this information into the values for the widths of each individual pulse of interest. The post processing method is discussed further in section 3.2.5.

3.2.5 Post processing

After the data is collected, the data file is passed into a program written in C++ that converts the scanned voltages into a pulse width measurement for velocities and for the time that each gas or liquid phase is present. The program outputs three columns for each probe. One column for times which gas is present, one for time which liquid is present, and the final column for the time it took for each bubble to travel from the first probe tip to the second. This allows for easy calculation of liquid or gas lengths, times, and velocities because the scan rate and the distance between the probe tips is known. Since a bubble can hit both tips at the same time or hit one tip but miss the other, one needs a way of eliminating either of these cases since the bubble length or velocity cannot be determined in these cases. This program also eliminates the cases in which velocities and lengths cannot be found and produces an output file in which only the valid measurements are displayed. However, since one only needs the time in which gas is present on one of the tips and the total time in which data was collected to determine the time averaged void fraction, one includes all of the bubble measurements, even the cases in which velocity cannot be determined, to determine the void fraction. However, since all bubble measurements and the valid bubble measurements are both required for further calculations, the C++ program outputs two tab delimited text files; one that includes all gas and liquid times, and the other with only valid gas and liquid times and velocities. These output files can then be imported into Microsoft Excel to create histogram of the various quantities of interest. For fitting of the distribution, BestFit 4.5 by Palisade Software was used. BestFit is a commercial program that attempts to fit up to twenty-seven different distribution functions to your data. Best Fit then ranks the distributions based on some goodness of fit test. BestFit provides the values to the necessary parameters of the distribution as well as plotting the fitted curve against the actual data. BestFit is also useful for determining statistical parameters of the input data like mean, median, or standard deviation.

4. DATA AND RESULTS

Table 4.1 provides a tabulated list of the different test cases that were performed. There were six cases performed using two different liquid flow rates and three different gas flow rates. Data was then collected at the four measurement locations, $L/D=6, 30, 60,$ and 90 , to analyze the development of two-phase flow in a vertical column. With this set of test cases, bubbly flow, slug flow, and transition from bubbly flow to slug flow were all observed.

Table 4.1: Test matrix

Test Number	Liquid Flow Rate Q_l (gal/min)	Gas Flow Rate Q_g (SCFH)	Superficial Liquid Velocity j_l (m/s)	Superficial Gas Velocity j_g (m/s)
TC-1	30	40	0.93	0.25
TC-2	20	40	0.62	0.25
TC-3	30	60	0.93	0.37
TC-4	20	60	0.62	0.37
TC-5	30	80	0.93	0.49
TC-6	20	80	0.62	0.49

Table 4.2 lists the time averaged pipe centerline void fraction for each test case and for each axial measurement station. The void fraction was determined using equation 3.3 using the signal from the leading sensor of the double sensor conductivity probe. This signal includes both the normal measurement case and the missing bubble case since a velocity measurement is not required for the determination of void fraction. One will note from Table 4.2, an increasing trend in the void fraction as the gas flow is increased. One can also observe that the void fraction decreases with increasing liquid flow rate. From Table 4.2, one will also note an increasing trend in void fraction as one progress from lower axial locations to higher axial locations. This is to be expected since the reduction in surrounding

pressure as the bubble rises allows for expansion of the bubble and thus an increase in void fraction. Another mechanism for the increase in void fraction in the centerline of the pipe is a change in the radial void fraction distribution. Typically, near the entrance of the column, the radial void fraction distribution is saddle shaped with higher void fractions being near the pipe wall. However, as the flow develops, the bubbles will move toward the center of the pipe and form a parabolic void fraction distribution in the radial direction. In the case of the parabolic distribution, the void fraction will be higher in the center of the pipe and reduce to zero at the pipe wall. Because of this change in the void fraction radial profile, one could get an increase in the pipe centerline void fraction along the axial direction even without the change in surrounding pressure due to gravity. In addition to displaying void fraction data, Table 4.2 also shows the flow regimes observed by using different shades of gray. The lightest gray is the bubbly flow regime, the medium gray is the transition from bubbly flow into slug flow, and the darkest gray is the slug flow regime. However, flow regime identification is somewhat subjective in that what one person thinks is transition from bubbly to slug flow regime, another person may think it is the slug flow regime or maybe even the bubbly flow regime. Table 4.2 will however give an idea of how a certain void fraction at a certain stage of development appears visually.

Table 4.2: Void fraction data

	Bubbly		Transition		Slug	
	TC-1	TC-2	TC-3	TC-4	TC-5	TC-6
L/D=90	0.089	0.155	0.175	0.333	0.336	0.384
L/D=60	0.085	0.180	0.195	0.380	0.353	0.432
L/D=30	0.015	0.112	0.053	0.086	0.056	0.118
L/D=6	0.051	0.056	0.047	0.080	0.092	0.191

One will notice however, that the measured void fraction at $L/D=60$ location generally reads higher than the void fraction at $L/D=90$ location. This is somewhat unexpected since the void fraction typically increases as the bubbles rise up the column. By looking at the data, the only explanation for this fact is either error associated with the probe or that the centerline void fraction at $L/D=90$ is truly less than the void fraction at $L/D=60$. If the centerline void fraction at $L/D=90$ is truly lower, some of the reasons may be that the probe at $L/D=60$ is enhancing breakup of the larger bubbles as well as potentially causing a change in the void fraction radial distribution. If this is the case, further breakup of the large bubbles will create a lower void fraction measured at the next measurement station. One will notice from the table that the axial variation in the void fraction is correct in test TC-1 all the way to the top of the pipe. This means that the discrepancy may not be a result of error in the probe since the $L/D=60$ did not consistently read higher. In case TC-1, bubbly flow existed along the entire length of the pipe which reinforces the possibility that the discrepancy in the void fraction measurement between $L/D=60$ and $L/D=90$ locations is due to breakup caused by the probe at the $L/D=60$ measurement location.

After acquiring the data, the data was then processed through a C++ program, which is included as an appendix, developed by the author to allow for conversion between the numerous lines of scanned voltages to pulse width measurements. The pulse width measurements included vapor residence times, the liquid residence time, and the time difference between the leading signal edge of the forward sensor and the leading signal edge of the rear sensor for velocity determination. This processed data directly gives the residence time of each bubble and liquid portion and allows for the calculation of bubble velocity indirectly. This data is then passed into Excel and BestFit 4.5 for further analysis.

The commercially available program, BestFit 4.5, allows for fitting of up to twenty-seven different distributions. However, for the case of this research, only the codes ability to calculate mean values and standard deviations of the data will be used in the analysis.

In the following section, some of the distributions that will be considered in future work for fitting of the data will be described in order to facilitate the understanding of the analysis. Some of the more likely distributions that will be used include the normal distribution, the lognormal distribution, and the gamma distribution.

The normal distribution is a popular symmetric distribution given by the following equation.

$$f(x) = \frac{1}{\sqrt{2\pi}\sigma} e^{-\frac{1}{2}\left(\frac{x-\mu}{\sigma}\right)^2} \quad (4.1)$$

In this equation, μ is the mean value of the distribution and σ is the standard deviation.

The lognormal distribution is based on the normal distribution and is often used in particle size distributions as well as time to failure distributions. The lognormal distribution is asymmetric on a linear scale with a shape leading edge peak followed by a long tail. One of the advantageous qualities of the lognormal distribution is that it cannot report negative quantities. This is one of the reasons why this distribution is useful for such things as particle size in which a negative value does not make sense. The lognormal distribution is given by:

$$f(x) = \frac{1}{x\sqrt{2\pi}\sigma'} e^{-\frac{1}{2}\left(\frac{\ln x - \mu'}{\sigma'}\right)^2} \quad (4.2)$$

where:

$$\mu' = \ln \left[\frac{\mu^2}{\sqrt{\mu^2 + \sigma^2}} \right] \quad (4.3)$$

and

$$\sigma' = \frac{1}{2} \ln \left[1 + \left(\frac{\sigma}{\mu} \right)^2 \right] \quad (4.4)$$

The third distributions that will be considered is the gamma distribution. The gamma distribution is defined as the following.

$$f(x) = \frac{1}{\beta \Gamma(\alpha)} \left(\frac{x}{\beta} \right)^{\alpha-1} e^{-x/\beta} \quad (4.5)$$

where α is a continuous shape parameter, β is a continuous scale parameter, and Γ is the Gamma Function. The Gamma Function is defined by equation 4.6.

$$\Gamma(z) = \int_0^{\infty} t^{z-1} e^{-t} dt \quad (4.6)$$

4.1 RESIDENT VAPOR TIME

Table 4.3 lists the mean vapor resident time for each axial position as well as for different flow rates. One can definitely see a trend in the data. For a given liquid flow rate, the mean residence time for the vapor phase increases as the gas flow rate is increased. It also increases as a function of axial position. One may also note a large jump in the mean vapor residence time from about 1.5 milliseconds to more than 5 milliseconds. This corresponds to the transition to slug flow. The presence of slug bubbles greatly influences the mean vapor residence time as well as the standard deviation of the vapor residence time.

Table 4.3: Mean resident vapor time (ms)

	TC-1	TC-2	TC-3	TC-4	TC-5	TC-6
L/D=90	2.8	5.0	2.7	8.5	4.9	14.9
L/D=60	2.6	4.0	3.1	5.2	4.8	8.5
L/D=30	0.9	1.3	1.1	1.4	1.1	1.6
L/D=6	1.5	1.7	1.5	2.0	1.8	2.4

Table 4.4 lists the standard deviation of the vapor residence time for the data that was acquired. One may notice that the standard deviation in the data follows a similar trend to the mean vapor residence time. Table 4.4 shows a large jump in the data as slug flow begins to occur.

Table 4.4: Resident vapor time standard deviation (ms)

	TC-1	TC-2	TC-3	TC-4	TC-5	TC-6
L/D=90	1.2	3.1	2.2	11.2	10.2	29.8
L/D=60	0.7	1.9	1.6	5.6	6.8	17.7
L/D=30	0.5	0.9	0.6	0.9	0.7	1.1
L/D=6	0.7	0.8	0.7	0.9	0.9	1.3

The data in Tables 4.3 and 4.4 make sense intuitively. At the entrance to the vertical column, all of the bubbles should be near the same size. However, as the flow travels up the pipe, the bubbles will expand which increases their mean size. In addition, some bubbles will coalesce as they proceed along the direction of flow resulting in some bubble growing faster than others do. This phenomenon will increase the spread in the distribution and therefore the standard deviation. One

would also expect to see a larger mean residence time for the vapor if the gas flow is increased and a decrease in mean residence time if the liquid flow is increased. This can clearly be seen in Table 4.3.

The distributions for the resident vapor times for tests TC-1 through TC-6 is shown in Figures 4.1 – 4.24 with each flow condition beginning with $L/D=90$ and descending to $L/D=6$. One may observe the information from Tables 4.3 and 4.4 from these distribution plots in that one can see how the peak shifts to a higher mean value and becomes shorter and wider as the flow develops along the axial direction. This is intuitive since the expansion will cause a shift in the distribution and coalescence/breakage will increase the standard deviation. One can also note from the distributions of vapor residence time that the shape of the distribution tends to be along the lines of a lognormal distribution or a gamma function distribution. From the distributions of the resident vapor time, one can also observe that the mean residence time increases with increasing gas flow and decreases with increasing liquid flow.

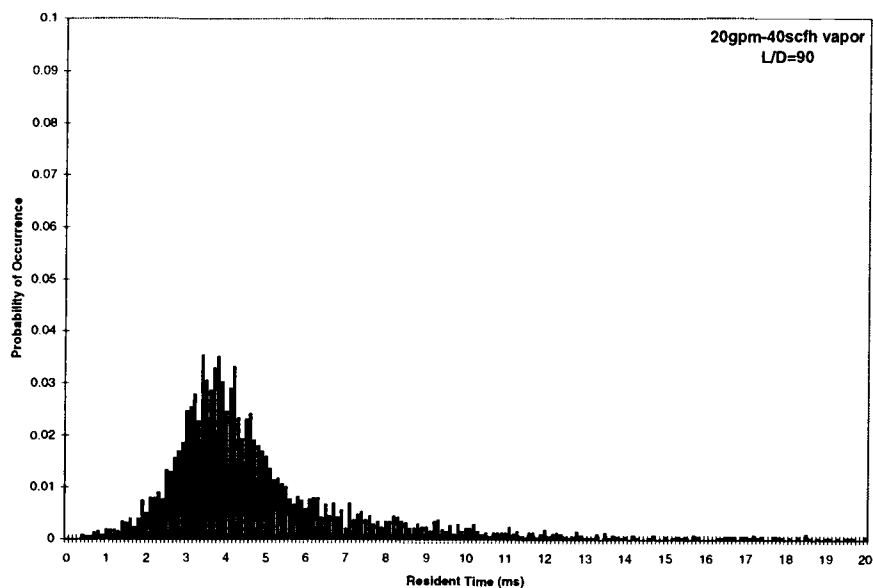


Figure 4.1: Resident vapor time distribution, L/D=90, 20 gpm, 40 scfh

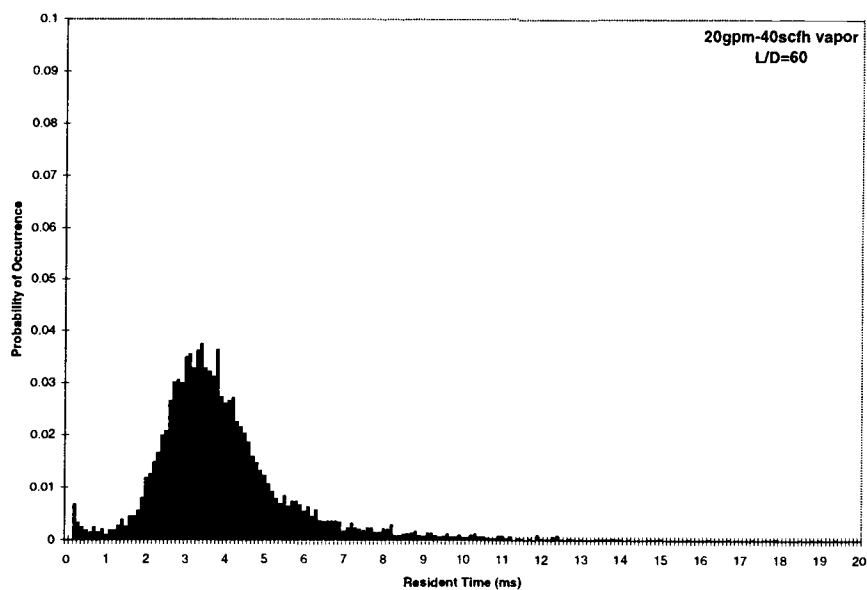


Figure 4.2: Resident vapor time distribution, L/D=60, 20 gpm, 40 scfh

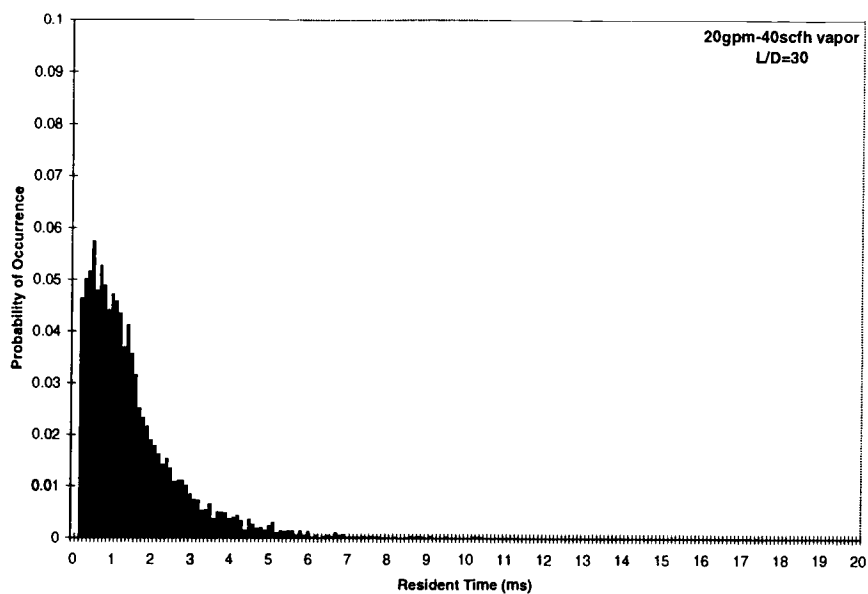


Figure 4.3: Resident vapor time distribution, $L/D=30$, 20 gpm, 40 scfh

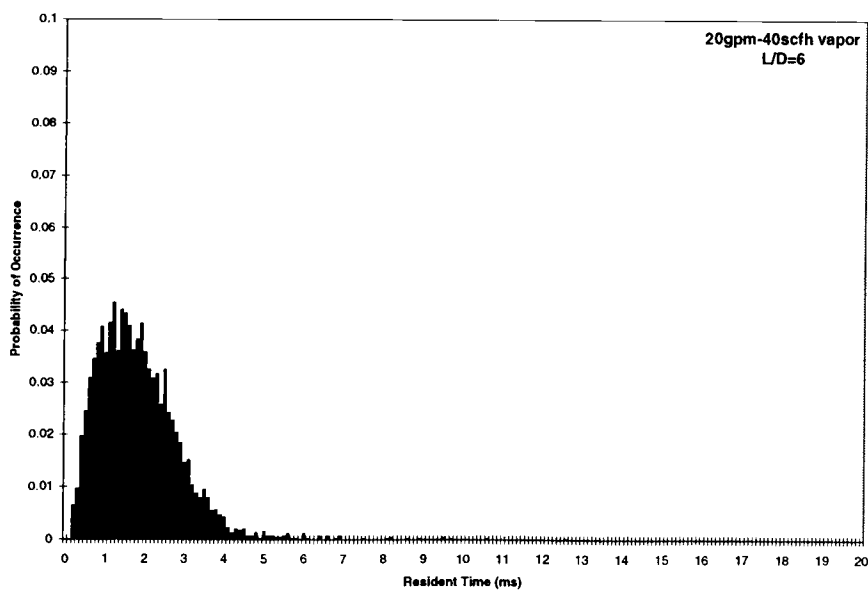


Figure 4.4: Resident vapor time distribution, $L/D=6$, 20 gpm, 40 scfh

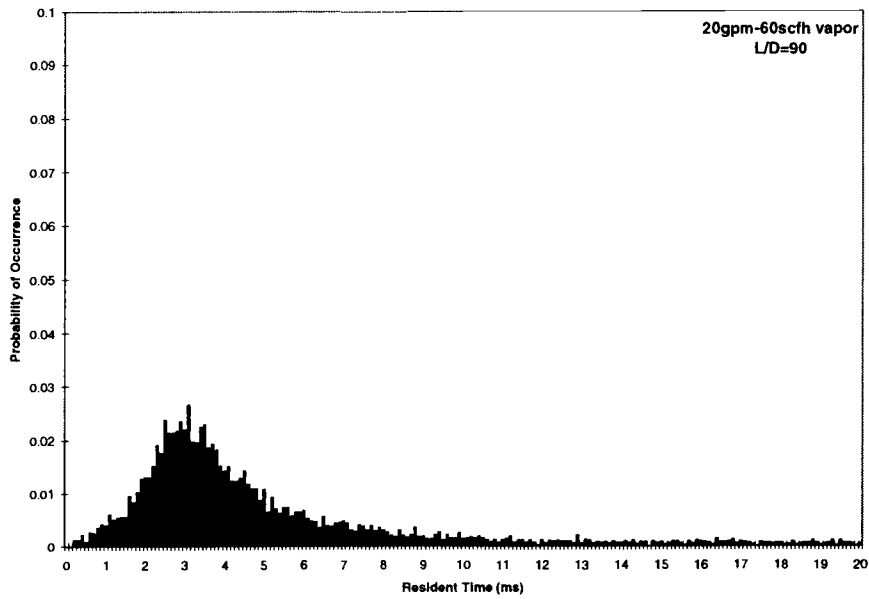


Figure 4.5: Resident vapor time distribution, L/D=90, 20 gpm, 60 scfh

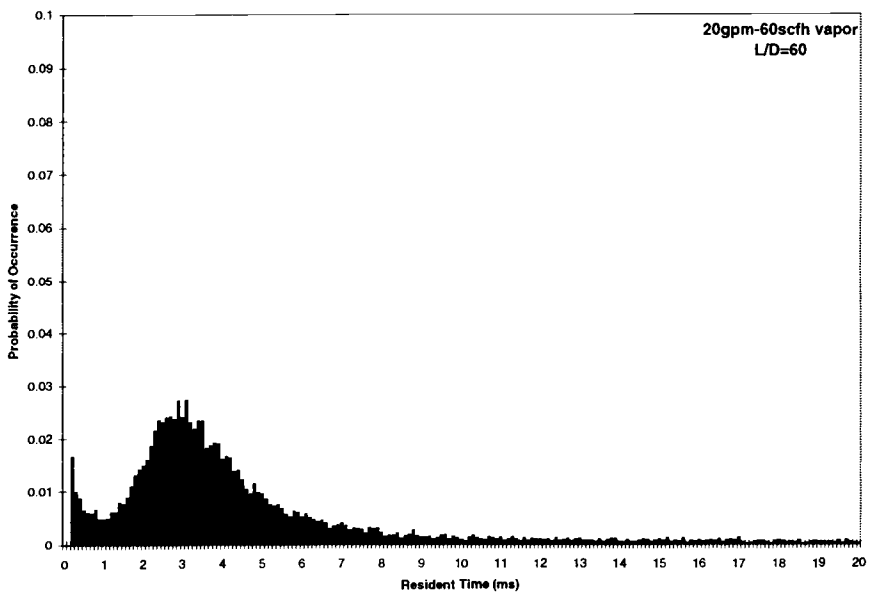


Figure 4.6: Resident vapor time distribution, L/D=60, 20 gpm, 60 scfh

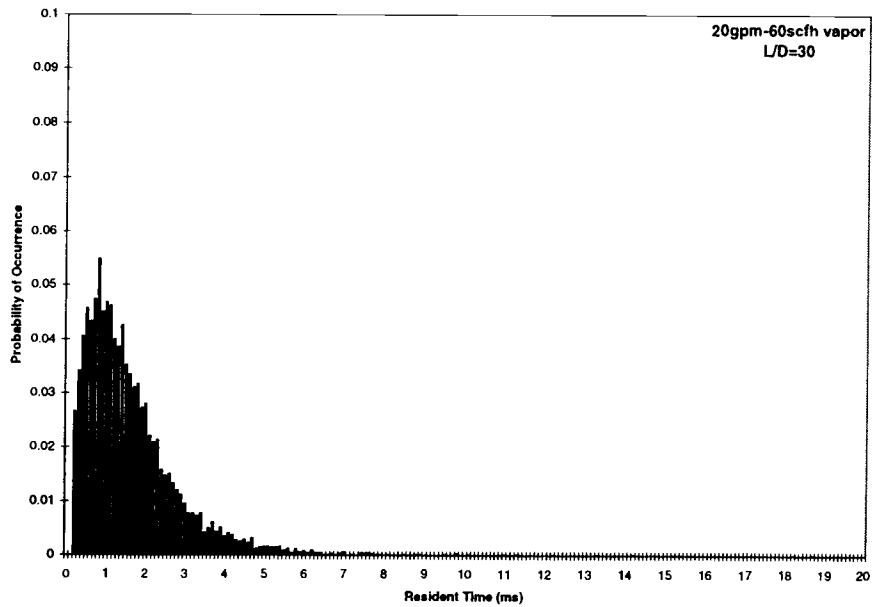


Figure 4.7: Resident vapor time distribution, $L/D=30$, 20 gpm, 60 scfh

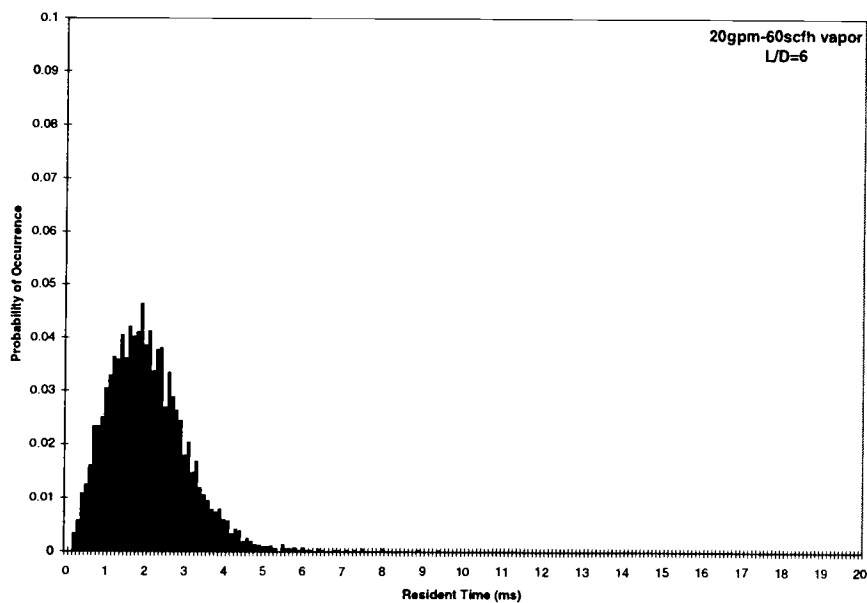


Figure 4.8: Resident vapor time distribution, $L/D=6$, 20 gpm, 60 scfh

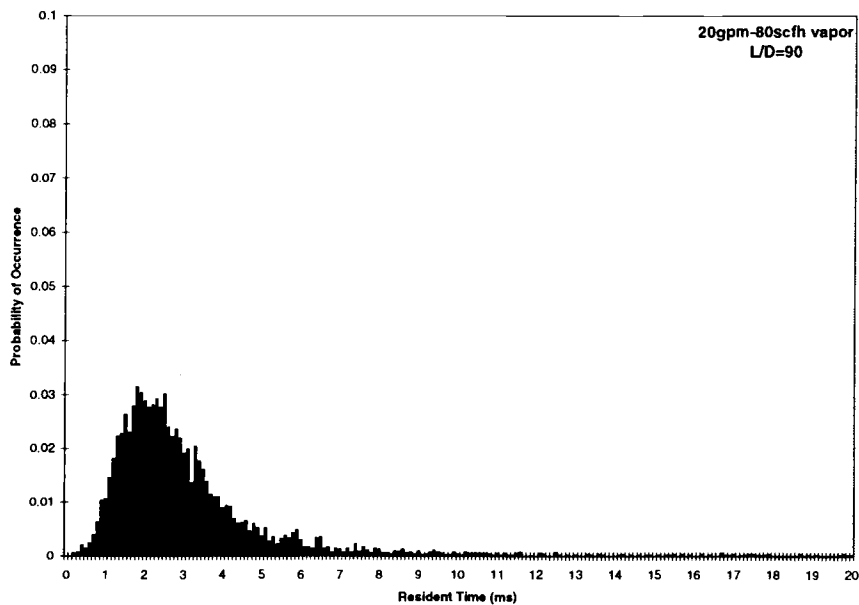


Figure 4.9: Resident vapor time distribution, L/D=90, 20 gpm, 80 scfh

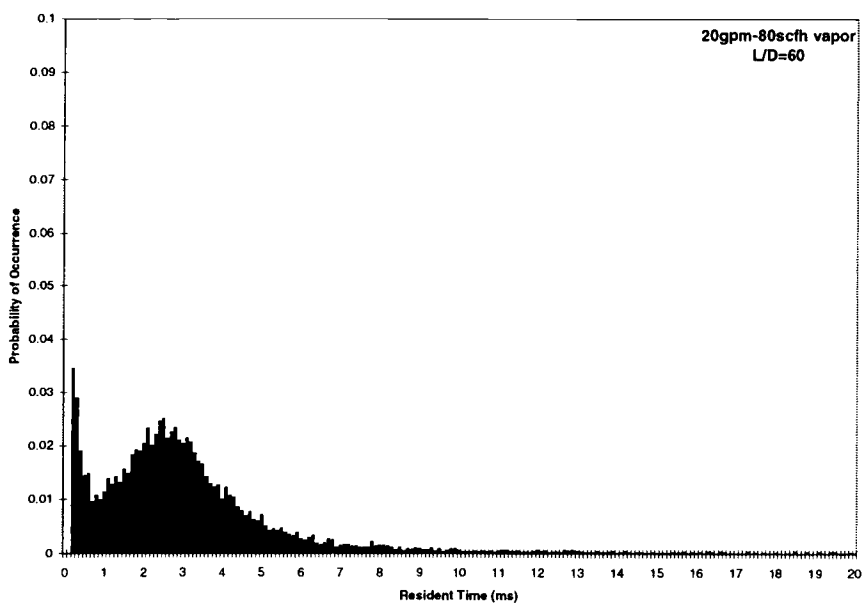


Figure 4.10: Resident vapor time distribution, L/D=60, 20 gpm, 80 scfh

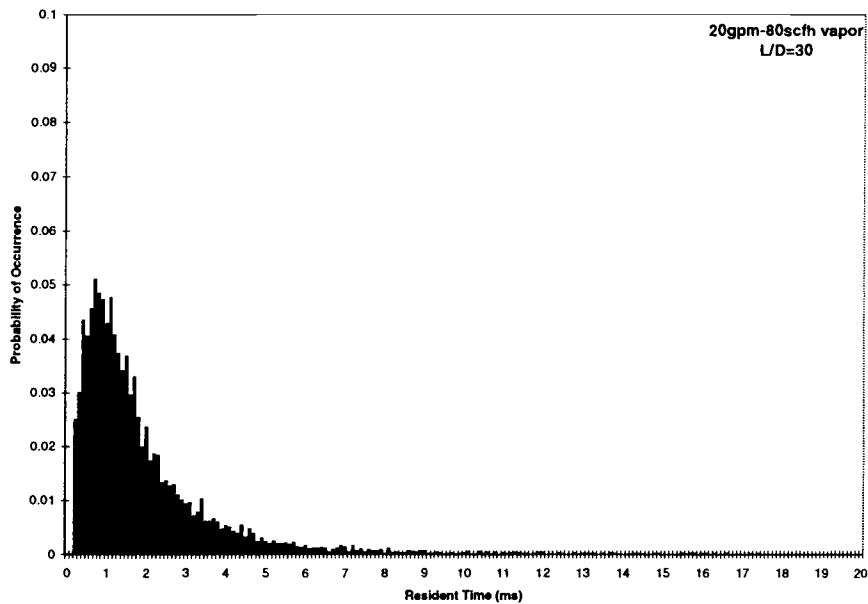


Figure 4.11: Resident vapor time distribution, L/D=30, 20 gpm, 80 scfh

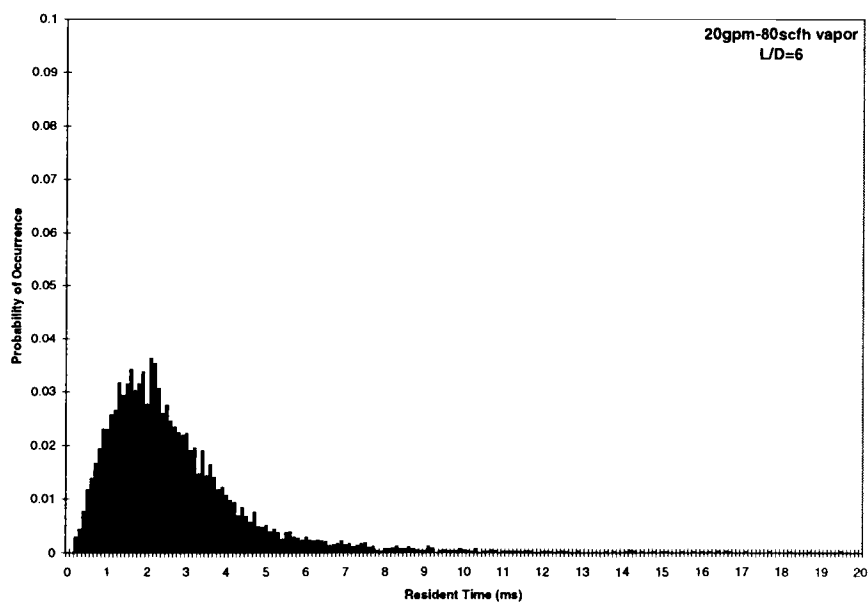


Figure 4.12: Resident vapor time distribution, L/D=6, 20 gpm, 80 scfh

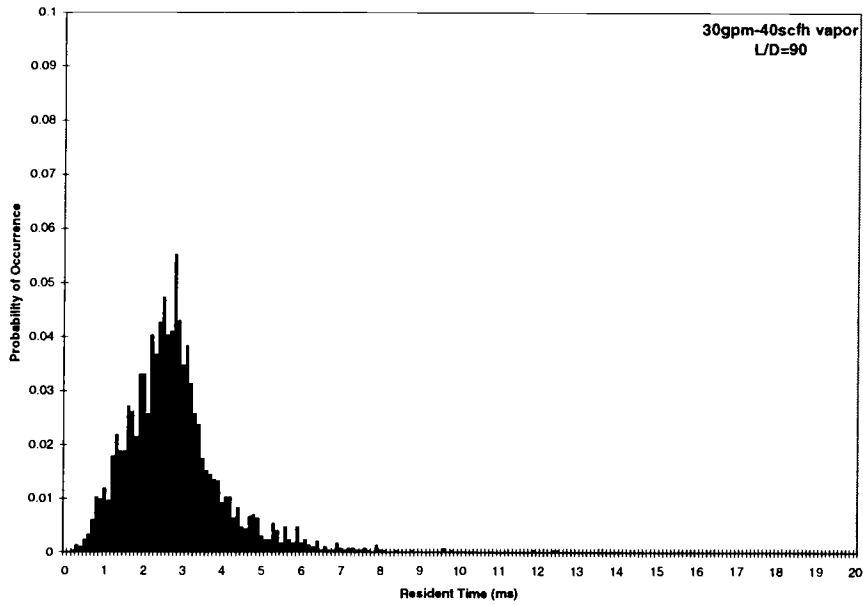


Figure 4.13: Resident vapor time distribution, $L/D=90$, 30 gpm, 40 scfh

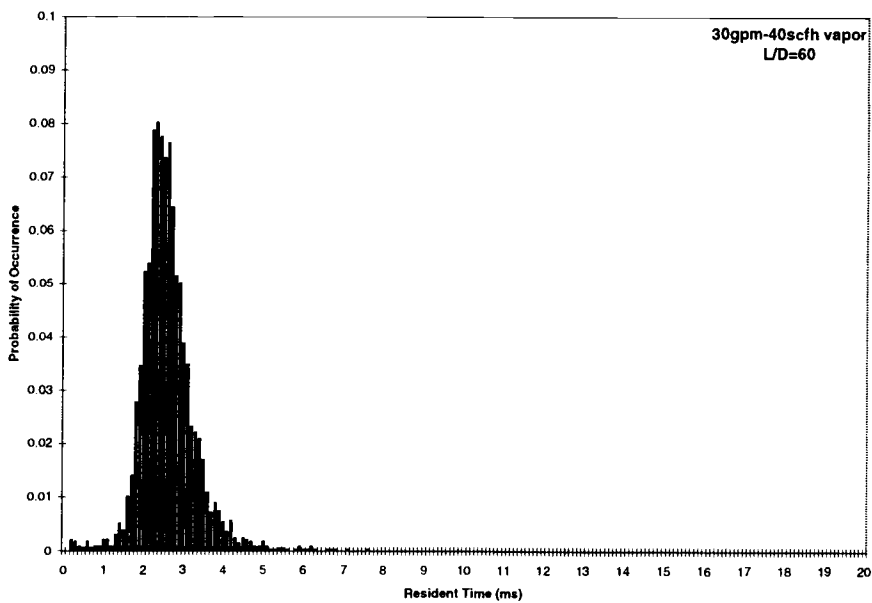


Figure 4.14: Resident vapor time distribution, $L/D=60$, 30 gpm, 40 scfh

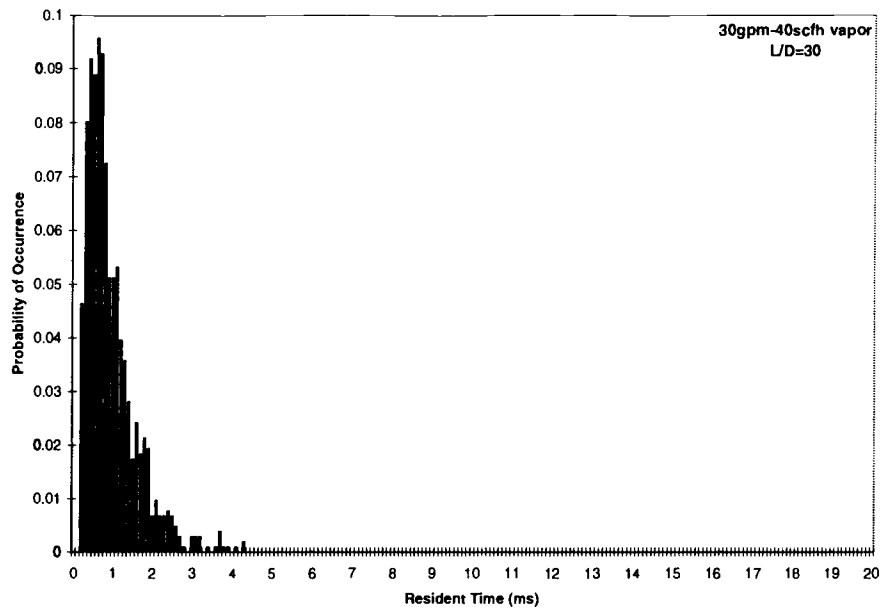


Figure 4.15: Resident vapor time distribution, $L/D=30$, 30 gpm, 40 scfh

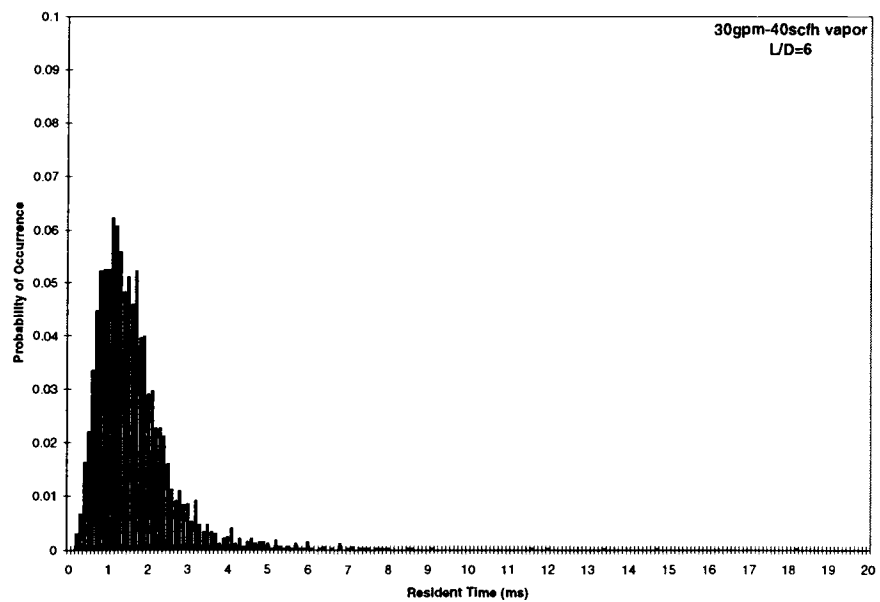


Figure 4.16: Resident vapor time distribution, $L/D=6$, 30 gpm, 40 scfh

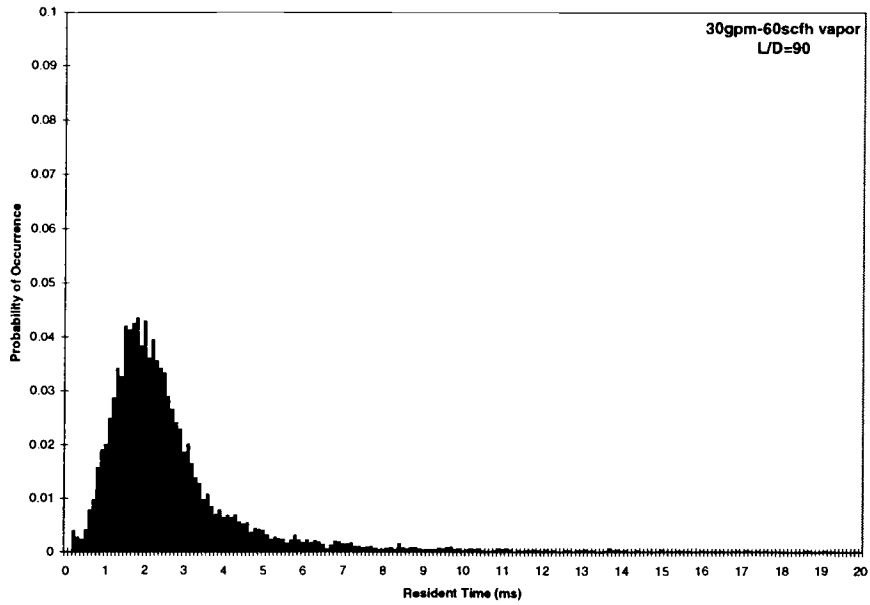


Figure 4.17: Resident vapor time distribution, L/D=90, 30 gpm, 60 scfh

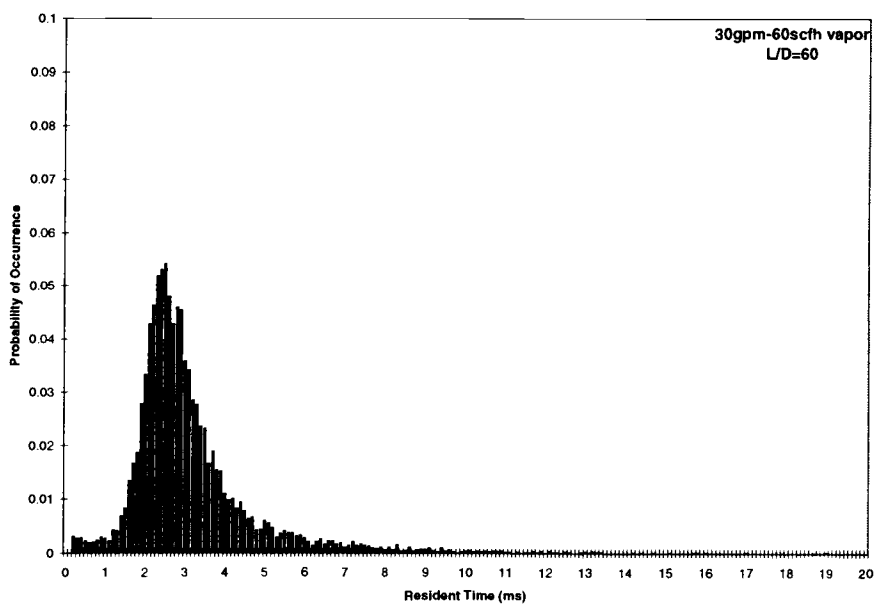


Figure 4.18: Resident vapor time distribution, L/D=60, 30 gpm, 60 scfh

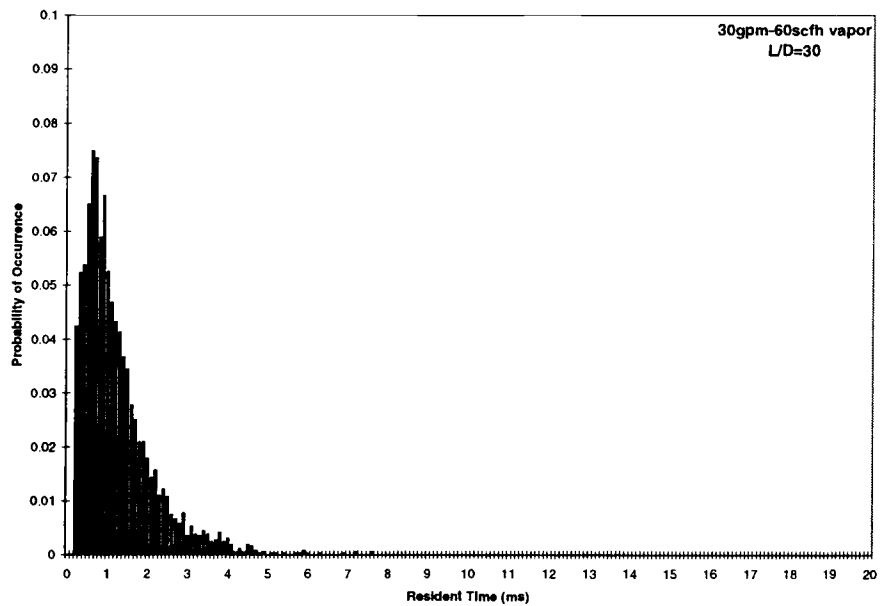


Figure 4.19: Resident vapor time distribution, $L/D=30$, 30 gpm, 60 scfh

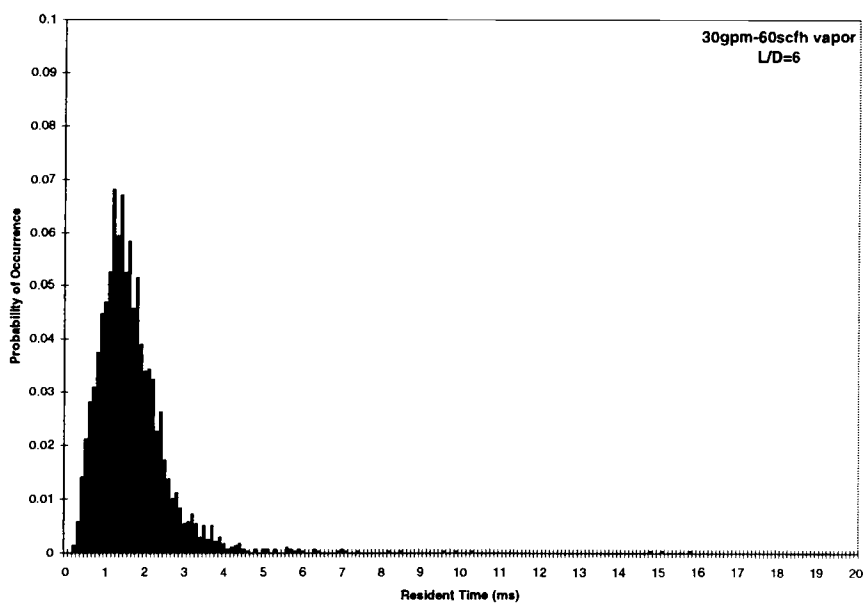


Figure 4.20: Resident vapor time distribution, $L/D=6$, 30 gpm, 60 scfh

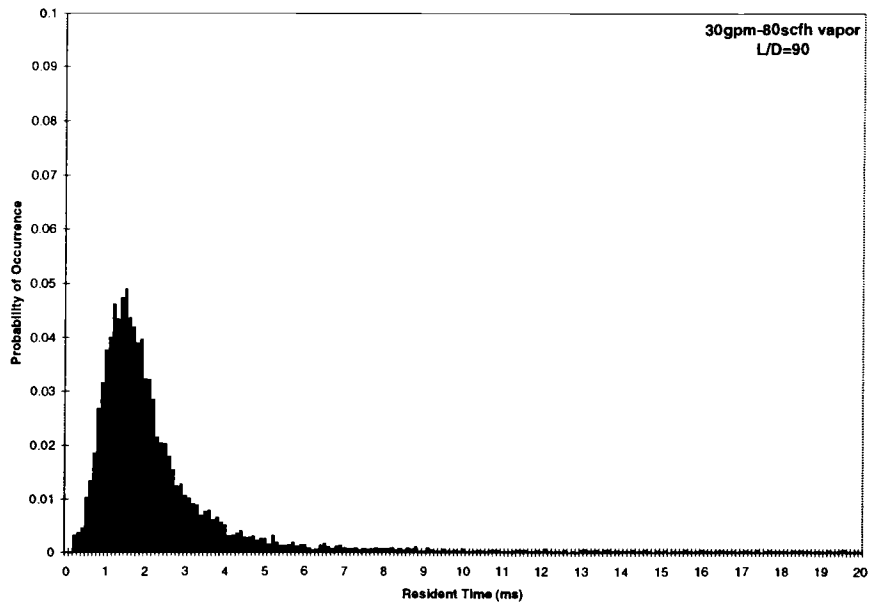


Figure 4.21: Resident vapor time distribution, L/D=90, 30 gpm, 80 scfh

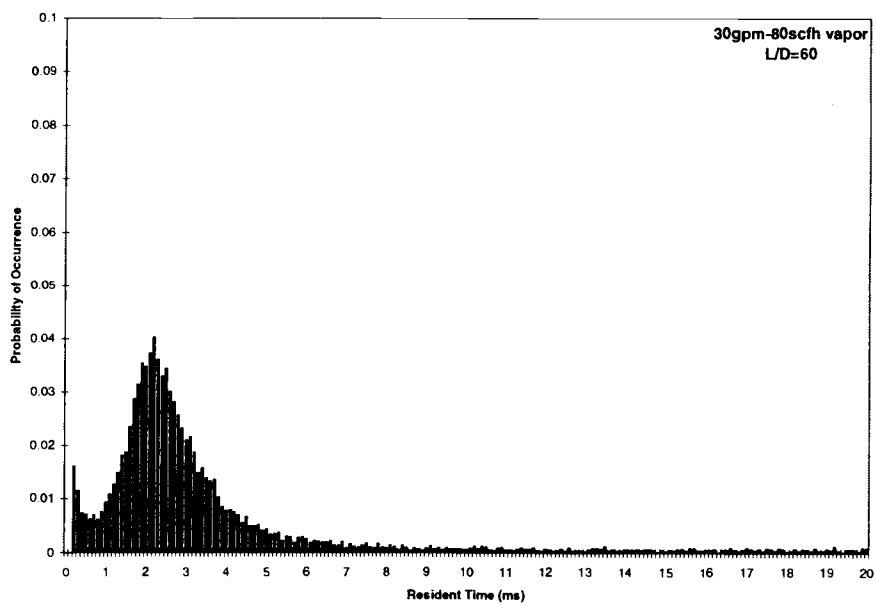


Figure 4.22: Resident vapor time distribution, L/D=60, 30 gpm, 80 scfh

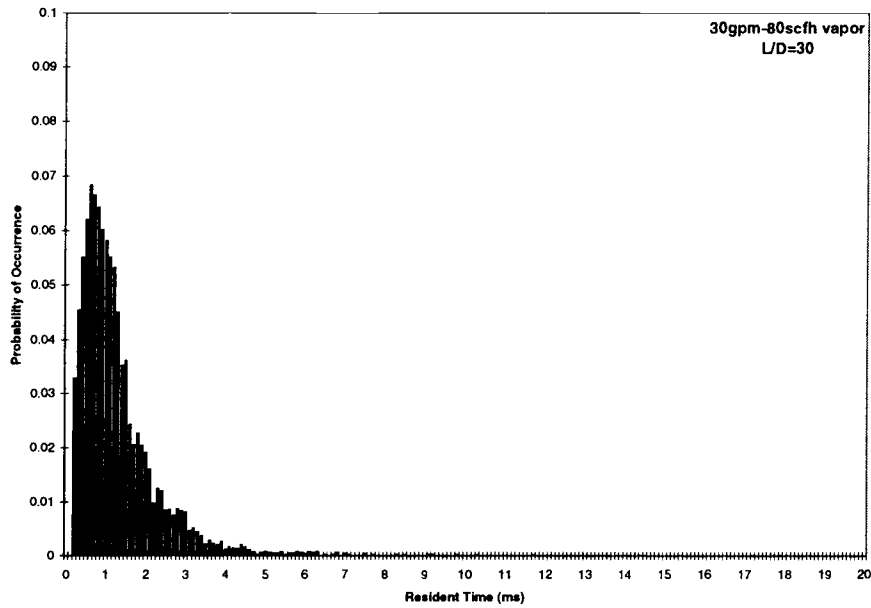


Figure 4.23: Resident vapor time distribution, $L/D=30$, 30 gpm, 80 scfh

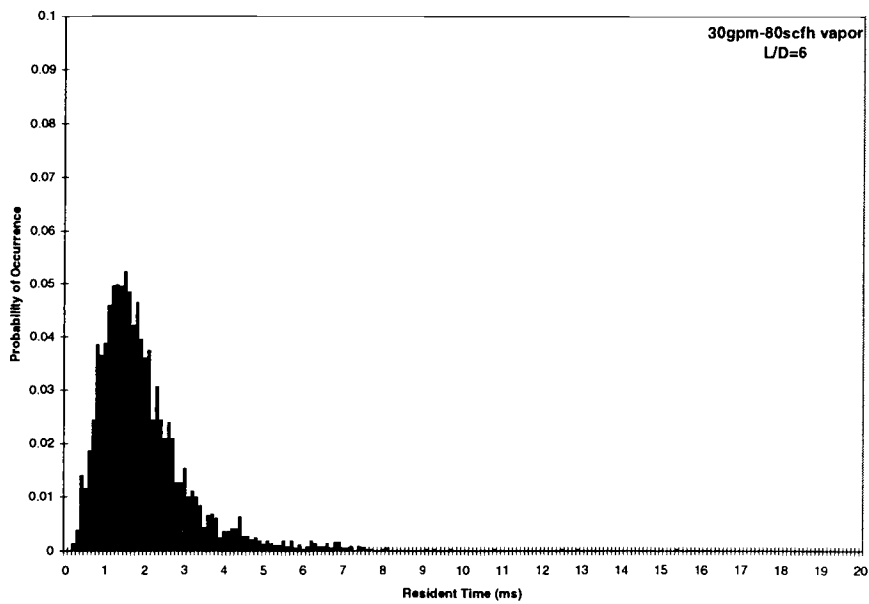


Figure 4.24: Resident vapor time distribution, $L/D=6$, 30 gpm, 80 scfh

4.2 RESIDENT LIQUID TIME

The distributions for the resident liquid times for tests TC-1 through TC-6 is shown in Figures 4.25 – 4.48 with each flow condition beginning with $L/D=90$ and descending to $L/D=6$. These distributions were included since any distribution with the liquid portion of the flow is typically not reported. It is interesting to note that some of the resident liquid time distributions follow an exponential type distribution while others exhibit something like a lognormal or gamma distribution. One can note from the sequence of distributions that, like the vapor resident time distributions, the distribution tends to become less peaked and shifted to higher values as one progresses along the axial direction of flow. One may observe the information from Tables 4.4 and 4.5 from these distribution plots in that one can see how the peak shifts to a higher mean value and becomes shorter and wider as the flow develops along the axial direction. From the distributions of the resident liquid time, one can also observe that the mean residence time increases with increasing liquid flow and decreases with increasing gas flow.

Table 4.5: Mean resident liquid time (ms)

	TC-1	TC-2	TC-3	TC-4	TC-5	TC-6
L/D=90	18.2	16.5	10.0	9.8	7.6	9.6
L/D=60	17.0	11.6	8.0	5.4	5.0	5.0
L/D=30	17.7	4.7	7.5	6.6	7.9	5.4
L/D=6	9.7	13.2	8.3	7.4	4.6	3.4

Table 4.6 lists the standard deviation of the liquid residence time for the data that was acquired. One may notice that the standard deviation in the data follows a similar trend to the mean liquid residence time.

Table 4.6: Resident liquid time standard deviation (ms)

	TC-1	TC-2	TC-3	TC-4	TC-5	TC-6
L/D=90	18.6	16.6	11.3	11.0	8.5	11.0
L/D=60	16.1	11.8	8.2	7.1	6.5	7.8
L/D=30	38.2	9.8	15.0	13.1	16.0	12.8
L/D=6	15.2	18.1	13.3	10.7	4.8	5.7

Tables 4.5 and 4.6 contain some valuable information on the behavior of the liquid phase in two-fluid flow in a vertical column. One can observe trends in the data for the liquid resident times in Tables 4.5 and 4.6. Table 4.5 shows a general increase in the mean liquid resident time as the liquid flow rate is increased and a decrease in the mean resident time as the gas flow is increased. Table 4.5 also shows an increase in liquid resident time as the flow develops along the axial direction. From Table 4.6, it can be noted that standard deviation in the liquid resident time decreases from increasing gas flow. However, based on the data available, it is difficult to clearly state how the standard deviation in the liquid resident time changes in relation to a change in liquid flow rate.

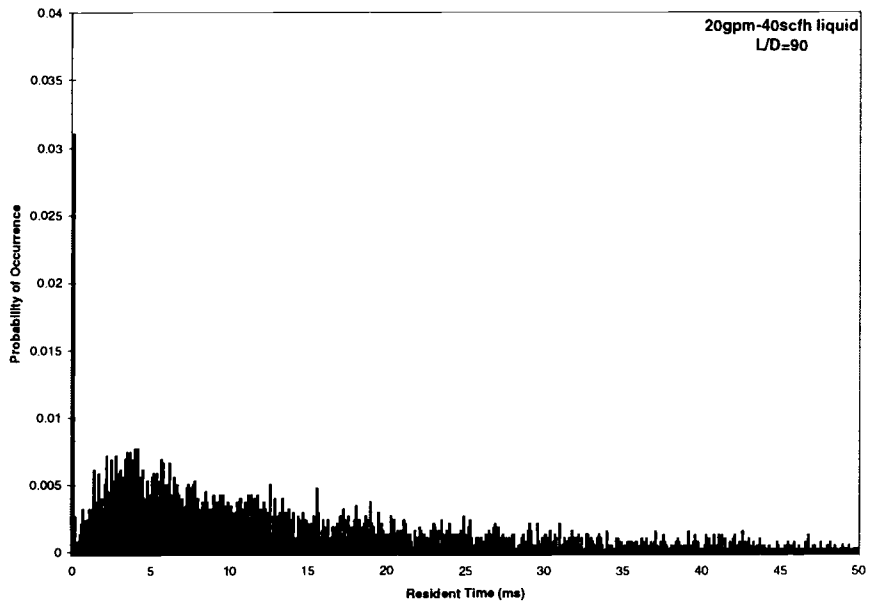


Figure 4.25: Resident liquid time distribution, $L/D=90$, 20 gpm, 40 scfh

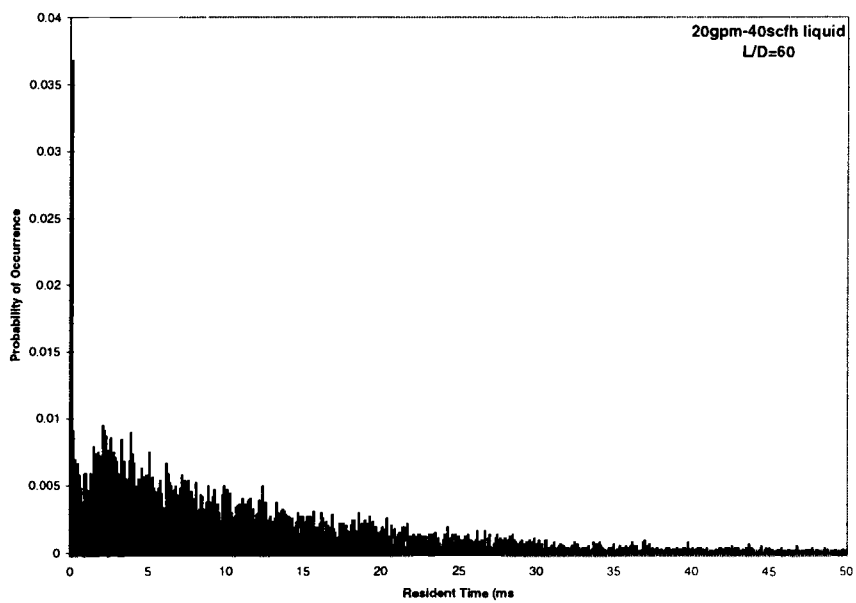


Figure 4.26: Resident liquid time distribution, $L/D=60$, 20 gpm, 40 scfh

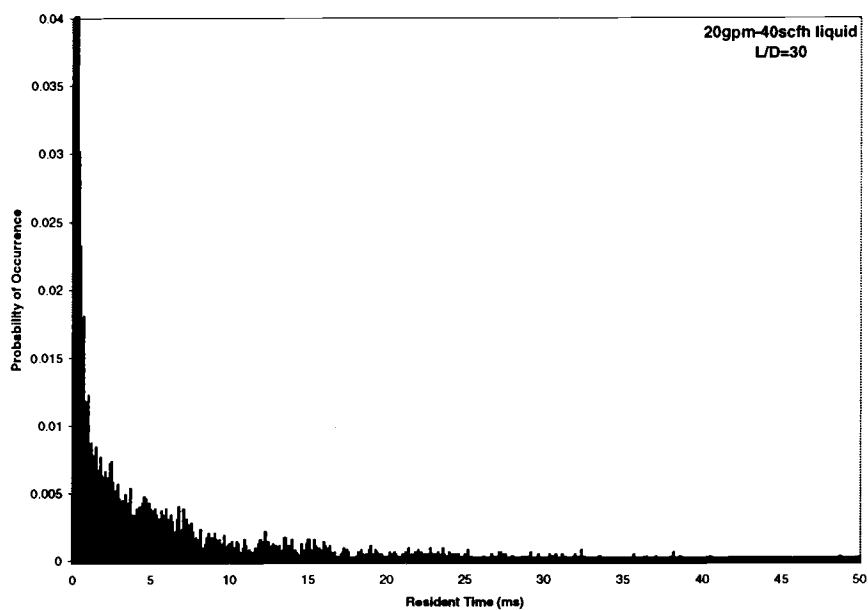


Figure 4.27: Resident liquid time distribution, $L/D=30$, 20 gpm, 40 scfh

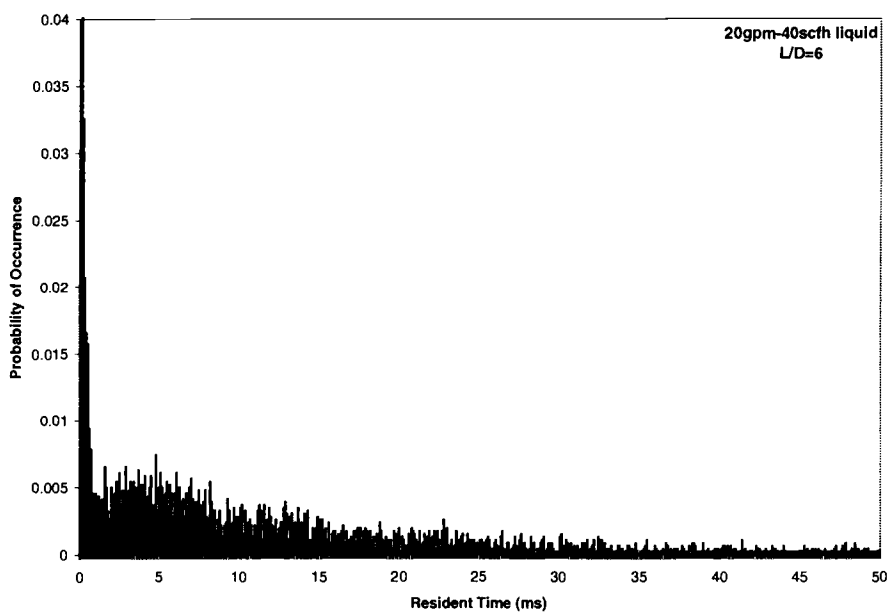


Figure 4.28: Resident liquid time distribution, $L/D=6$, 20 gpm, 40 scfh

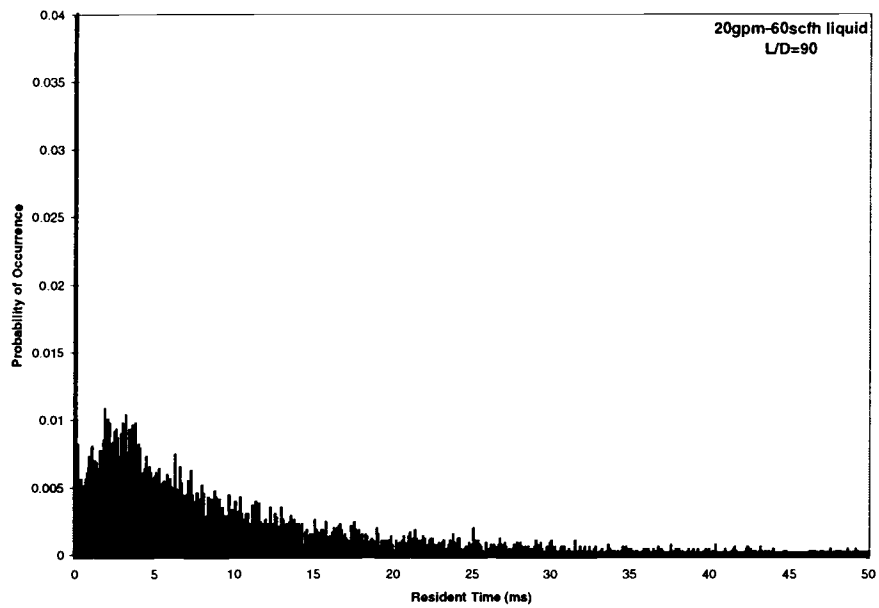


Figure 4.29: Resident liquid time distribution, $L/D=90$, 20 gpm, 60 scfh

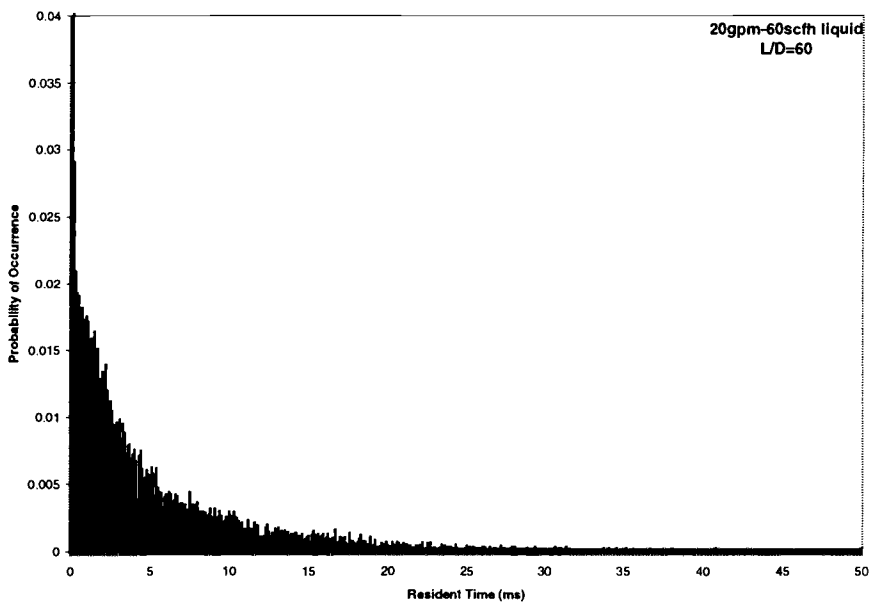


Figure 4.30: Resident liquid time distribution, $L/D=60$, 20 gpm, 60 scfh

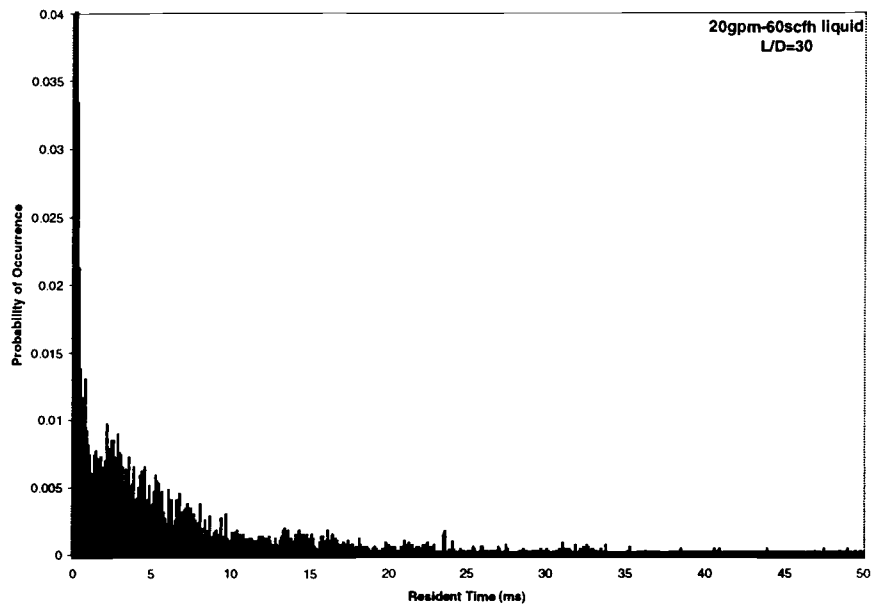


Figure 4.31: Resident liquid time distribution, $L/D=30$, 20 gpm, 60 scfh

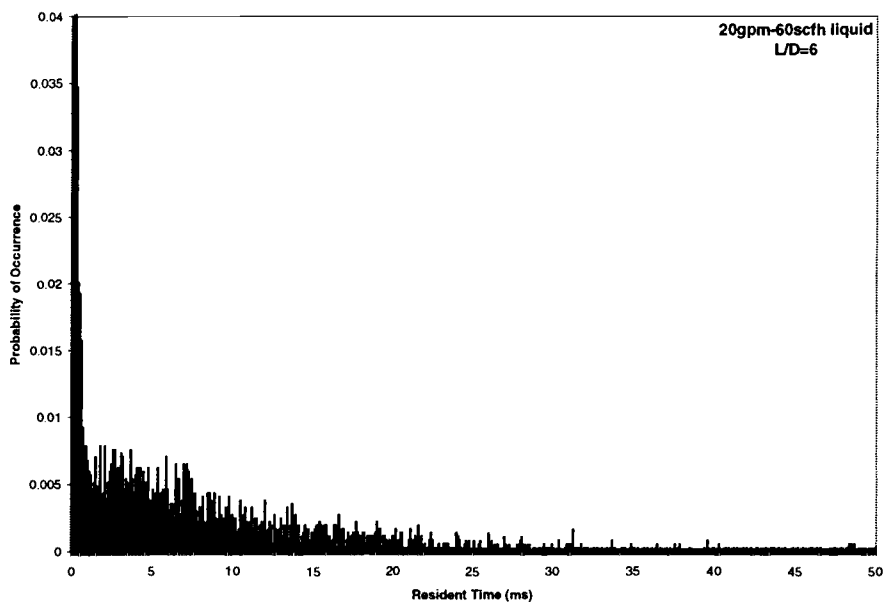


Figure 4.32: Resident liquid time distribution, $L/D=6$, 20 gpm, 60 scfh

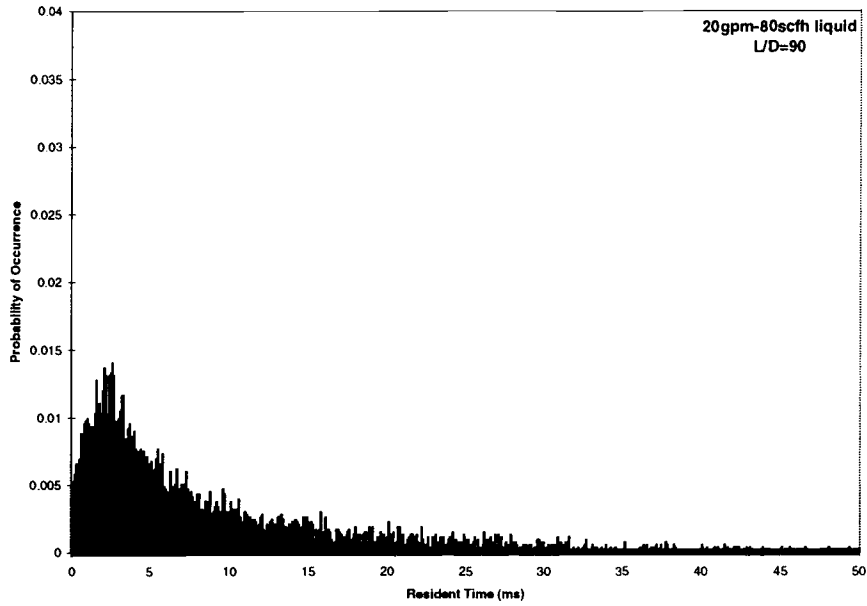


Figure 4.33: Resident liquid time distribution, $L/D=90$, 20 gpm, 80 scfh

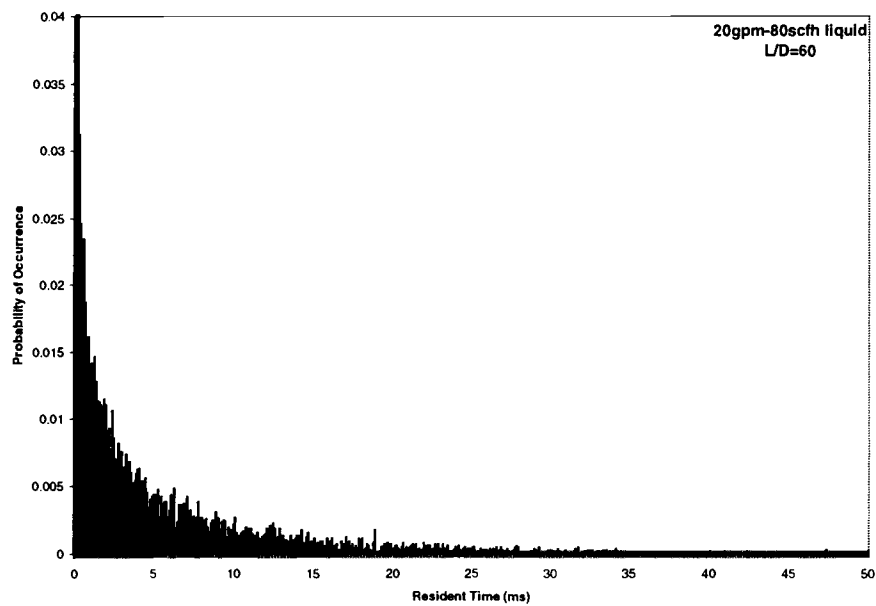


Figure 4.34: Resident liquid time distribution, $L/D=60$, 20 gpm, 80 scfh

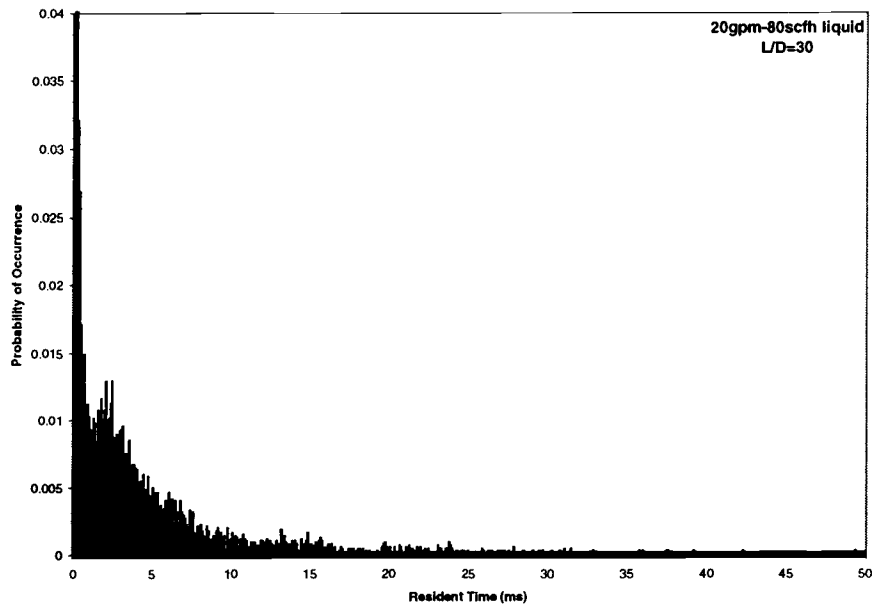


Figure 4.35: Resident liquid time distribution, $L/D=30$, 20 gpm, 80 scfh

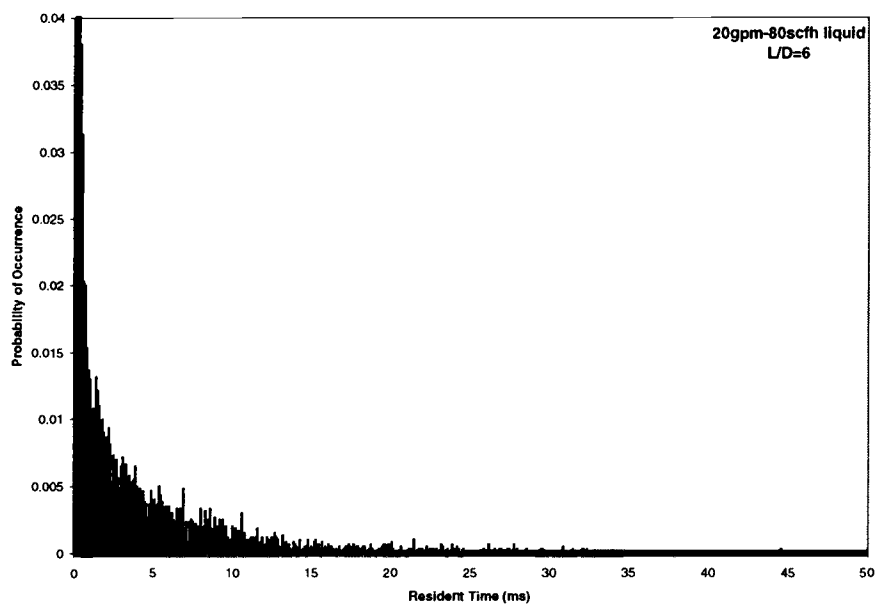


Figure 4.36: Resident liquid time distribution, $L/D=6$, 20 gpm, 80 scfh

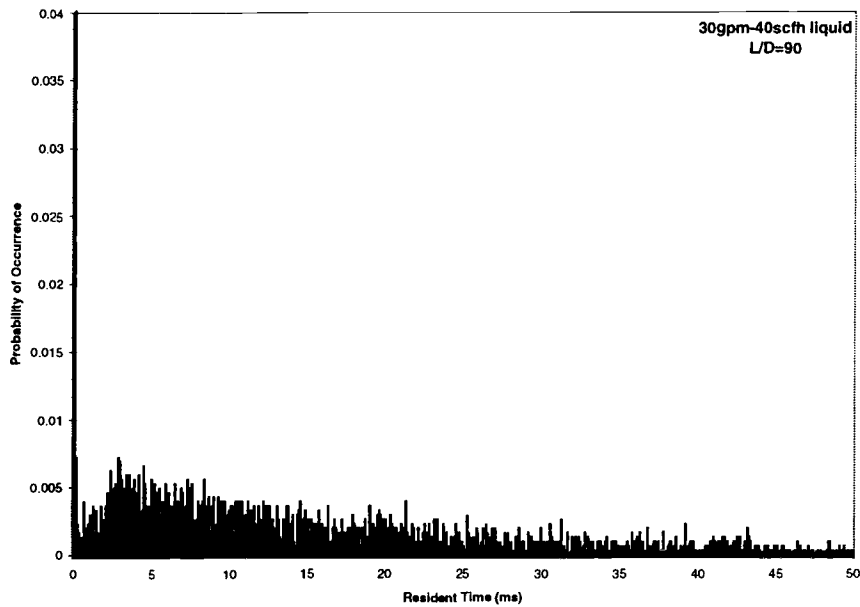


Figure 4.37: Resident liquid time distribution, L/D=90, 30 gpm, 40 scfh

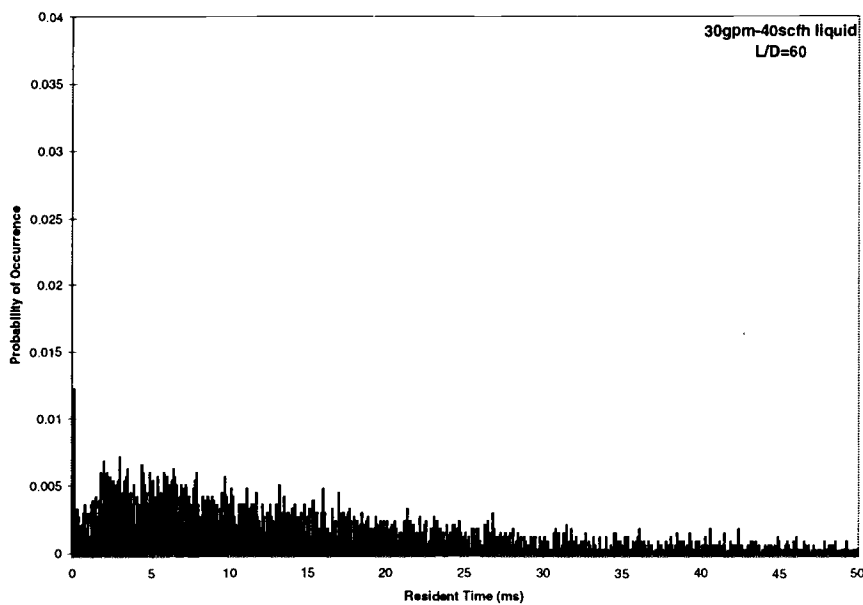


Figure 4.38: Resident liquid time distribution, L/D=60, 30 gpm, 40 scfh

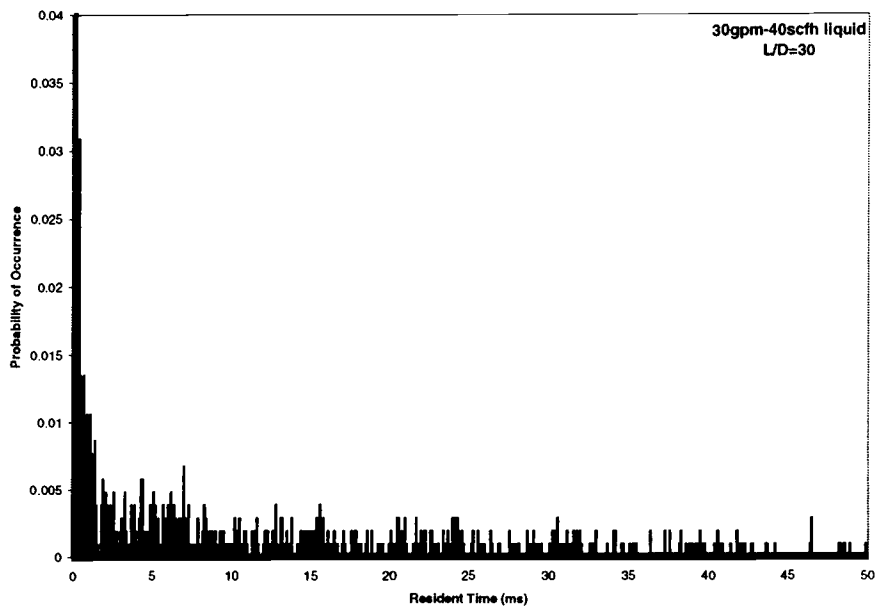


Figure 4.39: Resident liquid time distribution, L/D=30, 30 gpm, 40 scfh

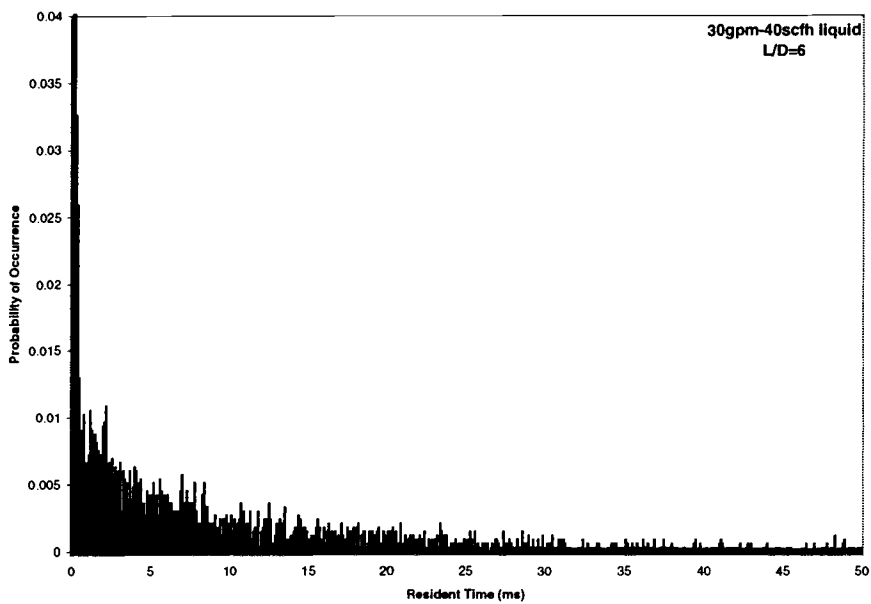


Figure 4.40: Resident liquid time distribution, L/D=6, 30 gpm, 40 scfh

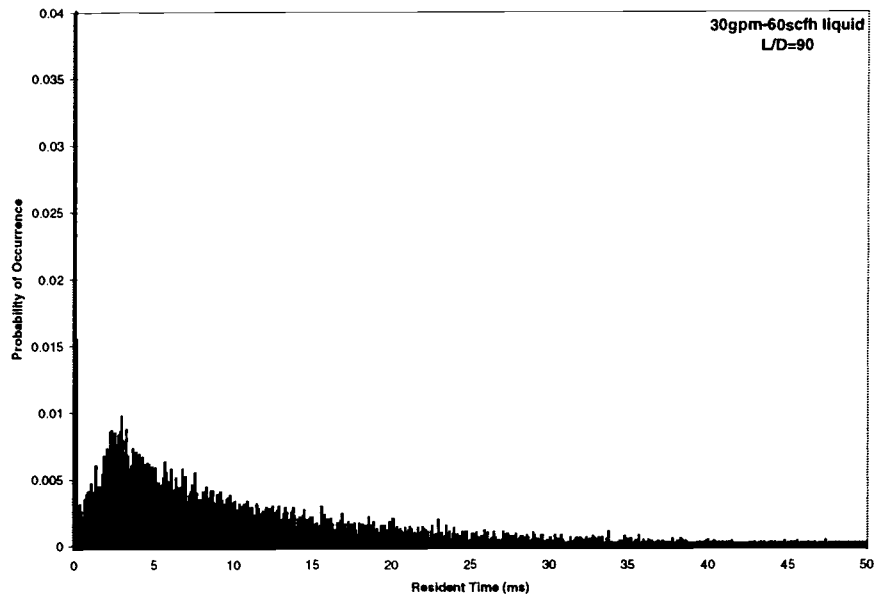


Figure 4.41: Resident liquid time distribution, $L/D=90$, 30 gpm, 60 scfh

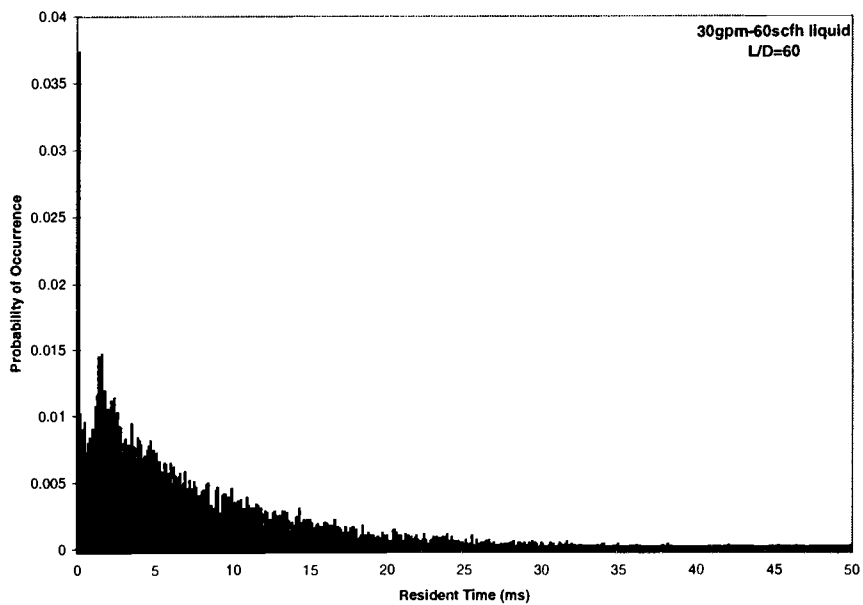


Figure 4.42: Resident liquid time distribution, $L/D=60$, 30 gpm, 60 scfh

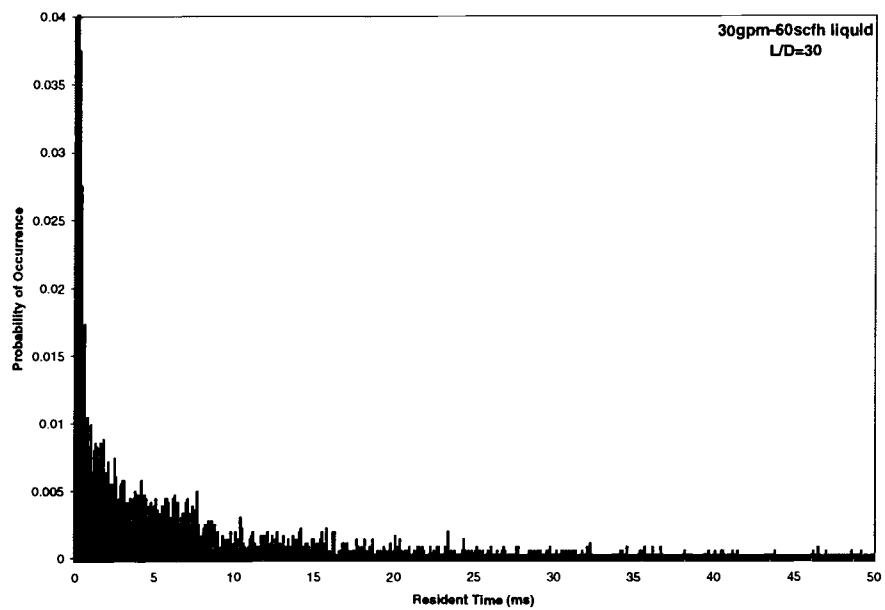


Figure 4.43: Resident liquid time distribution, $L/D=30$, 30 gpm, 60 scfh

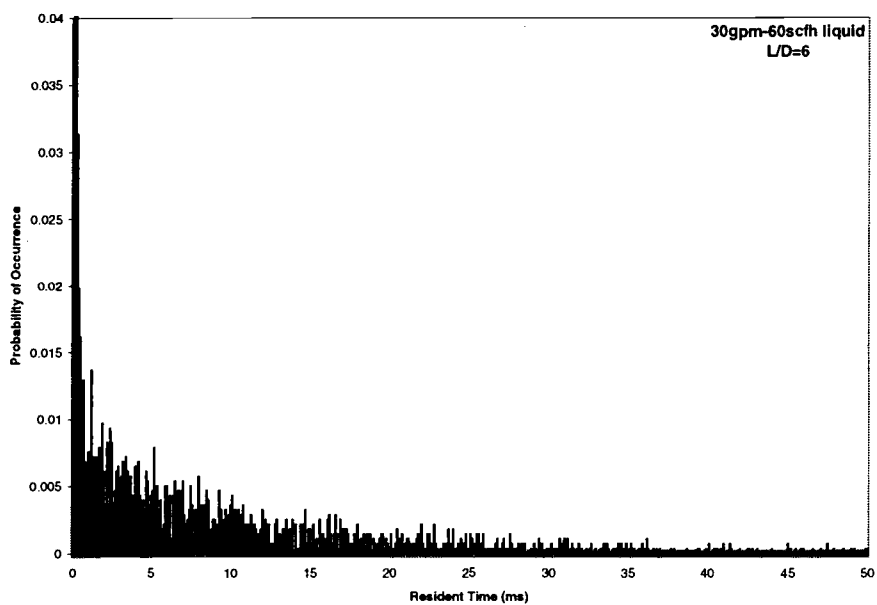


Figure 4.44: Resident liquid time distribution, $L/D=6$, 30 gpm, 60 scfh

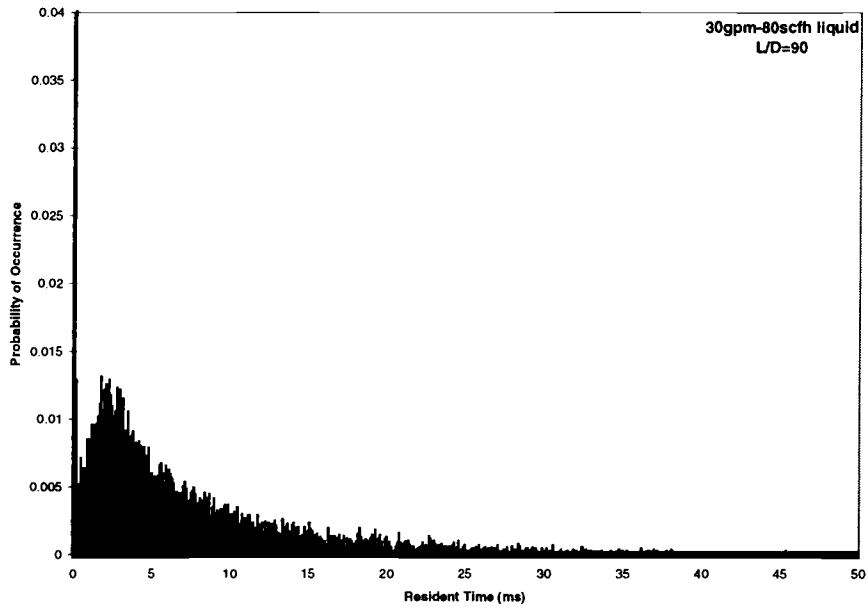


Figure 4.45: Resident liquid time distribution, L/D=90, 30 gpm, 80 scfh

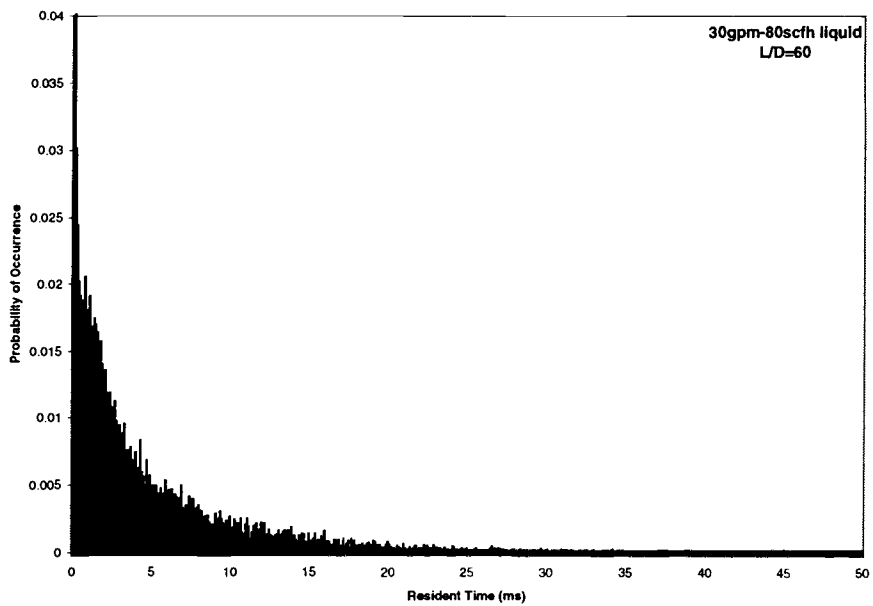


Figure 4.46: Resident liquid time distribution, L/D=60, 30 gpm, 80 scfh

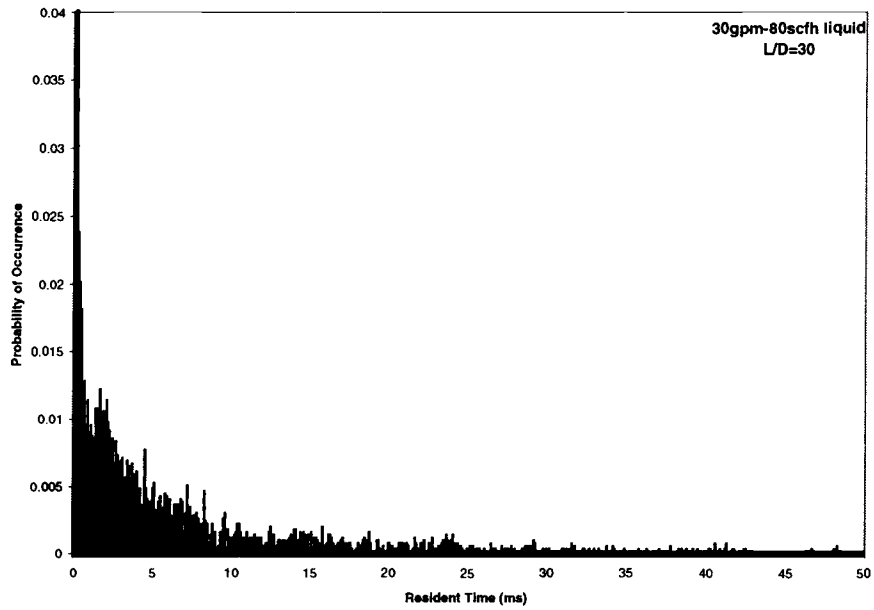


Figure 4.47: Resident liquid time distribution, $L/D=30$, 30 gpm, 80 scfh

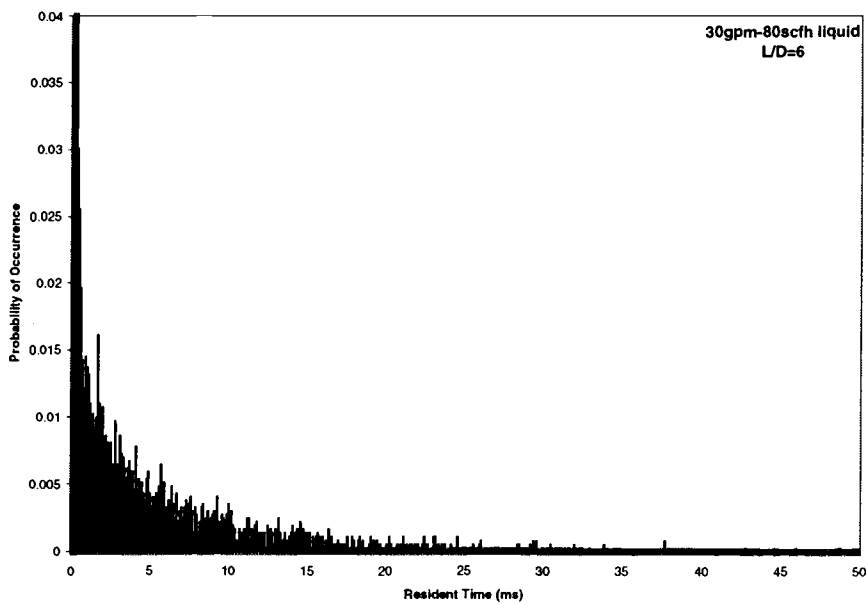


Figure 4.48: Resident liquid time distribution, $L/D=6$, 30 gpm, 80 scfh

4.3 VAPOR VELOCITY MEASUREMENT

The determination of vapor velocity is found by the difference in time between the rising signal edge from the first tip and the rising signal edge of the second probe tip. This would result in a good vertical velocity component if the bubbles did not have lateral motion. The lateral motion of the bubbles as well as the wide range of possible bubble sizes make it difficult in determining the proper spacing of the probe tips. If the probe tips are too far apart, most of the small bubbles, which contact the first probe tip, will miss the second probe tip. On the other hand, if the spacing between the probe tips is not wide enough, bubbles will contact both probe tips nearly simultaneously and produce erroneous values for velocity. It is usually determined that the ideal probe spacing is about 3 millimeters. Figures 4.49 through 4.54 show a proper velocity measurement from the probe at the axial position of $L/D=60$. Figure 4.55, however, shows an incorrect velocity measurement determined by the probe at the axial position of $L/D=6$. We know these values are incorrect because they do not physically make sense. It was later determined that the cause of this error was due to insufficient probe spacing and many of the incoming bubbles contacting both probe tips nearly simultaneously.

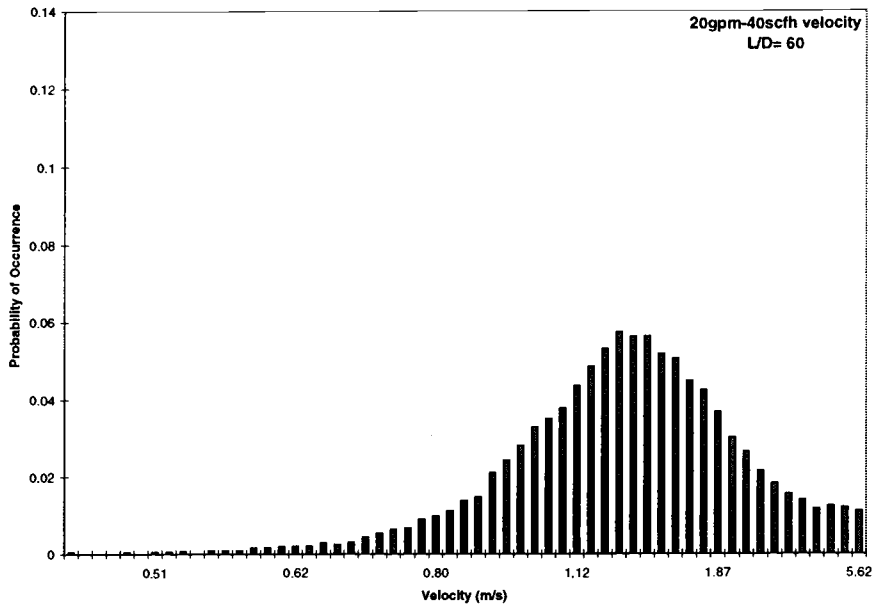


Figure 4.49: Velocity distribution, L/D=60, 20 gpm, 40 scfh

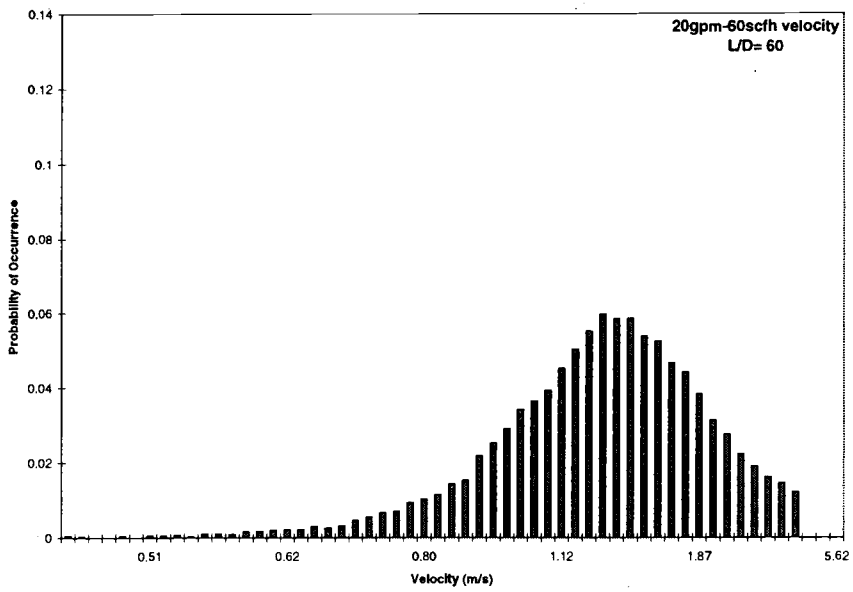


Figure 4.50: Velocity distribution, L/D=60, 20 gpm, 60 scfh

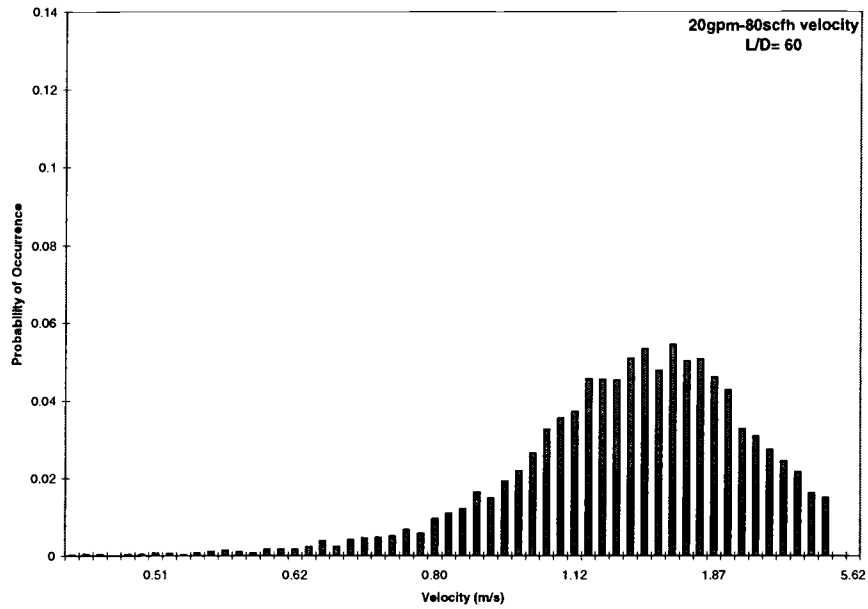


Figure 4.51: Velocity distribution, $L/D=60$, 20 gpm, 80 scfh

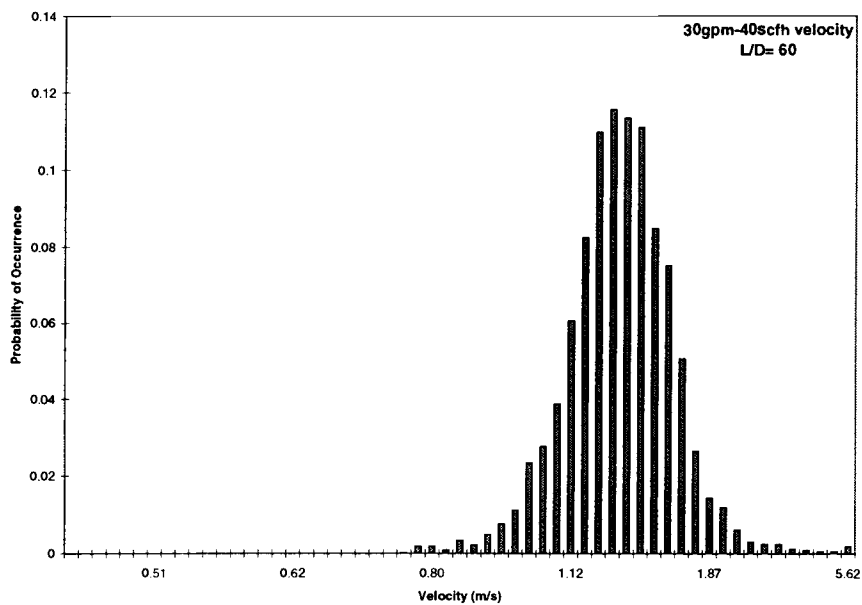


Figure 4.52: Velocity distribution, $L/D=60$, 30 gpm, 40 scfh

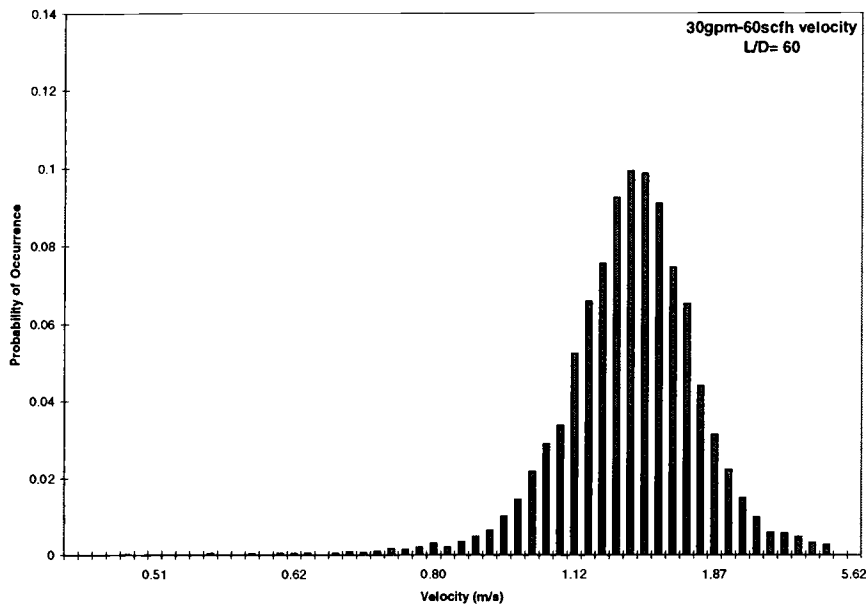


Figure 4.53: Velocity distribution, L/D=60, 30 gpm, 60 scfh

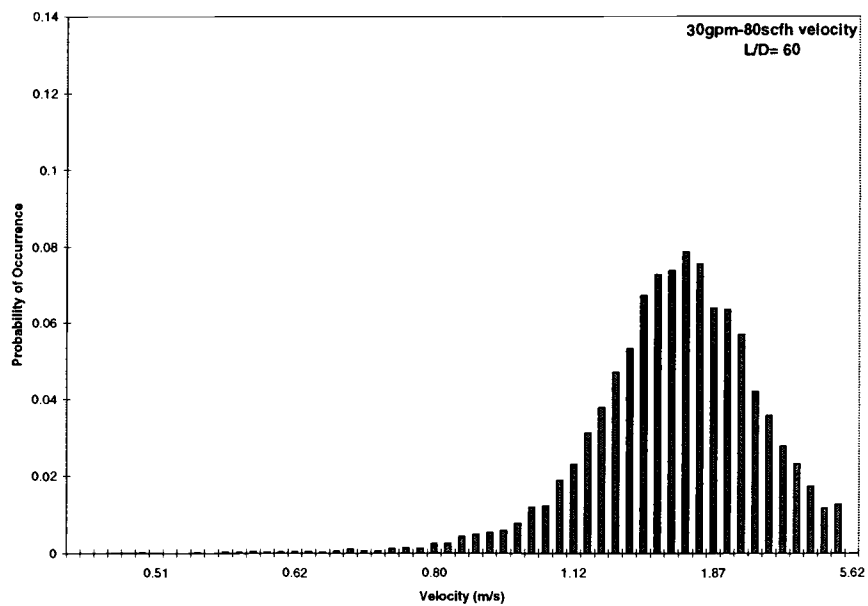


Figure 4.54: Velocity distribution, L/D=60, 30 gpm, 80 scfh

Table 4.7 shows a comparison between the average measured vapor velocity and correlations for bubble velocity. One will note the measured value for velocity is close, within one standard deviation, to the rise velocities predicted by correlations.

The terminal velocity correlation used are given is equations 4.7 - 4.9.

$$v_{\infty} = \left(\frac{8d(\rho_f - \rho_g)}{3\rho_f} \right)^{1/2} \quad \text{for } d < 5\text{mm} \quad (4.7)$$

$$v_{\infty} = 1.53 \left(\frac{\sigma g(\rho_f - \rho_g)}{\rho_f^2} \right)^{1/4} \quad \text{for } 5\text{mm} \leq d \leq 50.8\text{mm} \quad (4.8)$$

$$v_{\infty} = 0.35 \left(\frac{g(\rho_f - \rho_g)D}{\rho_f} \right)^{1/2} \quad \text{for } d > 50.8\text{mm} \quad (4.9)$$

where D is the tube diameter, σ is the fluid surface tension, and g is the acceleration due to gravity. The terminal velocity calculated by equations 4.7 – 4.9 are for single bubbles. In a real system, the bubble terminal velocity is influenced by surrounding bubbles giving a rise velocity that is less than the values calculated in equations 4.7 – 4.9. The terminal velocity is altered in the following way in the presence of other bubbles.

$$v_{ij} = v_{\infty} (1 - \langle \alpha \rangle)^n \quad (4.10)$$

where n is equal to; 3 for equation 4.7, 1.5 for equation 4.8, and 0 for equation 4.9. The bubble drift velocity is then added to the liquid velocity to obtain the total bubble velocity.

Any differences between the measured and correlated velocities could be attributed to the fact that the measured velocity is influenced by how well one can measure the distance between the probe tips. Another possibility is that lateral motion of the bubbles causes some of the bubbles to contact both probes nearly simultaneously. This could skew the velocity data to higher values. However, in this case, these factors only have a secondary effect on the velocity measurements. The reason this can be said is the spacing between the probe tips is measured very accurately as well as the fact that bubbles with velocities that are unphysical are eliminated during this calculation.

Table 4.7: Velocity Results for L/D=60 Location

	$\frac{j_f}{(1-\alpha)}$ (m/s)	v_f (m/s)	v_b (m/s)	Measured Average Velocity (m/s)	Standard Deviation Velocity (m/s)
TC-1	1.18	0.15	1.33	1.34	0.23
TC-2	0.87	0.14	1.01	1.15	0.28
TC-3	1.30	0.14	1.44	1.41	0.27
TC-4	1.00	0.15	1.15	1.31	0.35
TC-5	1.42	0.15	1.57	1.52	0.31
TC-6	1.11	0.16	1.27	1.33	0.37

Figure 4.55 shows an incorrect velocity distribution measurement by the probe at L/D=6. As mentioned earlier, it was found that the spacing of this probe was insufficient and several bubbles hit both of the sensors at nearly the same time. One can easily discern the bubbles that contact both tips at nearly the same time since the associated bubble velocity will be unphysical. The large gaps between bins which contain data is due to the fact that the velocity may only take on discrete values since the value for velocity is based on the number of scans between the signal being detected on the first and the rear sensor. This means that if only a few

scans occur between the two rising signal edges from the probe, the velocity will change sensitively for a small change in the number of scans used to determine velocity.

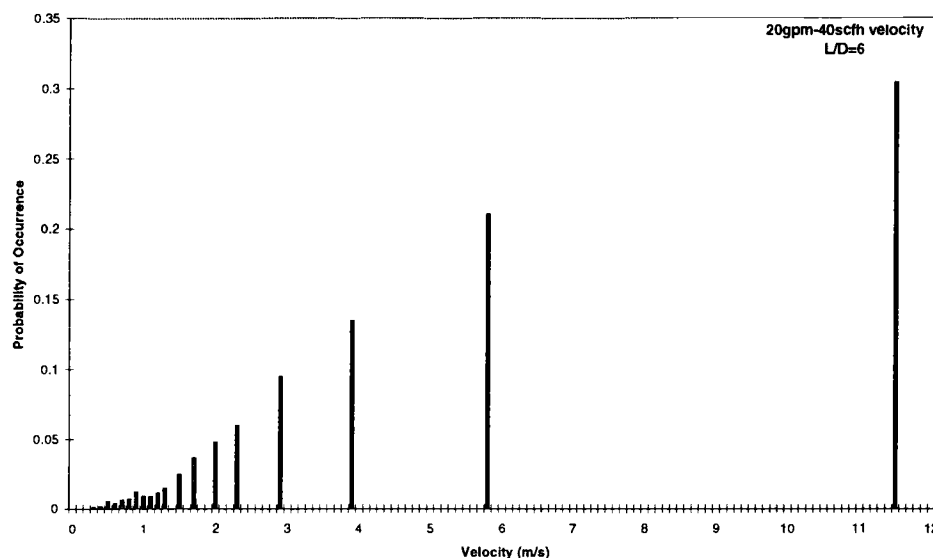


Figure 4.55: Improper velocity measurement at $L/D=6$

4.4 TWO-GROUP VOID FRACTION

To validate the two-group interfacial area transport equation, it is important to measure the transfer of interfacial area between the two groups. In this research, however, only the study on the transfer of void fraction contribution to each group was analyzed because the interfacial area is difficult to measure directly with a double sensor probe, especially the cap/slug bubble group since this group does not meet the spherical shape assumption. Figure 4.56 displays the resident vapor time for each of the two bubble groups. The two scales on Figure 4.56 are different because there are many more small bubbles than the larger cap/slug bubbles

present. If two different scales were not used for plotting purposes, one would be able to clearly see only one of the two groups. One can clearly see from the figure, that there exist two distinct distributions in the case of slug flow. It is also interesting to note that the shape of the two distributions is completely different. On one hand, the spherical/distorted bubble group tends to take on a lognormal or gamma distribution for resident vapor time as well as for bubble size. On the other hand, the cap/slug bubble group takes on a normal distribution for resident vapor time as well as for bubble sizes.

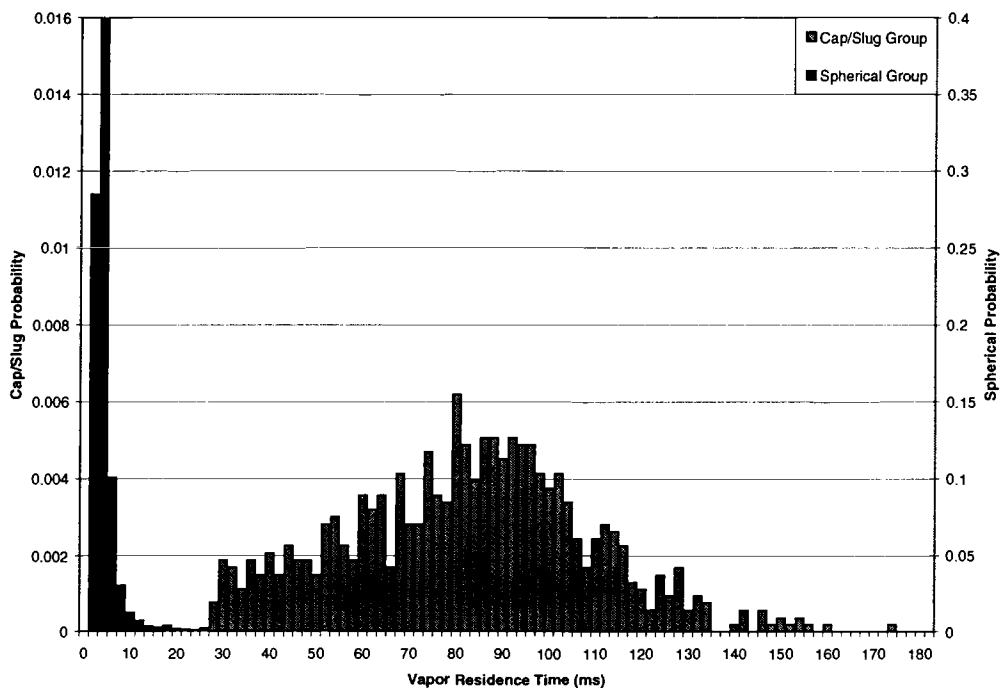


Figure 4.56: Two-group vapor time distribution for $L/D=90$, 20gpm, 80scfh

Tables 4.8 – 4.11 show the void fraction broken up into two groups for each test that was performed. This set of tables indicates how the void fraction is distributed

between the spherical/distorted bubble group and the cap/slug bubble group as a function of flow rates and axial position. One can clearly see from Tables 4.10 and 4.11 that, since there is no void fraction contribution from group 2 bubbles, the flow stays within the bubbly flow regime throughout all of the performed tests. One can note from the data in Tables 4.8 and 4.9, how the flow rates affect the relative weights of the group 1 and group 2 void fraction contributions. This set of tables is useful to gain a better understanding of how the net change in the transfer of vapor volume across the two groups of bubbles occurs.

Table 4.8: Two group void fraction table $L/D=90$

	Group 1 Void Fraction	Group 2 Void Fraction	Total Void Fraction
TC-1	0.089	0	0.089
TC-2	0.132	0.023	0.155
TC-3	0.173	0.002	0.175
TC-4	0.169	0.165	0.333
TC-5	0.184	0.152	0.336
TC-6	0.068	0.316	0.384

Table 4.9: Two group void fraction table $L/D=60$

	Group 1 Void Fraction	Group 2 Void Fraction	Total Void Fraction
TC-1	0.085	0	0.085
TC-2	0.180	~ 0	0.180
TC-3	0.195	~ 0	0.195
TC-4	0.309	0.071	0.380
TC-5	0.242	0.111	0.353
TC-6	0.141	0.291	0.432

Table 4.10: Two group void fraction table $L/D=30$

	Group 1 Void Fraction	Group 2 Void Fraction	Total Void Fraction
TC-1	0.015	0	0.015
TC-2	0.112	0	0.112
TC-3	0.053	0	0.053
TC-4	0.086	0	0.086
TC-5	0.056	0	0.056
TC-6	0.118	~ 0	0.118

Table 4.11: Two group void fraction table $L/D=6$

	Group 1 Void Fraction	Group 2 Void Fraction	Total Void Fraction
TC-1	0.051	0	0.051
TC-2	0.056	0	0.056
TC-3	0.047	0	0.047
TC-4	0.080	0	0.080
TC-5	0.092	~ 0	0.092
TC-6	0.191	~ 0	0.191

Figures 4.57 - 4.59 represent the data from tables 4.8 through 4.11 in a graphical form. These figures indicate clear trends in the overall void fraction as well as the void fraction contribution from the cap/slug bubble group as well as the spherical/distorted bubble group. As one can note from Figure 4.59 and Figure 4.60, the flow at $L/D=6$ and $L/D=30$ stays within the bubbly flow regime for all test cases that were performed. One may also note that when slug flow occurs, the overall void fraction is dominated by the group two void fraction contribution.

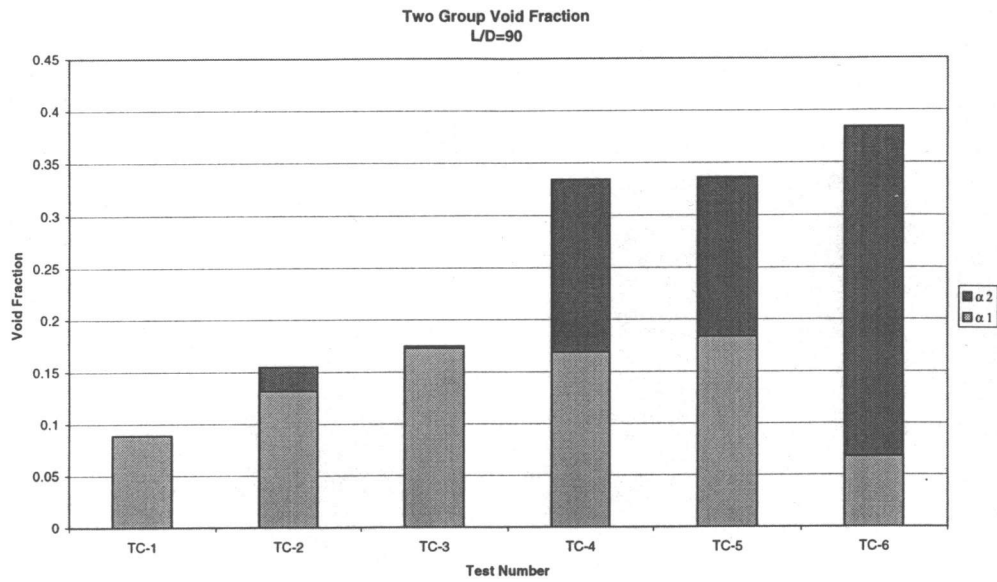


Figure 4.57: Two-group void fraction, $L/D=90$

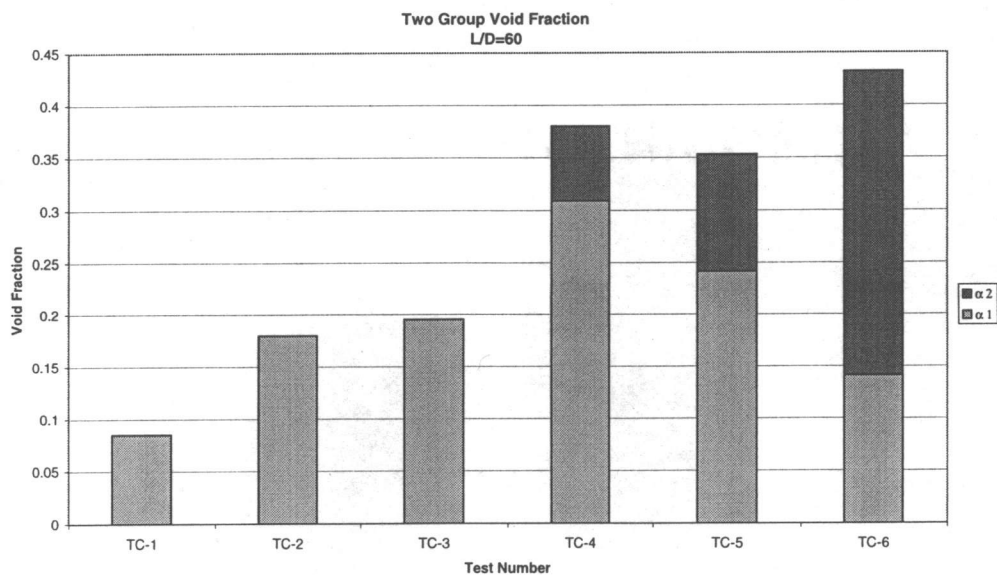


Figure 4.58: Two-group void fraction, $L/D=60$

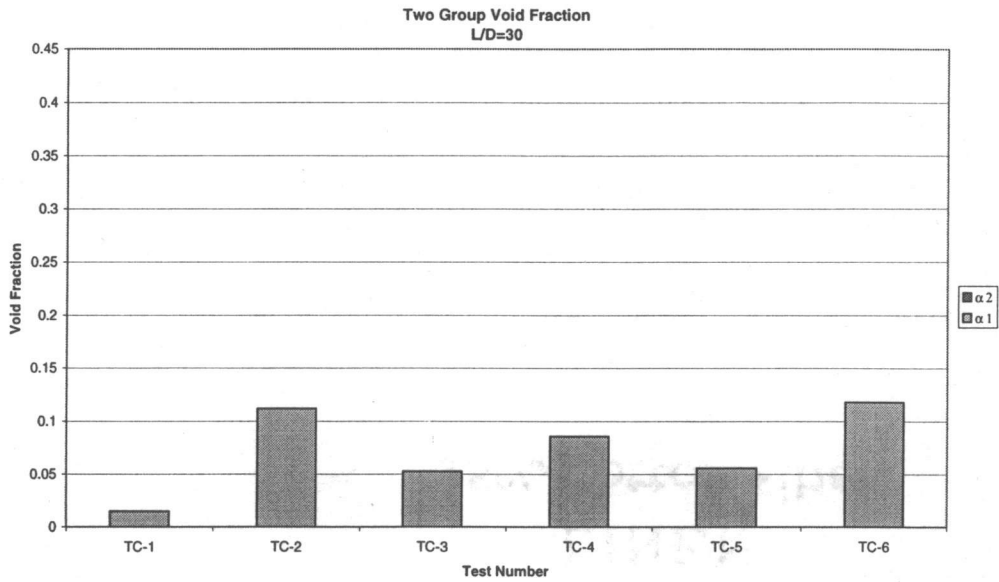


Figure 4.59: Two-group void fraction, L/D=30

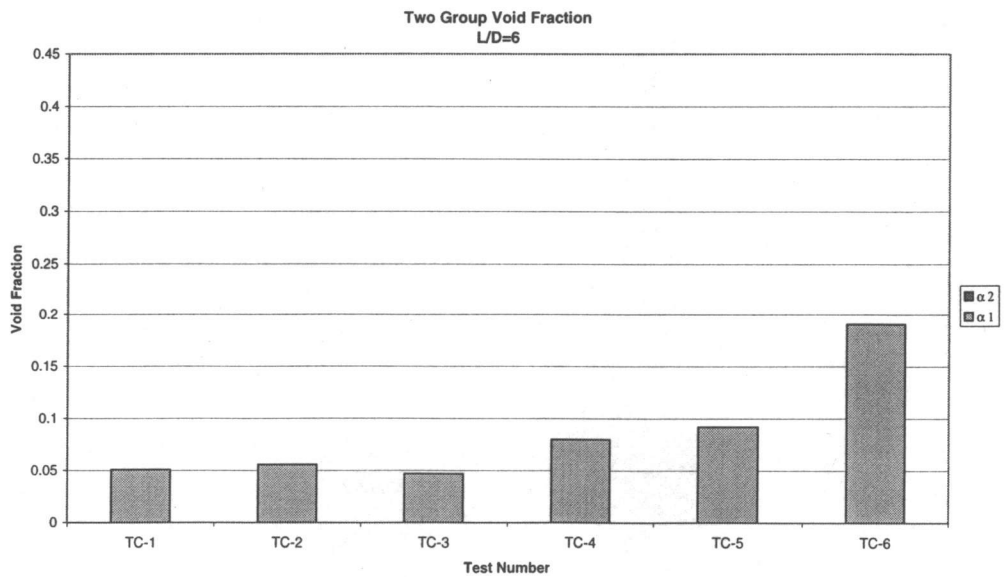


Figure 4.60: Two-group void fraction, L/D=6

5. CONCLUSIONS AND PLANS FOR FUTURE WORK

As part of this thesis, a two-phase vertical loop was designed and constructed. As part of the data acquisition and instrumentation, a program written with LabVIEW was created in order to acquire the data in the required manner. A C++ program was also developed as part of the post-processing portion of the data acquisition. Four double sensor impedance probes were constructed along with custom designed instrumentation mounts that allow the probes to be placed in several locations. As part of the instrumentation, an alternating current based circuit was developed for use in signal processing for each impedance probe that was constructed.

Collection of data within a test series was accomplished along with the required post processing and analysis required for properly interpreting the data. It was found that the acquired data followed the intuitively expected trend. From this data, one can distinguish where slug flow occurs as well as the transition from bubbly flow to slug flow based, not only changes in the void fraction, but also in dramatic changes in the standard deviation and mean bubble size. Some interesting information on the behavior of the liquid residence time was also found.

The main findings of this research are:

- Mean resident vapor time increases with increasing gas flow
- Mean resident liquid time increases with increasing liquid flow
- Slug flow is comprised of two distinct distributions
- One may use two void fraction groups to determine flow regime
- Measured centerline bubble velocity is higher than the average value
- Spherical bubble distribution takes on a gamma or lognormal distribution for vapor residence time
- Cap/slug bubbles take on a normal distribution for vapor residence time
- The velocity distribution tends to be Gaussian

- The resident vapor time becomes less peaked and shifted toward higher values as a function of axial position

As part of future work, additional tests will be run and compared. The double sensor probes will be replaced with miniaturized four-sensor probes in order to accurately measure local interfacial area concentration. The four-sensor probes will be traversed across the pipe to allow for mapping of the two-phase flow parameters along both the axial and radial directions. A theoretical analysis will also be performed to determine a relationship to predict how the standard deviation and the mean bubble size change for different flow rates and for different axial locations. After the initial set of theoretical work is completed, the next stage would be to theoretically determine how flow develops from a single distribution of small bubbles to two separate distributions in the case of slug flow.

BIBLIOGRAPHY

1. Chen, Y., Fan, L., "Drift Flux in Gas-Liquid-Solid Fluidized Systems from the Dynamics of Bed Collapse", *Chemical Engineering Science*, Vol. 45, pp. 935-945, 1990
2. Costigan, G., Whalley, P.B., "Slug Flow Regime Identification from Dynamic Void Fraction Measurements in Vertical Air-Water Flows", *Int. J. Multiphase Flow*, Vol. 23, No. 2, pp. 263-282, 1997
3. Franca, F., Lahey, R.T. Jr., "The Use of Drift-Flux Techniques for the Analysis of Horizontal Two-Phase Flows", *Int. J. Multiphase Flow*, Vol. 18, No. 6, pp. 787-801, 1992
4. Hibiki, T., Hogsett, S., Ishii, M., "Local Measurement of Interfacial Area, Interfacial Velocity, and Liquid Turbulence in Two-Phase Flow", *Nuclear Engineering and Design*, Vol. 184, pp. 287-304, 1998
5. Hibiki, T., Ishii, M., "Experimental Study on Interfacial Area Transport in Bubbly Two-Phase Flows", *Int. J. Heat Mass Transfer*, Vol. 42, pp. 3019-3035, 1999
6. Hibiki, T., Ishii, M., "Two-Group Interfacial Area Transport Equations at Bubbly-to-Slug Flow Transition", *Nuclear Engineering and Design*, Vol. 202, pp. 39-76, 2000
7. Hibiki, T., Ishii, M., Zheng, X., "Axial Interfacial Area Transport of Vertical Bubbly Flows", *Int. J. Heat Mass Transfer*, Vol. 44, pp. 1896-1888, 2001
8. Hibiki, T., Takamasa, T., Ishii, M., "Interfacial Area Transport of Bubbly Flow in a Small Diameter Pipe", *Journal of Nuclear Science and Technology*, Vol. 38, No. 8, pp. 614-620, 2001
9. Hogsett, S., Ishii, M., "Local Two-Phase Flow Measurements Using Sensor Techniques", *Nuclear Engineering and Design*, Vol. 175, pp. 15-24, 1997
10. Jepson, W.P., Taylor, R.E., "Slug Flow and its Transitions in Large-Diameter Horizontal Pipes", *Int. J. Multiphase Flow*, Vol. 19, No. 3, pp. 411-420, 1993
11. Kaminaga, F., "Assessment of Void Fraction Correlations for Vertical Two-Phase Flow in Small Diameter Tube at Low Liquid Velocity", *Journal of Nuclear Science and Technology*, Vol. 29, pp. 695-698, July 1992

12. Kataoka, I., Ishii, M., "Drift Flux Model for Large Diameter Pipe and New Correlation for Pool Void Fraction", *Int. J. Heat Mass Transfer*, Vol. 30, pp. 1927-1939, 1987
13. Kataoka, Y., Suzuki, H., Murase, M., "Drift-Flux Parameters for Upward Gas Flow in Stagnant Liquid", *Journal of Nuclear Science and Technology*, Vol. 24, pp. 580-586, July 1987
14. Kim, S., Fu, X.Y., Wang X., Ishii, M., "Study on Interfacial Structures in Slug Flows Using a Miniaturized Four-Sensor Conductivity Probe", *Nuclear Engineering and Design*, Vol. 204, pp. 45-55, 2001
15. Kocamustafaogullari, G., Huang, W.D., "Internal Structure and Interfacial Velocity Development for Bubbly Two-Phase Flow", *Nuclear Engineering and Design*, Vol. 151, pp. 79-101, 1994
16. Kocamustafaogullari, G., Huang, W.D., Razi, J., "Measurement and Modeling of Average Void Fraction, Bubble Size and Interfacial Area", *Nuclear Engineering and Design*, Vol. 148, pp. 437-453, 1994
17. Lafi, A.Y. and Reyes, J.N. Jr., "Phenomenological Models for Fluid Particles Coalescence and Breakage", Technical Report, OSU-NE-9120, Department of Nuclear Engineering, Oregon State University, Corvallis, Oregon, 1991.
18. Leung, W.H., Revankar, S.T., Ishii, Y., Ishii, M., "Axial Development of Interfacial Area and Void Concentration Profiles Measured by Double-Sensor Probe Method", *Int. J. Heat Mass Transfer*, Vol. 38, pp. 445-453, 1995
19. Morel, C., Goreaud, N., Delhaye, J.M., "The Local Volumetric Interfacial Area Transport Equation: Derivation and Physical Significance", *Int. J. Multiphase Flow*, Vol. 25, pp. 1099-1128, 1999
20. Morriss, S.L., Hill, A.D., "Ultrasonic Imaging and Velocimetry in Two-Phase Pipe Flow", *Journal of Energy Resources Technology*, Transactions of the ASME, Vol. 115, No. 2, pp. 108-116, Jun, 1993
21. Mudde, R.F., Bakker, R.A., van den Akker, H.E.A., "Noise Analysis of Transmitted Light Beams for Determining Bubble Velocity and Gas Holdup in a Bubble Column", *Chemical Engineering Science*, Vol. 47, pp. 3631-3638, 1992
22. Nydal, O.J., Pintus, S., Andreussi, P., "Statistical Characterization of Slug Flow in Horizontal Pipes", *Int. J. Multiphase Flow*, Vol. 18, No. 3, pp. 439-453, 1992

23. Pinto, A.M.F.R., Campos, J.B.L.M., "Coalescence of Two Gas Slugs Rising in a Vertical Column of Liquid", *Chemical Engineering Science*, Vol. 51, No. 1, pp. 45-54, 1996
24. Revankar, S.T., Ishii, M., "Local Interfacial Area Measurement in Bubbly Flow", *Int. J. Heat Mass Transfer*, Vol. 35, pp. 913-925, 1992
25. Revankar, S.T., Ishii, M., "Theory and Measurement of Local Area Using a Four Sensor Probe in Two-Phase Flow", *Int. J. Heat Mass Transfer*, Vol. 36, pp. 2997-3007, 1993
26. Reinecke, N., Petritsch, G., Boddem, M., Mewes, D., "Tomographic Imaging of the Phase Distribution in Two-Phase Slug Flow", *Int. J. Multiphase Flow*, Vol. 24, No. 4, pp. 617-634, 1998
27. Reyes, J.N. Jr., Lafi, A.Y., Saloner, D., "The Use of MRI to Quantify Multi-Phase Flow Patterns and Transitions: an Application to Horizontal Slug Flow", *Nuclear Engineering and Design*, Vol. 184, pp. 213-228, 1998
28. Rinne, A., Loth, R., "Development of Local Two-Phase Flow Parameters for Vertical Bubbly Flow in a Pipe with Sudden Expansion", *Experimental Thermal and Fluid Science*, Vol. 13, pp.152-166, 1996
29. Sena Esteves, M.T., Guedes De Carvalho, J.R.F., "Liquid-Side Mass Transfer Coefficient for Gas Slugs Rising in Liquids", *Chemical Engineering Science*, Vol. 48, No. 20, pp. 3497-3506, 1993
30. Taitel, Y., Barnea, D., "Effect of Gas Compressibility on a Slug Tracking Model", *Chemical Engineering Science*, Vol. 53, No. 11, pp. 2089-2097, 1998
31. Tudose, E.T., Kawaji, M., "Experimental Investigation of Taylor Bubble Acceleration Mechanism in Slug Flow", *Chemical Engineering Science*, Vol. 54, pp. 5761-5775, 1999
32. van Hout, R., Shemer, L., Barnea, D., "Spatial Distribution of Void Fraction within a Liquid Slug and Some Other Related Parameters", *Int. J. Multiphase Flow*, Vol. 18, No. 6, pp. 831-845, 1992
33. Wilmarth, T., Ishii, M., "Interfacial Area Concentration and Void Fraction of Two-Phase Flow in Narrow Rectangular Vertical Channels", *Transactions of the ASME*, Vol. 119, pp. 916-922, December 1997

34. Wu, Q., Ishii, M., "Sensitivity Study on Double-Sensor Conductivity Probe for the Measurement of Interfacial Area Concentration in Bubbly Flow", *Int. J. Multiphase Flow*, Vol. 25, pp.153-173, 1999
35. Wu, Q., Kim, S., Ishii, M., Beus, S.G., "One-Group Interfacial Area Transport in Vertical Bubbly Flow", *Int. J. Heat Mass Transfer*, Vol. 41, pp.1103-1112, 1998
36. Zuber, N., Findley, J.A., "Average Volumetric Concentration in Two-Phase Flow Systems", *J. Heat Transfer*, pp. 453-468, Nov., 1965

APPENDIX

C++ DATA PROCESSING PROGRAM

```
#include <fstream.h>
#include <iostream.h>
#include <stdio.h>
#include <stdlib.h>
#include <string.h>

void main()
{
    ifstream fs_in;
    ofstream fs1_Liquid, fs1_Bubble;
    char str1[40]= "_all_results.txt";
    char str2[40]= "_valid_bubble.txt";
    char infile[80];
    char outfile1[80];
    char outfile2[80];
    char string[80];

    char directory[]= "//Bernoulli/Student/Kent Abel/";

    cout << "Enter input file name: ";
    cin >> string;

    strcpy(infile, directory);
    strcat (infile, string,80);

    fs_in.open(infile);
    cout << infile << endl;

    strcpy(outfile1, directory);
    strcat(outfile1, string, 80);

    strcpy(outfile2, directory);
    strcat(outfile2, string, 80);

    strcat (outfile1, str1,80);
    strcat (outfile2, str2,80);

    fs1_Liquid.open(outfile1);
    fs1_Bubble.open(outfile2);

    fs1_Liquid << "Bubble Length" << "\t" << "Liquid Length" << endl;
    fs1_Bubble << "Bubble Length" << "\t" <<"Liquid Length"<< "\t"<<
    "Velocity Length" << endl;

    bool pre_ch1=false, pre_ch2=false;
    bool ch1,ch2;
    int bubbleSize=0;
    int liquidSize=0;
```

```

        int Leading1=0,Leading2=0;

while(!fs_in.eof())
    {
        double a, b;
        fs_in>> a >> b;
        ch1=a>4; ch2=b>4;
        if (pre_ch1==false && ch1==true)    // leading edge of
ch1
            {
                Leading1=liquidSize;
                pre_ch1=true;
            }
            if (ch1==true)
            {
                bubbleSize++;
                if (pre_ch2==false && ch2==true)    // leading edge of
ch2
                    {
                        Leading2=Leading1+bubbleSize-1;
                        pre_ch2=true;
                    }
            }
            else
            {
                liquidSize++;
            }
        if (pre_ch1==true && ch1==false) // falling edge of ch1
            {
                if (liquidSize!=0)
                {
                    fs1_Liquid << bubbleSize <<"\t" << liquidSize <<endl;
// output of all bubble and
liquid
                }
                if (Leading1<Leading2) // valid bubble
                {
                    fs1_Bubble<< bubbleSize<< "\t" << liquidSize << "\t"<<
(Leading2-Leading1) <<endl; // output of valid bubble
                }
                pre_ch1=false;
                pre_ch2=false;
                bubbleSize=0;
                liquidSize=0;
                Leading1=0;
                Leading2=0;
            }
    }
    fs_in.close();
    fs1_Liquid.close();
    fs1_Bubble.close();
}

```